



Title	NEW ASPECT OF MAGNETIC PHASE TRANSITIONS IN LOCALIZED SPIN SYSTEMS UNDER HIGH MAGNETIC FIELD
Author(s)	Sakakibara, Toshiro
Citation	大阪大学, 1983, 博士論文
Version Type	VoR
URL	https://hdl.handle.net/11094/24345
rights	
Note	

The University of Osaka Institutional Knowledge Archive : OUKA

<https://ir.library.osaka-u.ac.jp/>

The University of Osaka

NEW ASPECT OF MAGNETIC PHASE TRANSITIONS
IN LOCALIZED SPIN SYSTEMS
UNDER HIGH MAGNETIC FIELD

by

Toshiro SAKAKIBARA

DISSERTATION IN PHYSICS

THE OSAKA UNIVERSITY
GRADUATE SCHOOL OF SCIENCE
TOYONAKA, OSAKA
March, 1983

CONTENTS

PART I. EXPERIMENTAL TECHNIQUES ON PRECISE MAGNETIZATION,	
MAGNETORESISTANCE MEASUREMENTS AND TEMPERATURE	
CONTROL UNDER PULSED HIGH MAGNETIC FIELD	
ABSTRACT	1
§1. INTRODUCTION	2
§2. MAGNETIZATION MEASUREMENT UNDER	
PULSED HIGH MAGNETIC FIELD	
2.1 Outline of the System	7
2.2 Accuracy of the Measurement	17
2.3 Hysteresis Problems	22
2.4 Improvement of the Sensitivity	35
§3. MAGNETORESISTANCE MEASUREMENT UNDER	
PULSED HIGH MAGNETIC FIELD	
3.1 Outline of the System	45
3.2 Joule Heating of the Specimen due to	
the Eddy Current	50
§4. TEMPERATURE CONTROL TECHNIQUES UNDER	
PULSED HIGH MAGNETIC FIELD	
4.1 Outline of the System	55
4.2 Temperature Control Units	59
4.3 Magnetocaloric Effect under	
Pulsed Field Measurement	67
REFERENCES	75

PART II. FOUR-SPIN EXCHANGE IN EUROPIUM GRAPHITE

INTERCALATION COMPOUND C_6Eu

ABSTRACT	79
§1. INTRODUCTION	80
§2. CRYSTAL STRUCTURE AND MAGNETIC PROPERTIES OF C_6Eu	83
§3. RESULTS OF HIGH FIELD MAGNETIZATION MEASUREMENTS	87
§4. MAGNETIZATION PROCESS WITHOUT FOUR-SPIN EXCHANGE	90
§5. EFFECTS OF FOUR-SPIN EXCHANGE INTERACTIONS	102
§6. PHENOMENOLOGICAL CONSIDERATION	120
§7. CONCLUDING DISCUSSION	122
APPENDIX	123
REFERENCES	133

PART III. HIGH FIELD MAGNETIZATION OF RANDOMLY DILUTED

ANTIFERROMAGNET $Fe_{1-x}Zn_xF_2$

ABSTRACT	135
§1. INTRODUCTION	136
§2. CRYSTAL AND MAGNETIC STRUCTURES	139
§3. EXPERIMENTAL PROCEDURES AND RESULTS	
3.1 Experimental Procedures	142
3.2 Low Temperature Results	142
3.3 Phase Diagrams	153
§4. DISCUSSION	
4.1 FeF_2	158
4.2 Diluted Systems	160
REFERENCES	172
ACKNOWLEDGEMENTS	174

PART I

EXPERIMENTAL TECHNIQUES ON PRECISE MAGNETIZATION, MAGNETORESISTANCE MEASUREMENTS AND TEMPERATURE CONTROL UNDER PULSED HIGH MAGNETIC FIELD

ABSTRACT

Improvement in the magnetization measurement, and new techniques of the magnetoresistance measurement and temperature control under pulsed high magnetic field are described. Several tests are done on the flux compensation and data processing of the pick-up coil, and methods to improve the sensitivity and the accuracy are shown. Magnetoresistance measurement can be done up to 600 kOe. Specially designed temperature control units are combined with the large bore pulse-magnet and precise regulation of the specimen temperature is done within ± 0.1 K in the temperature range 4.2 K to 400 K under the field up to 400 kOe.

§ 1. INTRODUCTION

The magnetization processes and phase diagrams of magnetic materials have been the important subject of theoretical and experimental investigation in magnetism. A large amount of both theoretical and experimental work was performed on various kinds of ferro-, ferri- and antiferromagnets in the decades of 1950 and 1960 and various kinds of the magnetization processes, such as spin-flop or metamagnetic transitions, were found^{1,2)}. Technically speaking, however, the most experiments were done at low magnetic field region because the use of strong magnetic field was not so easy at that time. It is noted that the pulsed high magnetic field spin resonance was investigated in the decades and various kinds of antiferromagnetic resonance³⁾, spin-cluster resonance⁴⁾ and impurity localized magnon resonance⁵⁾ were found.

On the other hand, the technology in generating high magnetic field, both static and transient, has developed remarkably since 1960. Superconducting magnet up to 150 kOe is now commercially available, water-cooled Bitter type magnets are working in some magnet laboratories with steady field up to 220~250 kOe⁶⁾, and the highest steady field up to 300 kOe has been obtained by "hybrid magnet", a combined magnet of superconducting and water-cooled resistive solenoids⁷⁾. Magnetic field above 300 kOe is still now obtainable only transiently because of the Joule heat problem, and 0.1 sec pulsed field up

to 400 kOe⁸⁾, 1m~10msec pulsed field up to 400~500 kOe⁶⁾ are now available at several laboratories in the world. Most of these pulse-magnets, however, work only at low temperature in small bore of about 2 cm so that they are not suitable for temperature dependent measurements. The reliable field above 500 kOe is difficult to obtain in these coils because of huge Maxwell stress acting on the coil materials. Anyhow, the availability of those high magnetic fields has inspired the magnetization measurements on high T_N antiferromagnets^{9~11)}, rare earth and actinide compounds with new variations of magnetization process^{12~15)}, and metamagnetic materials with itinerant electrons^{16~19)}.

In Osaka University, the research on the generation of strong magnetic field and its application to the magnetic measurements started around 1970 by Date and his collaborators, and high field technology and physics have been developed since then. The principle of the field generation is characterized by the new method proposed by Date²⁰⁾ that 1MOe field can be produced by current controlled multi-layer coils without destruction of any part of the magnet or equipment. After several tests, the High Magnetic Field Laboratory has been founded as one of the facilities in the Faculty of Science at 1980. The laboratory now possesses three capacitor bank systems: D-1 with 250 kJ, D-2 with 1250 kJ and D-3 with 50 kJ energy sources. Three types of magnets are available for practical use: two-layer magnet 150(2L)20 for 700 kOe field in 2 cm bore,

single layer large bore magnet 150(1L)60 for 500 kOe in 6 cm bore and single layer magnet 100(1L)34 for 500 kOe in 3.4 cm bore.

The details about the construction of the capacitor banks and magnets are described in the previous paper by Mollymoto²¹⁾, which will hereafter be referred to as I. In addition to the field generation, various experimental techniques on magnetization, submillimeter ESR and optical measurements were also developed and applied to the magnetic studies. Some of the results are listed in I. As for the magnetization measurement, the induction method by highly balanced pick-up coil was established and experiments were done on various substances with the sensitivity of 5×10^{-6} emu/cm³ in susceptibility; at liquid helium or nitrogen temperature up to 600 kOe^{22~26)}.

Some advanced techniques were required after the above facility was established. One of them was the temperature control of the specimen, which is the inevitable technique for the investigation of magnetic phase diagrams. Usual pulse magnets generate field in very small space so that introduction of sufficient temperature control unit was difficult. Fortunately, the magnet 150(1L)60 in our laboratory has enough space so that precise temperature regulation under pulsed field was aimed. It was, however, not so easy because bulk metallic material can not be used due to the eddy current. Specially designed temperature control units were combined with large bore 150(1L)60 magnet and temperature regulation of the specimen in range 4.2 K to 400 K was realized in an accuracy ± 0.1 K up to

400 kOe. Another point was the improvement of the magnetization measurement system. The experiments increased both in number and variety. To perform them, Data Processor SM-1330, Iwatsu, was introduced and on-line data analysis was realized. Improvement in the sensitivity was done to cover magnetically dilute systems such as organic compounds of current interest^{27~29)}. Several tests on the flux compensation of the pick-up coil system were done and new type of pick-up coil was proposed, which improved the sensitivity more than five times better than the previous one. The pick-up coil succeeded to observe magnetic transition in spin-Peierls system $\text{MEM}-(\text{TCNQ})_2$. New technique for the magnetoresistance measurement was also developed, which was effectively employed in the observation of super to normal transition in type-II superconductors^{30,31)}, and spin fluctuation effects in weakly itinerant magnet³²⁾.

The present author joined the Date group in 1978 and has been concerned with these improvements of high field measurement technology, in addition to the experimental studies on magnetic phase transitions of magnetic materials under high field^{33~44)}. After short review of the system, various improvements in magnetization measurements are given in §2, where hysteresis problem pointed out in I is reexamined in detail and the possible origins are discussed. Other characteristics of the system concerning the accuracy of the measurement, which are not discussed in the previous paper I, are also shown. Magnetoresistance measurement techniques are given in §3, where

problems arising from the eddy current in the conductive specimen are also discussed. Final section is devoted for the techniques of temperature control under pulsed magnetic field. Specially designed temperature control units for magnetization and magneto-resistance measurements are shown. In addition, technical difficulty coming from an adiabatic condition under pulsed field is explained and example of the correction method is given.

New results of magnetic phase transitions in localized spin systems are described in the following two parts of this paper. In PART II, magnetization process and the analysis of europium graphite intercalation compound C_6Eu are given. Metamagnetic plateau with $1/3$ moment of the saturated value is found in the c-plane magnetization process of the triangular spin lattice, which is explained by weak four-spin exchange interactions among localized Eu spins. Magnetization processes of diluted high anisotropy antiferromagnet $Fe_{1-x}Zn_xF_2$ are described in PART III, where new phenomena of field induced single-spin exchange flips are shown. Hysteresis effect in a field region is observed in the magnetization process with anomalous peak in dM/dH_0 , and this is explained by the order-disorder transition in the random spin system.

§2. MAGNETIZATION MEASUREMENT UNDER PULSED HIGH MAGNETIC FIELD

2.1 Outline of the System

The magnetization measurement is done using a balanced pick-up coil. The technically important point is how to compensate background flux change due to a transient field, which is usually $10^4 \sim 10^6$ times larger than the flux change due to the magnetization of the specimen. This is usually done by setting three coils as are shown schematically in Fig.1 (a). Coil A picks up the magnetic flux change of the specimen while coil B is wound in the opposite direction to A in order to compensate the background flux change. Fine adjustment is done by one loop coil C taking a bridge balance as shown in the figure. The sensitivity of the measurement strongly depends on the arrangement of these coils. The detailed discussion will be given in 2.4. Figure 1(b) is the cut view of the standard pick-up coil which has been used in our laboratory. Considering the field duration and frequency response, coil A is wound with 100 turns. The inner diameter is 4 mm for D-1 and D-2 1L magnets, and 3 mm for D-2 2L magnet. The coil B is coaxially wound on A with 50 turns oppositely. The cross section of coil B is twice as large as that of A so as to make the net flux in A equal to that in B. Fine adjustment coil C is wound on B. The coil wire material is urethane coated 2% tin-doped Cu of 0.1mm D. The wire has large residual resistivity ($2.5 \mu\Omega\text{cm}$) and is effective to improve the flux compensation

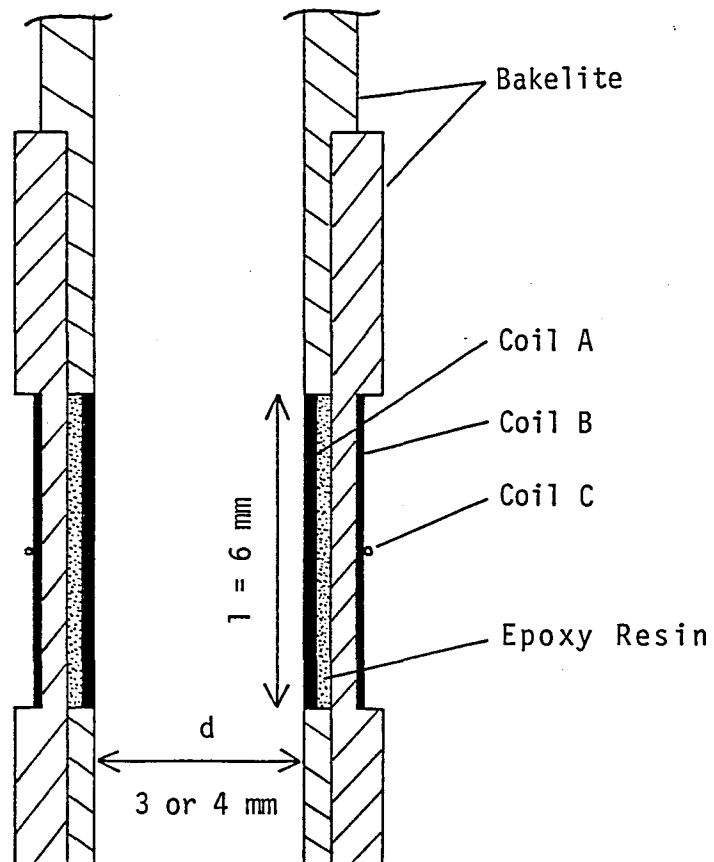
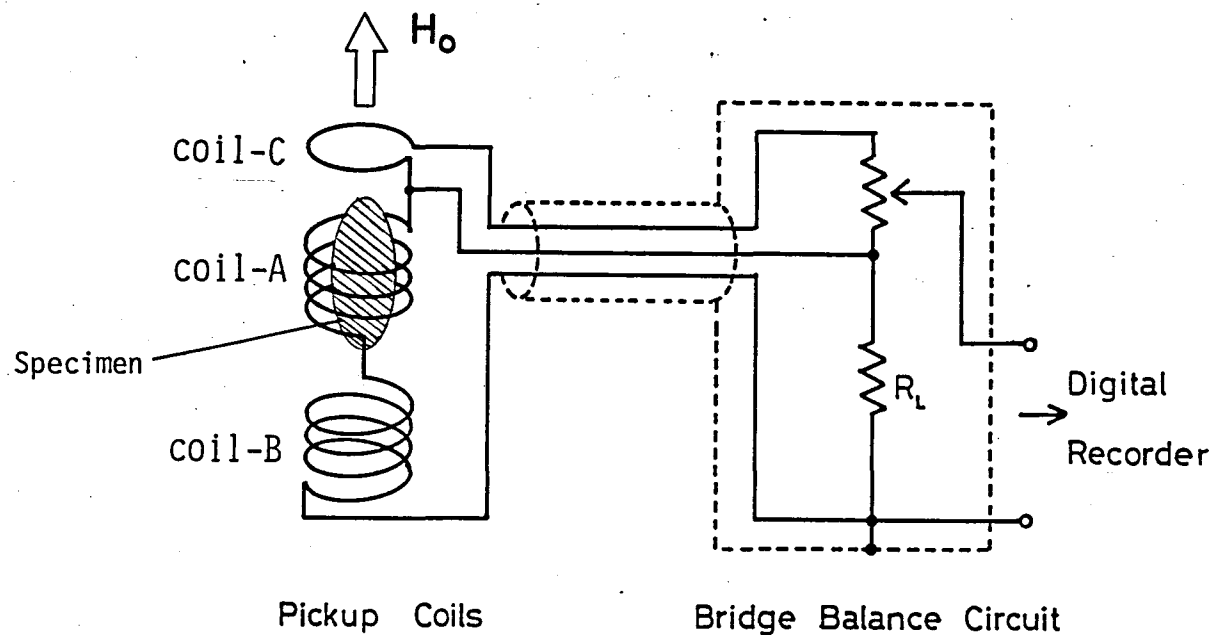


Fig.1 Method of flux compensation and cut view of standard pick-up coil.

especially at liquid helium temperature. The standard pick-up coil attained a flux compensation of $10^{-4} \sim 10^{-5}$ at the signal output of the bridge balance circuit.

Figure 3 is a block diagram of the system, where a cut view of a cryostat is also shown schematically. Three signal outputs of the pick-up coil (A) are shielded by a copper capillary (B) in the cryostat and are connected to double shield cable (C) and transmitted to the bridge balance circuit. The balanced signal is then stored in a digital recorder, IWATSU DM-901. The digital recorder consists of 8-bit A-D converter and 1024×2 words digital memory, and can record transient events with a minimum time resolution of 10 ns. Usual measurements are done at the time resolution of 200~500 ns. A specimen (D) is mounted on the tip of glass rod (E) by a teflon tube and driven by a miniature motor (F) for insertion and adjustment at the right position. Usually a specimen whose length is $10 \sim 15$ mm and diameter of $2.5 \sim 3.2$ mm is used. The accuracy of the measurement depends on the size as will be shown in 2.2. The pick-up coil is found to be very sensitive to the axial displacement so that it is suspended by a quartz pipe (G) that has small coefficient of thermal expansion. A magnetic field is monitored by a single loop field pick-up coil (H). The output signal (proportional to dH/dt) is integrated by a high speed operational amplifier and also stored in the digital recorder. The time-constant of the integrator is taken as 300 times longer than the field duration time.

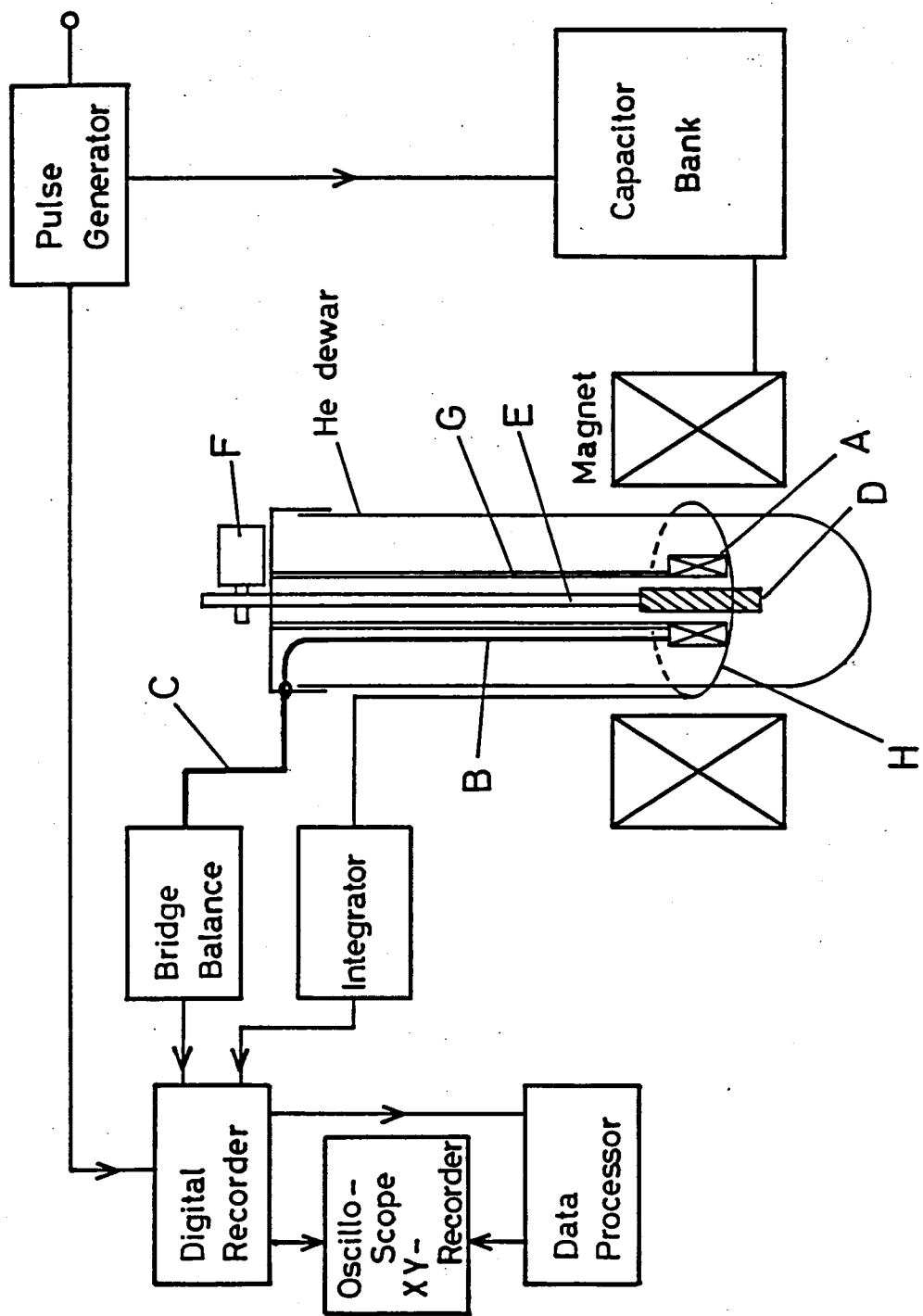


Fig. 2 Block diagram of magnetization measurement system.

Short time-constant will cause an apparent hysteresis in the magnetization, as will be discussed in 2.3. The field calibration is done at 283 kOe by submillimeter ESR of paramagnetic $\text{CuCl}_2 \cdot 2\text{H}_2\text{O}$.

The output signal of the bridge balance circuit is proportional to dM/dt but still contains background noise. Further noise reduction is done by Data Processor SM-1330, IWATSU. Using two shots of pulsed field generation, two sets of data, with and without the specimen are taken. These are transferred to the Data Processor and the subtraction of the background and the integration of dM/dt are done there. The Data Processor enable one to analyze and check the data immediately, and improves the efficiency of the experiment greatly. In this manner, sufficiently high sensitive measurement can be done under the final effective flux compensation of 10^{-6} . This corresponds to the sensitivity of 5×10^{-6} emu/cc in a susceptibility measurement. Further improvement in the sensitivity will be discussed in 2.4.

An example of the data processing is shown on a trinuclear complex salt $[\text{Cr}_3\text{O}(\text{CH}_3\text{COO})_6(\text{H}_2\text{O})_3]\text{Cl} \cdot 6\text{H}_2\text{O}$. This complex consists of nearly free trimeric cluster of Cr^{3+} . Each Cr^{3+} ion possesses spin $s=3/2$ and antiferromagnetically couples to each other in the cluster. Therefore, the ground state of the cluster has net spin $S=1/2$ and there is an excited state with $S=3/2$. Applying strong field, level crossing between Zeeman splitted $S=1/2$ and $S=3/2$ levels will occur and large increase

in the magnetization will be expected. Fig.4 shows an example of the data stored in the digital recorder after two shots of pulsed field generation. Figure 4(a) shows the two outputs with (curve A) and without (curve B) a specimen, while (b) is the trace of the applied field. These signals A and B are transferred to the Data Processor and subtraction A-B is done there, resulting in a background noise reduced datum shown in (c), which is proportional to dM/dt . Integrating (c) with respect to t , residual fine noise in curve (c) is averaged and smooth magnetization change can be obtained as a function of time (d). Plotting it against field (b), the magnetization curve is given. The result is shown in Fig.5. The initial stage of the magnetization process corresponds to the paramagnetic saturation of the ground state doublet which completes at about 80 kOe. The large increase in the moment from $1\mu_B$ to $3\mu_B$ per cluster, coming from the level crossing of $S=1/2$ and $S=3/2$ states, is clearly observed between 260 kOe and 380 kOe. The energy gap between $S=1/2$ and $S=3/2$ levels is obtained as $30 \pm 4 \text{ cm}^{-1}$.

When one wants to investigate magnetic phase transitions, it is sometimes convenient to examine differential susceptibility dM/dH rather than integrated magnetization curves. The Data Processor can easily display dM/dH as a function of the field by dividing dM/dt by dH/dt . An example on a diluted antiferromagnet $\text{Fe}_{0.1}\text{Zn}_{0.9}\text{F}_2$ is shown in Fig.6. Figure 6(a) is the magnetization curve, which shows almost continuous increase up to 400 kOe. On the other hand, (b) is the

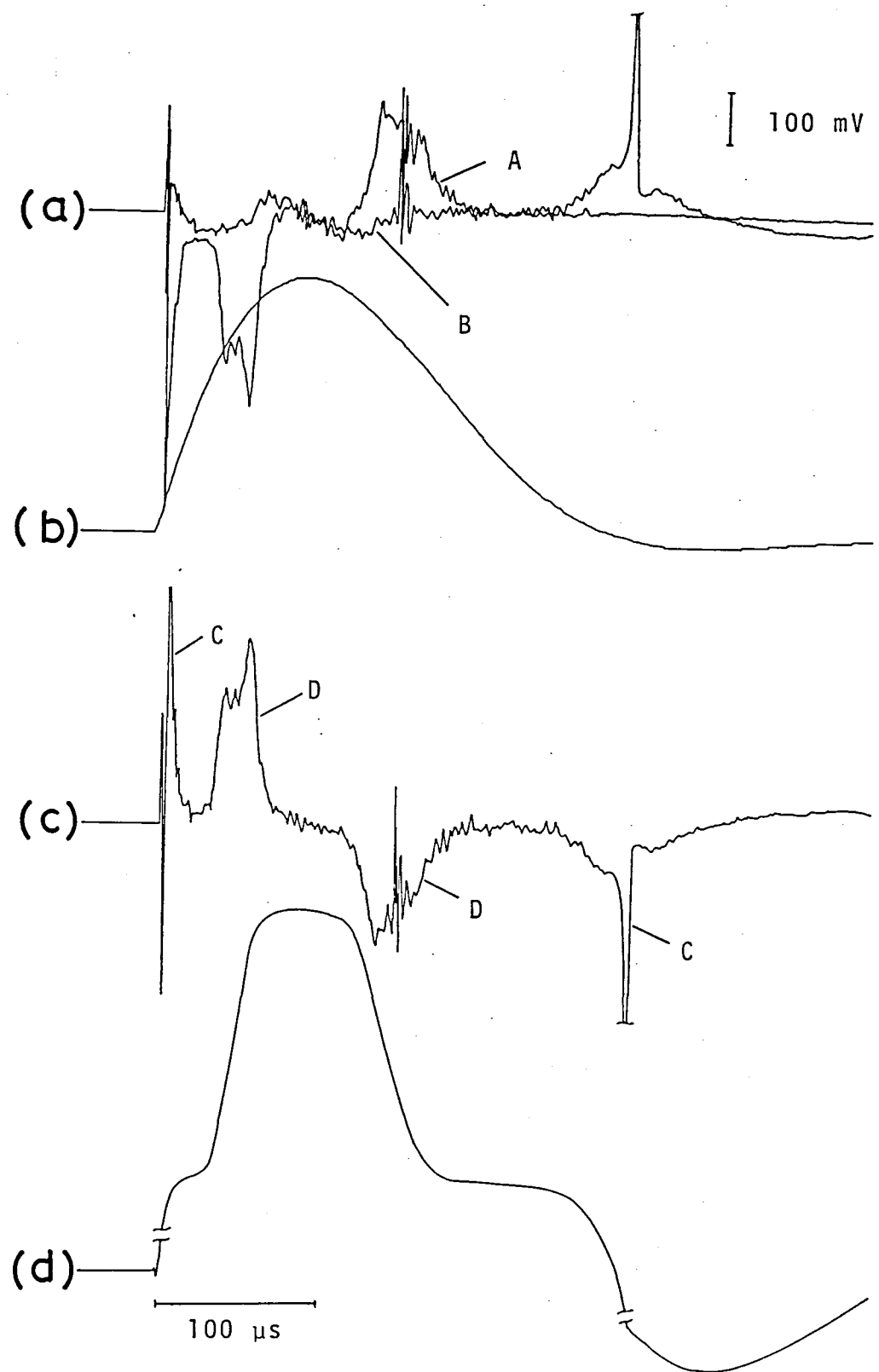


Fig.3 Example of data processing on $[\text{Cr}_3\text{O}(\text{H}_2\text{O})_3(\text{CH}_3\text{COO})_6]\text{Cl} \cdot 6\text{H}_2\text{O}$. Two signals A and B shown in (a) are obtained by applying two shots of pulsed field (b), with and without a specimen in a pick-up coil, respectively. Background reduced dM/dt is given in (c) and integrated magnetization is shown in (d). Peaks in (c) indicated by C correspond to the paramagnetic saturation of the ground state doublet, while D indicates the peaks that come from the level crossing explained in the text.

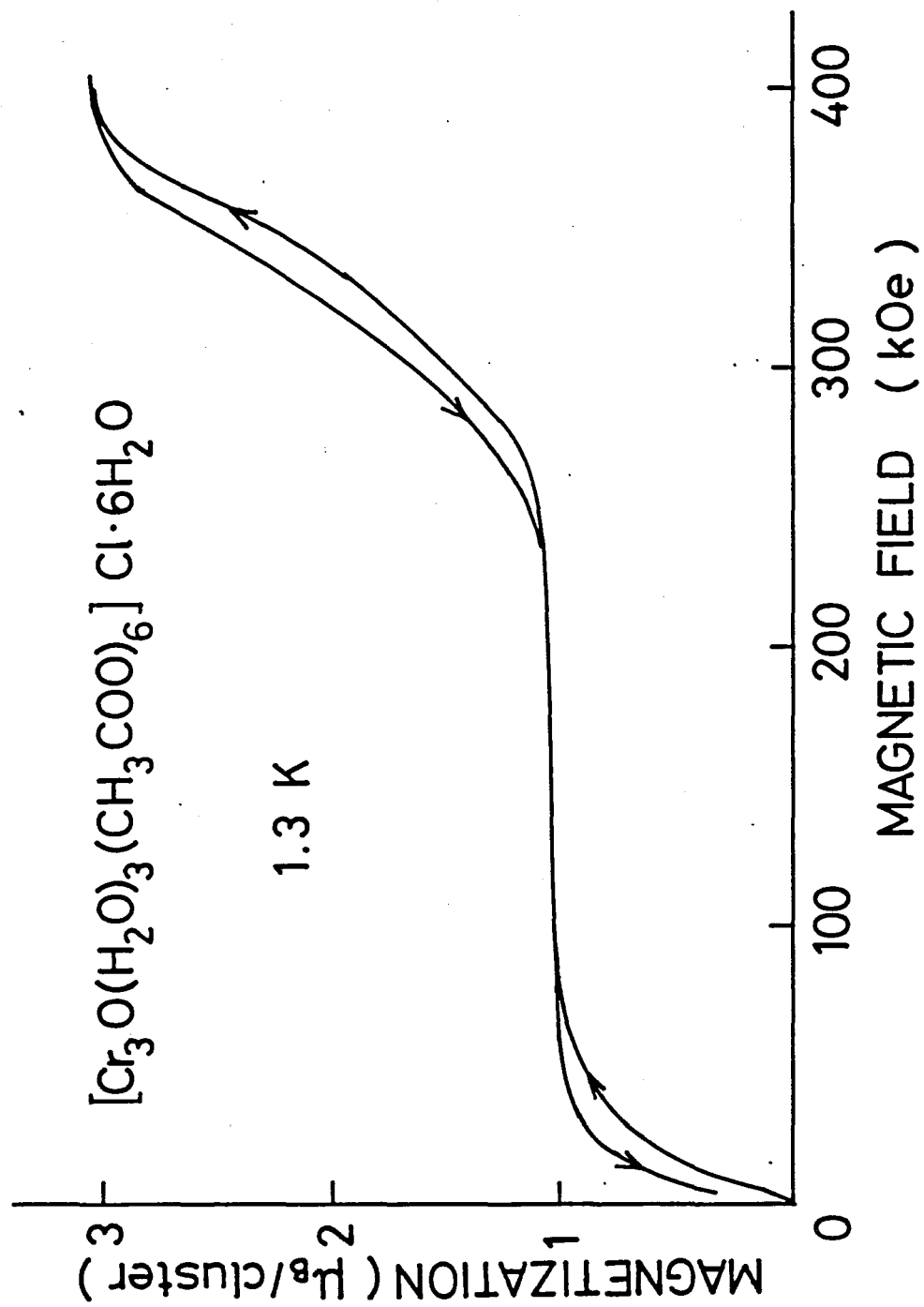


Fig.4 Magnetization of trimeric complex $[\text{Cr}_3\text{O}(\text{H}_2\text{O})_3(\text{CH}_3\text{COO})_6] \text{Cl} \cdot 6\text{H}_2\text{O}$.

corresponding dM/dH curve. There can be seen small but distinct peak in dM/dH indicated by arrows ($N=1, 2$ and 3). These peaks come from the exchange flips in high anisotropy diluted antiferromagnet. The detailed results and discussions will be given in Part III.

The calibration of magnetization value is done by single crystalline $\text{CuCl}_2 \cdot 2\text{H}_2\text{O}$ or MnF_2 as the standard specimen. An integrated output signal is proportional to a magnetization M , cross sectional area S and demagnetization correction term α of a specimen so that one can obtain the magnetization value by comparing these values with those of the standard specimen. The accuracy of the measurement depends on the geometrical condition of the specimen and an apparent hysteresis in the magnetization curve. These points are discussed in detail in 2.2 and 2.3.

Three types of cryostats are available now. Usual measurements at temperature ranges 1.3 K to 4.2 K and 77 K to R.T. are done using D-1 1L magnet up to 400 kOe or D-2 2L magnet up to 600 kOe. The measurements under precise temperature control are done using D-2 1L large bore magnet and temperature controlled cryostat. The details of the latter cryostat will be given in §4.

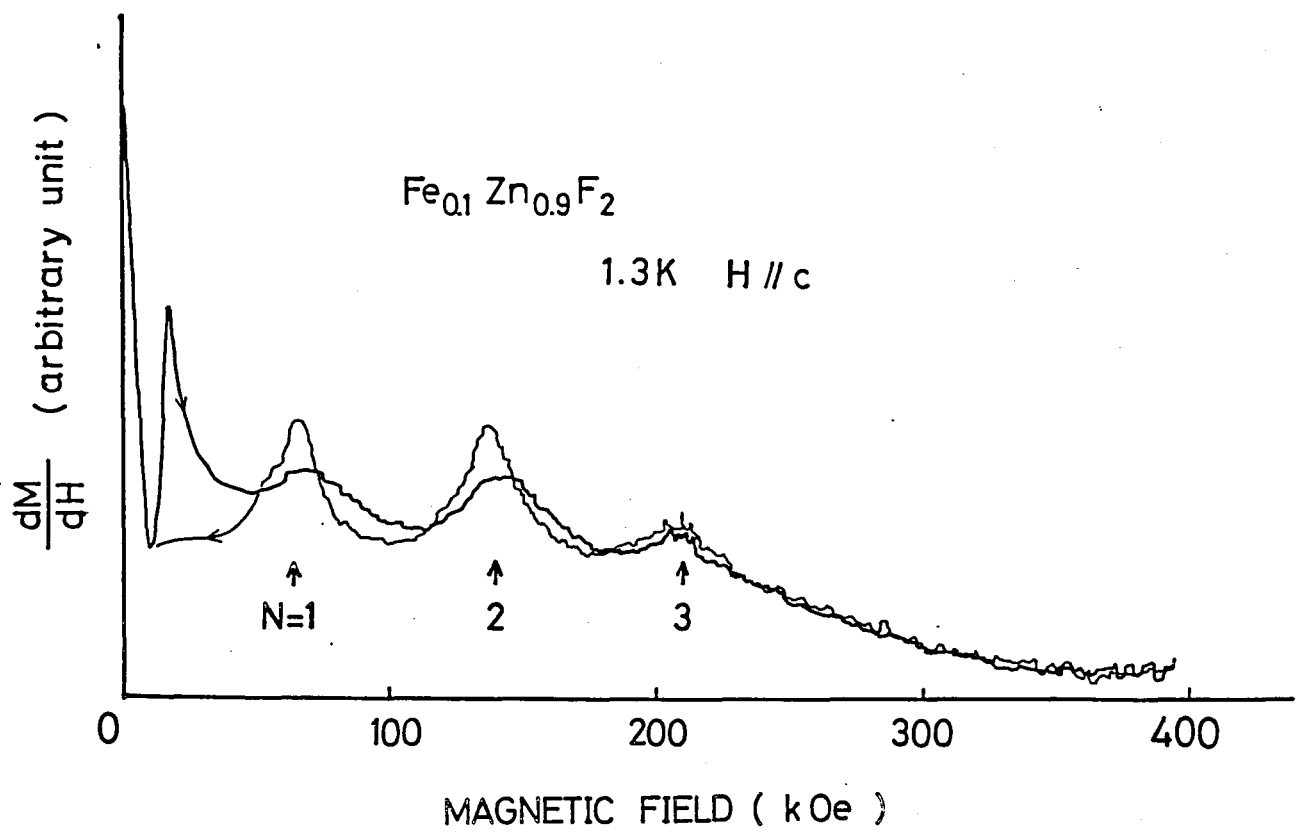
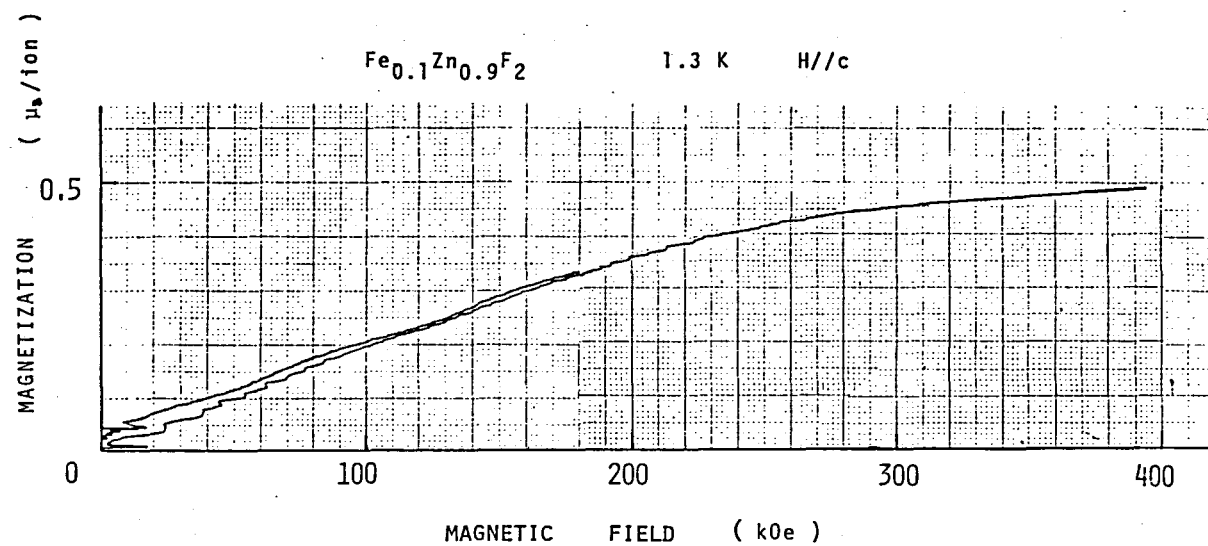


Fig.5 Magnetization of $\text{Fe}_{0.1}\text{Zn}_{0.9}\text{F}_2$ (upper) and the corresponding dM/dH (lower).

2.2 Accuracy of the Measurement

As is mentioned in the preceding subsection, magnetization of a specimen is obtained by integrating dM/dt output of a pick-up coil. The integrated output is proportional to αMS , where M is the magnetization, S is the cross sectional area and α is the demagnetizing field correction factor of the specimen, respectively. Magnetization value is determined by comparing these values with those of a standard specimen so that the accuracy of the magnetization depends on the estimation of S and α . Besides these geometrical factors, signal delay in the measurement system sometimes cause an apparent hysteresis in the magnetization curve and reduces the accuracy as is pointed out in the previous work I. In this subsection, we first consider the accuracy of the geometrical factors and show the practical methods for the precise measurement. The detailed discussions on the hysteresis problem will be given in 2.3.

a) Cross sectional area

The cross sectional area of a bulk homogeneous specimen, such as a single crystal material, can be precisely measured as follows. First the specimen is cut into a cylindrical shape with the diameter of 2~3 mm and the length of 15 mm(the section is not necessarily a circle). Next, both ends of the cylinder are polished into flat surfaces perpendicular to the cylinder axis. The cross sectional area S is then given by

$$S = W/L\rho_s , \quad (1)$$

where W is the weight and L is the length of the cylinder and ρ_s is the specific gravity of the material. S can be determined in an accuracy of $\pm 1 \sim \pm 2 \%$.

Powdered specimen is usually cast into a cylinder with an adhesive. Both ends of the cylinder are also polished and the effective cross sectional area S_{eff} is given as

$$S_{\text{eff}} = \frac{W}{L\rho_s} \frac{1}{1+k} , \quad (2)$$

where W is the total weight of the cylinder and k is the weight ratio of the adhesive to the specimen. In this case, the accuracy of S_{eff} is somewhat worse than the previous case because of an inhomogeneity in the density.

b) Demagnetizing field correction

The output signal of a pick-up coil does not depend on the length of the specimen L so long as L is much larger than the length of the pick-up coil. However, some correction for the demagnetizing field is necessary for a short specimen.

Generally speaking, a flux density within a magnetized material is given by $(1-N)M$, where N is the demagnetizing factor of the specimen. However, the output signal of a coaxial type pick-up coil is not proportional to $(1-N)$. We have determined the correction term α experimentally for a standard coaxial type pick-up coil as follows. We prepared a powdered specimen of metallic Co and cast it into a cylinder of 2.8 mm D and 40 mm L with Araldite. The spontaneous magnetization is measured

as a function of a specimen length L by successively shortening the specimen. A standard pick-up coil whose length is 6 mm and the inner diameter of 4 mm is used for the measurement. Figure 6 shows the results. When L is longer than 15 mm, no change over than 0.5 % in the output signal is observed. Therefore, α is substantially unity for $L > 15$ mm. On the other hand, the output, or α , rapidly decreases as L become shorter than 12 mm. The broken line in the figure denotes the L dependence of the factor $(1-N)$ for comparison, where N of an ellipsoid is used approximately. It is clear from the figure that α approaches unity faster than $(1-N)$ as L becomes longer than the pick-up coil length. This may because the magnetic flux produced by the surface magnetic charge of the specimen (demagnetizing field) is compensated by the coil B (see Fig.1) of the pick-up coil. It is found that L of 15 mm is enough for the precise magnetization measurement. On the other hand, α should be estimated carefully for $L < 12$ mm, according to Fig.6. The factor α of course depends on a diameter D of a specimen but it did not change widely for D between 2mm and 3mm.

Figure 7 shows the specimen position dependence of the output. As can be seen from the figure, output of a short specimen becomes very sensitive to the position. For example, displacement of 0.5 mm from the center of the pick-up coil will cause a reduction of 2 % in the signal for $L=5$ mm, so that one should be carefull for the setting.

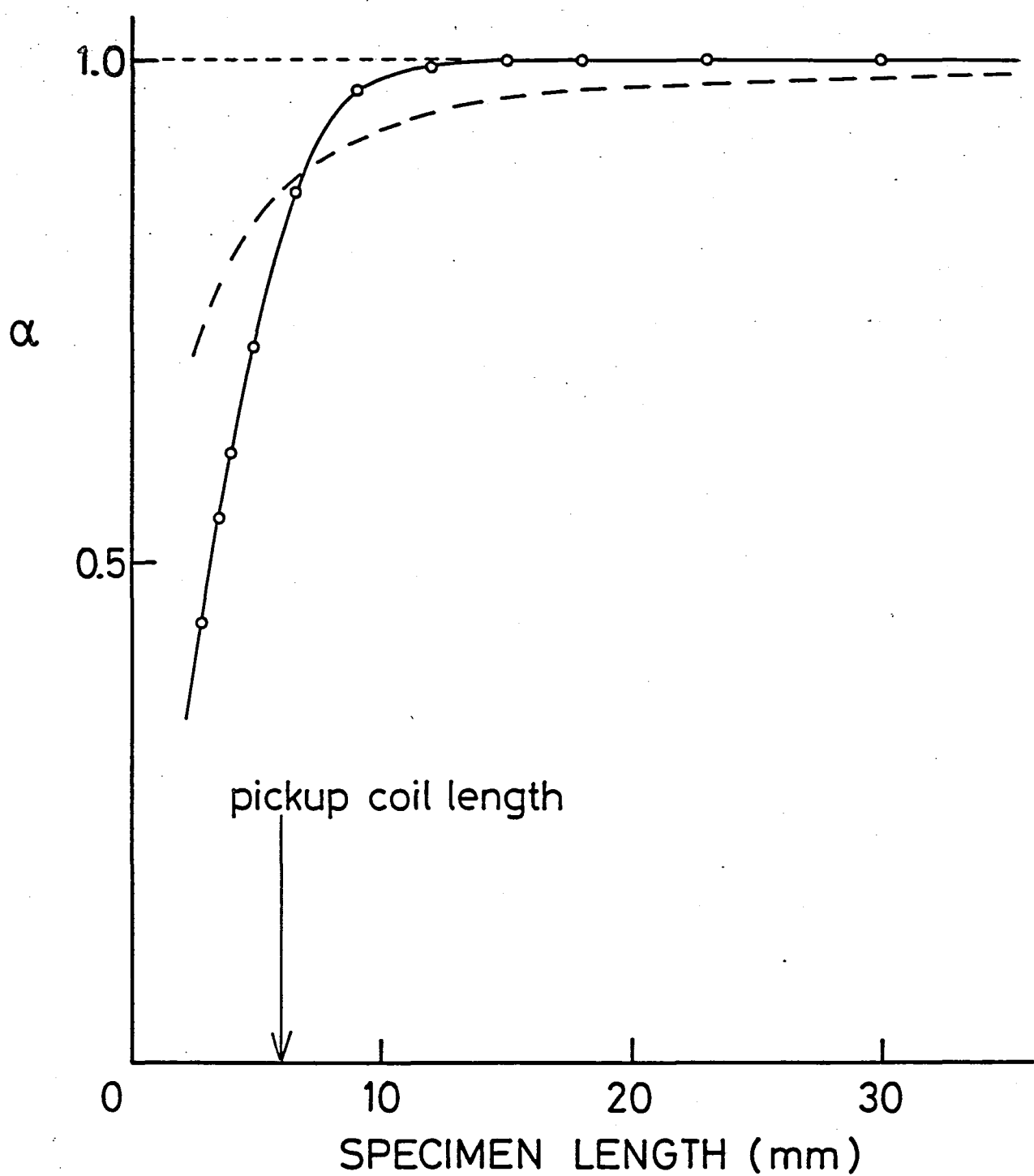


Fig.6 Demagnetizing field correction term α as a function of specimen length. Broken line is explained in the text.

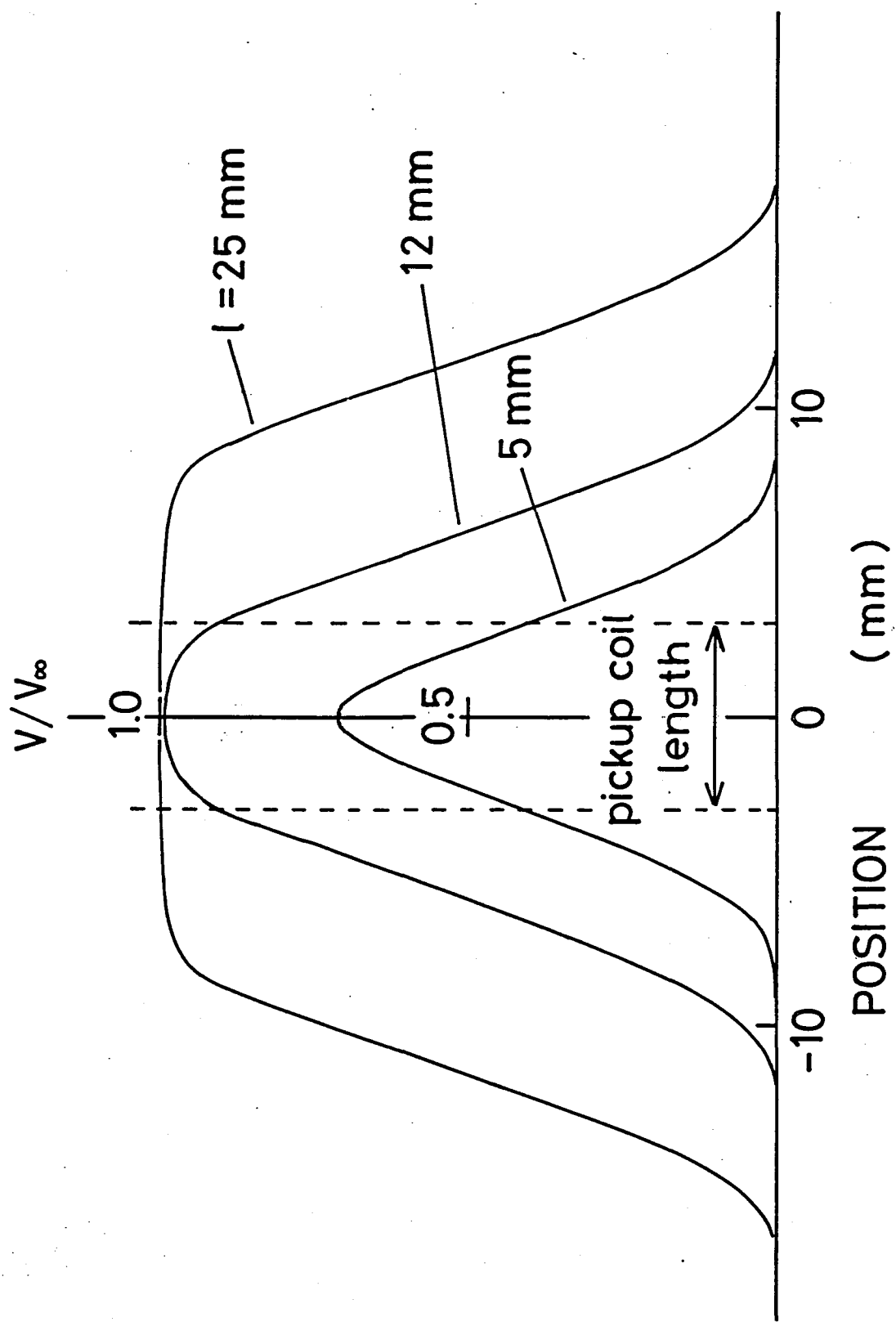


Fig. 7 Output of the pick-up coil versus position of the specimen with various length l . The output is normalized by the value at $l=\infty$.

2.3 Hysteresis Problems

As has been pointed out by Mollymoto²¹⁾, magnetizations obtained under a pulsed field sometimes show apparent hysteresis. For example, antiferromagnetic to paramagnetic critical field of $\text{CuCl}_2 \cdot 2\text{H}_2\text{O}$ showed a hysteresis of about 5 kOe in the previous work. It was a serious problem for the precise measurement. In this subsection, possible origins of the systematic hysteresis are considered in detail. These are removed now to some extent in the measurement.

a) Time constant of a field integrator

Pulsed magnetic field is measured by integrating dH/dt induced in a field pick-up coil with a Miller-type integrator. Defining τ as a time constant (time of discharge) of the integrator and T as the pulse field width, error of the order of T/τ is expected in the field measurement and this may cause hysteresis. This effect is first considered.

Figure 8 shows a response of an integrator whose time constant is τ and gain A_0 , to a square pulse input of magnitude v and width Δt ($\Delta t \ll \tau$). Output voltage increases linearly up to $A_0 v \Delta t / \tau$ and then decay exponentially with time constant τ . By superposing it, the response for a general input $v(t')$ ($t' > 0$) is given as

$$v(t) = \int_0^t A_0 v(t') \exp(-(t-t')/\tau) / \tau dt'. \quad (3)$$

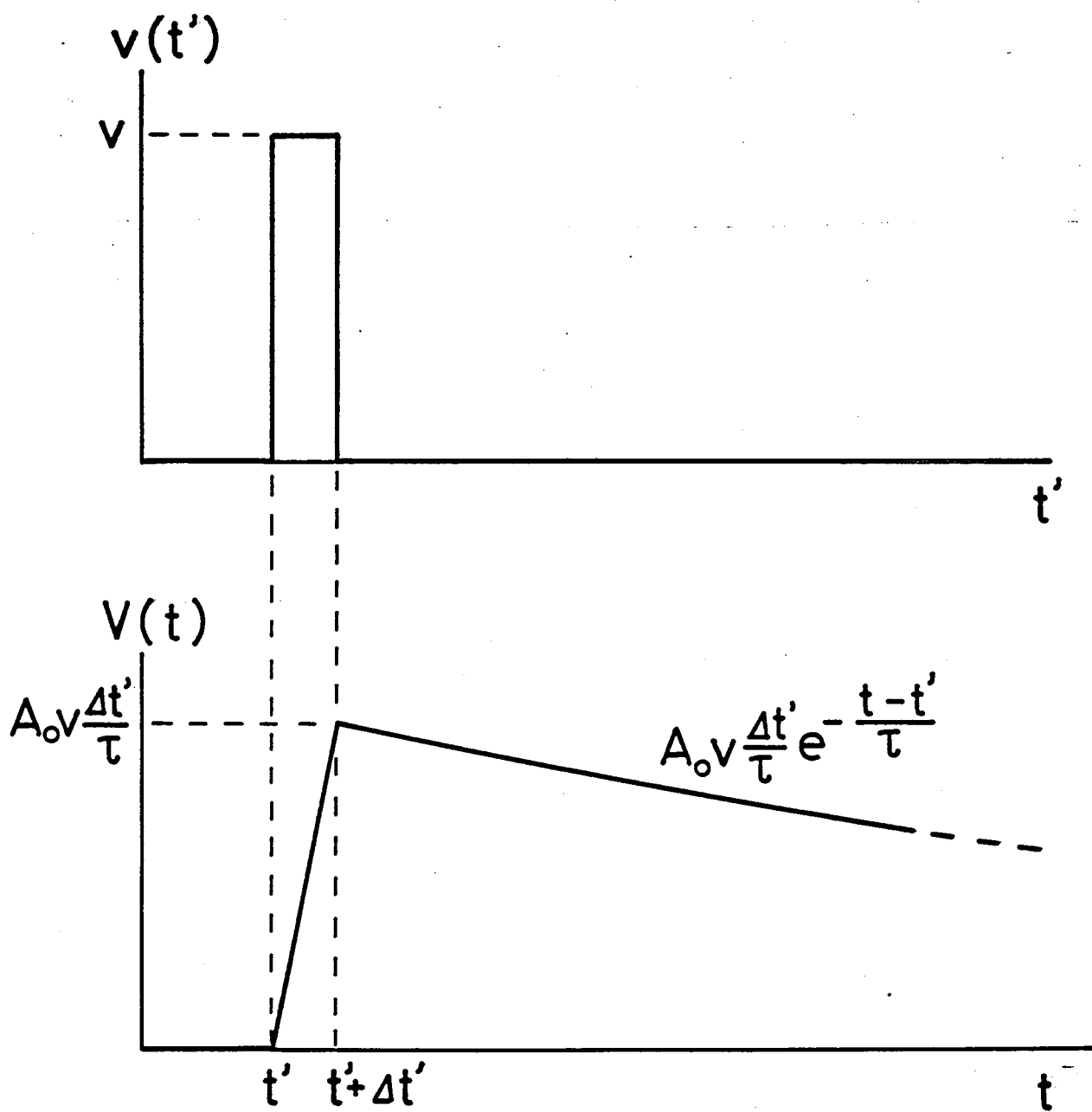


Fig. 8 Response of a integrator with time constant τ and gain A_0 , to a square pulse input with the width Δt ($\Delta t' \ll \tau$).

We now assume the field as

$$H_o(t) = H_o \sin(\pi t/T), \quad (0 < t < T). \quad (4)$$

The corresponding induced voltage of a field pick-up coil of unit cross section is

$$dH/dt = H_o \frac{\pi}{T} \cos(\pi t/T), \quad (0 < t < T). \quad (5)$$

The output of the integrator then becomes

$$\begin{aligned} v(t) &= \frac{A_o H_o \pi}{\tau T} \int_0^t \cos(\pi t'/T) e^{-(t-t')/\tau} dt' \\ &= \frac{A_o H_o}{\tau} \left[\sin(\pi t/T) + \frac{T}{\pi \tau} \cos(\pi t/T) - \frac{T}{\tau} e^{-t/\tau} \right]. \quad (6) \end{aligned}$$

The first term in the parentheses is the true integrated result and the others are error terms. These are explained in Fig.9. Dashed line of Fig.9 (a) is the true field trace and solid line is the real output of the integrator. When the time constant is not long enough ($\tau/T=7.5$ in Fig.9 (a)), the real output will return to zero faster than the true field and this will cause an apparent hysteresis in the measurement. The contribution of the error terms is shown in Fig.9 (b). In the previous measurement in I, τ/T of 50 was adopted. This value is found to be too small for the precise measurement because it makes error of more than 1 %. The time constant τ is now taken as 300T and the corresponding error is about 0.2 %, which value

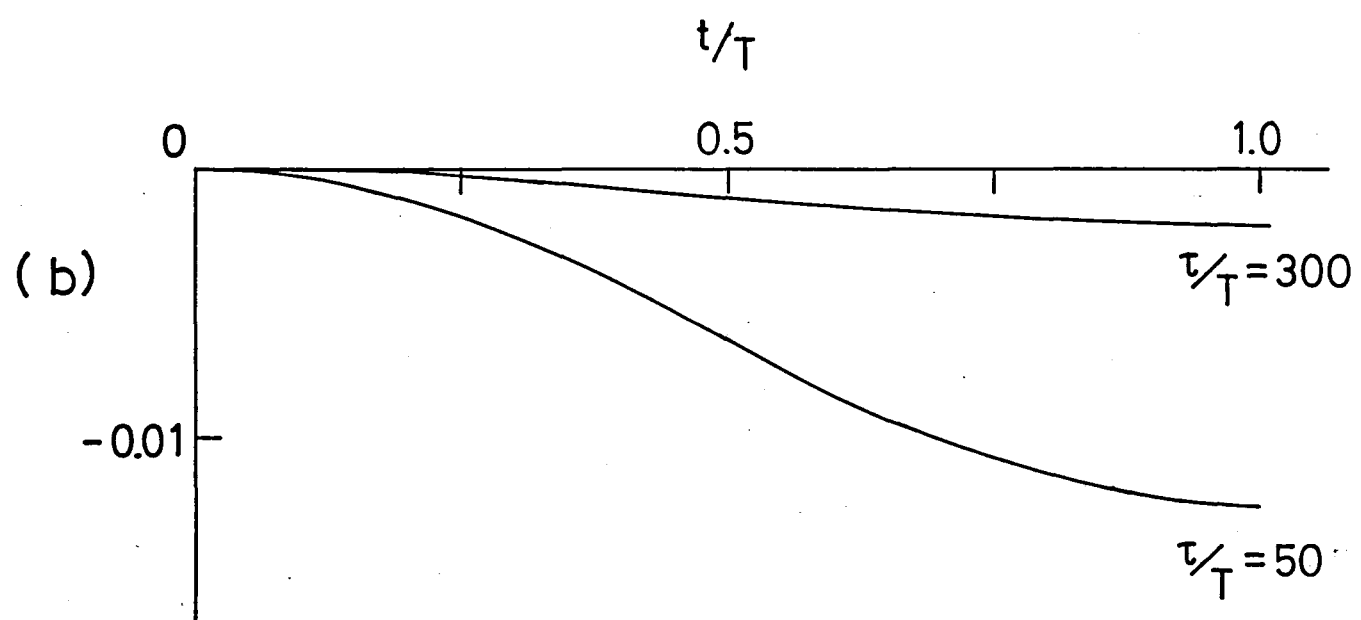
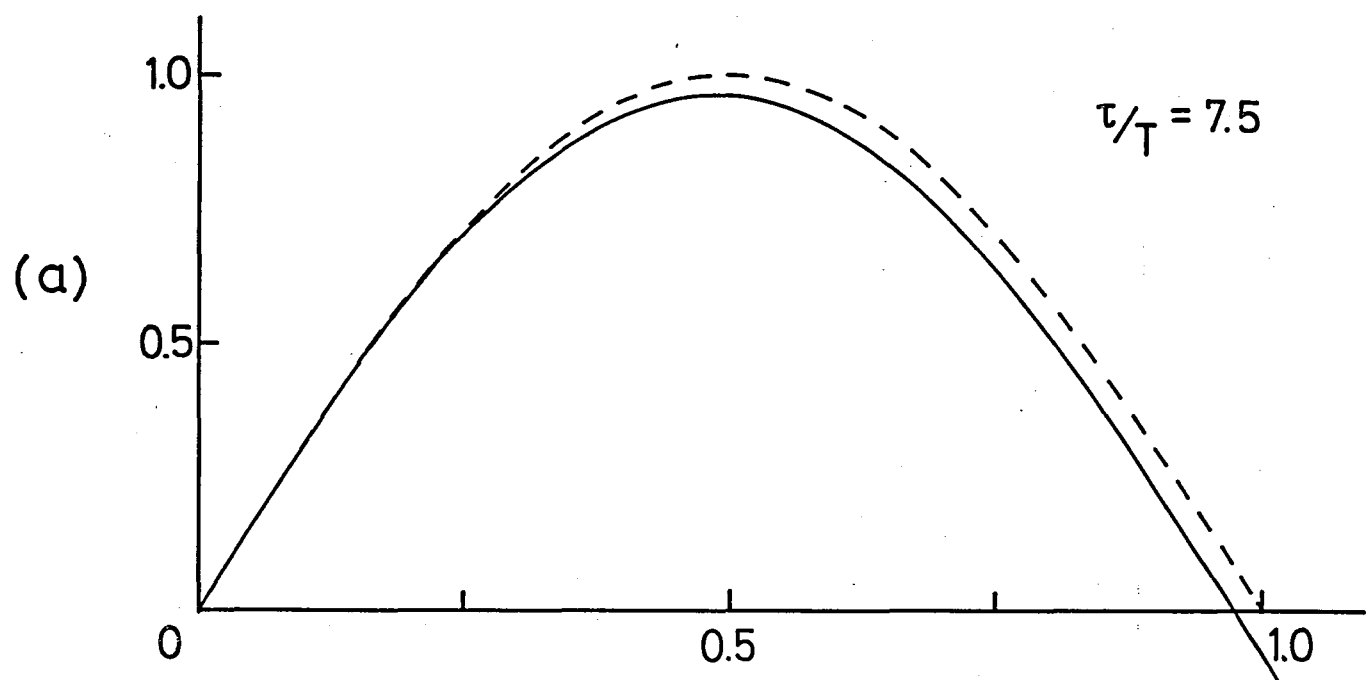


Fig.9 Response of the integrator (time constant τ) to a sinusoidal pulse with width T . The results for $\tau/T=7.5$ (solid line) and the ideal case $\tau/T=\infty$ (dashed line) are compared in (a). Error in the output is shown in (b) for two cases, $\tau/T=50$ and $\tau/T=300$.

is smaller than the error in field calibration by the sub-millimeter ESR.

b) Error in the integration of dM/dt

Magnetization curve is usually obtained by numerical integration of digitally recorded dM/dt signal. In the A-D conversion process of dM/dt signal, quantizing error of an order of $1/2^m$ is introduced where m is a quantization bit number. In our case m is 8 so that the quantizing error of dM/dt is smaller than 1 %. However, this error is sometimes accumulated in the integration process and results in a large hysteresis. Figure 10 shows examples on the magnetization of antiferromagnetic $\text{CuCl}_2 \cdot 2\text{H}_2\text{O}$. Field is applied along c axis at 1.3 K. Curve A is obtained by digital integration of dM/dt in a usual manner. The magnetization shows rather large hysteresis of about 5 kOe in a low field region. On the other hand, curve B is taken from direct integration of pick-up coil output by an integration circuit. Curve B shows no hysteresis at low field. Therefore, it may be concluded that an apparent hysteresis in A is produced during the data processing. This kind of error becomes serious especially when there are sharp and large peaks in dM/dt , such as spin flop or metamagnetic transition of an antiferromagnet. Analog integration is found to be very effective in such cases.

Curve B in Fig.10 still has hysteresis of about 3 kOe around the critical field to the paramagnetic state. This value is smaller than the previous result²¹⁾, but there still may be some

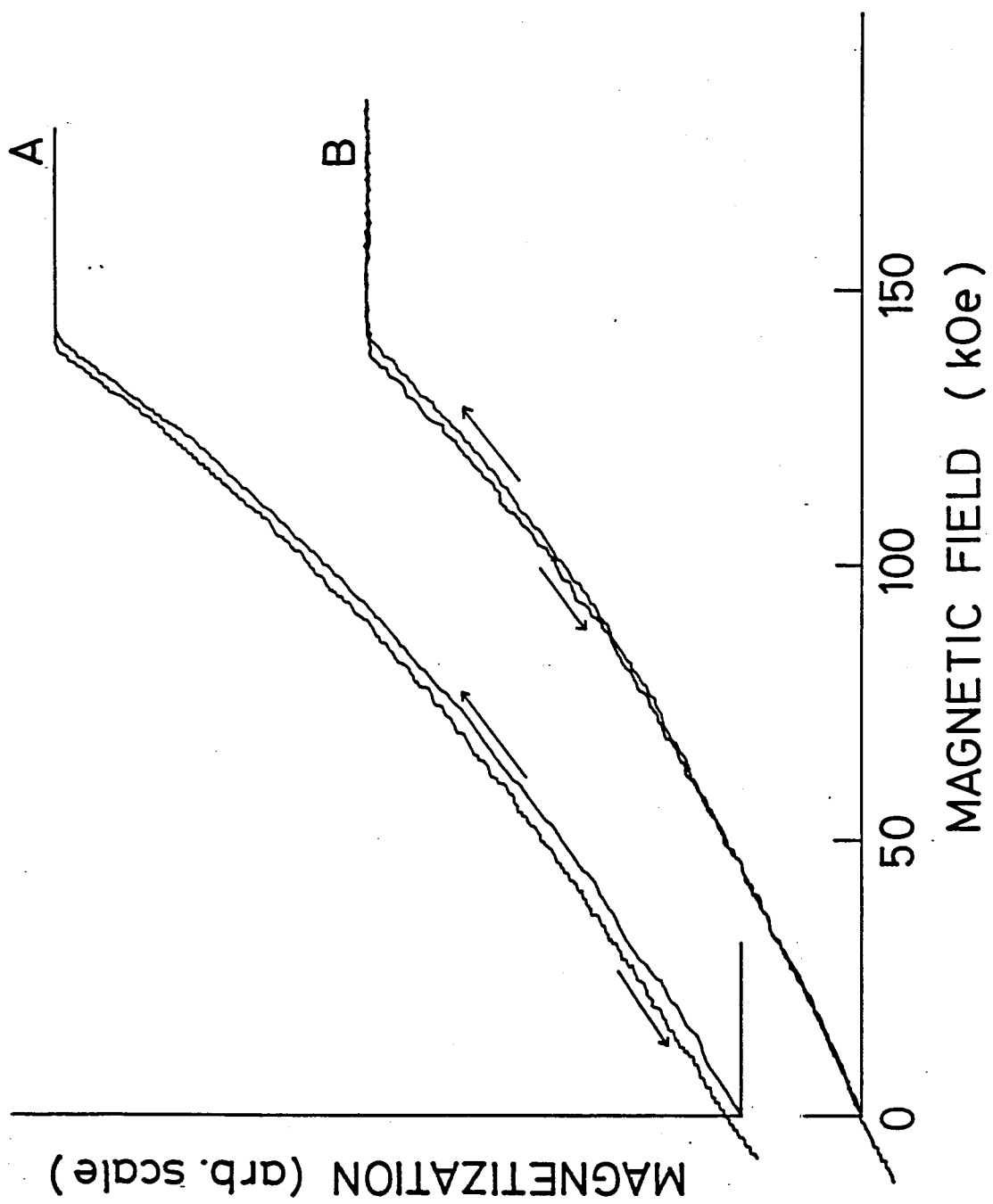


Fig. 10 Magnetization curves of CuCl₂ 2H₂O (H₀ // c) measured at T=1.3 K. A is obtained by digital integration of dM/dt data, while analog integrator is used in B.

delay in the detecting system. This point is considered next.

c) Signal delay in the pick-up coil system

As is pointed out in I, self inductance L_s of a compensated pick-up coil is not zero. A stray capacitance of a signal transmission line and a matching load resistor, together with L_s form a LCR network and there should be some amount of signal retardation. Figure 11 shows the simplified equivalent circuit. The self inductance of the coils A and B is L_s , and r is their internal resistance while L_s' and r' are those of fine adjustment coil C. C_s and C_s' are the stray capacitance of the signal transmission lines. The value L_s of the standard pick-up coil was measured as $11\mu\text{H}$, C_s is a few thousands of pF and the matching load resistor R_L is usually chosen as 50Ω so that a delay of a fraction of μs may be expected. As the field sweep rate amounts to $1\sim 3 \text{ kOe}/\mu\text{s}$, a delay of $1 \mu\text{s}$ will cause hysteresis of several killo-Oersted. Therefore, precise estimation of the delay time becomes important. This was experimentally done as follows.

The experimental set up and examples of the results are shown in Fig.12. Several turns of wire is wound around a ferrite core that can be used under radio-frequency, and is connected to a triangular wave oscillator. The frequency is chosen as about 150 KHz and the output current is monitored through a shunt resistor of 50Ω . The ferrite core is weakly coupled to the pick-up coil and the output dM/dt is measured

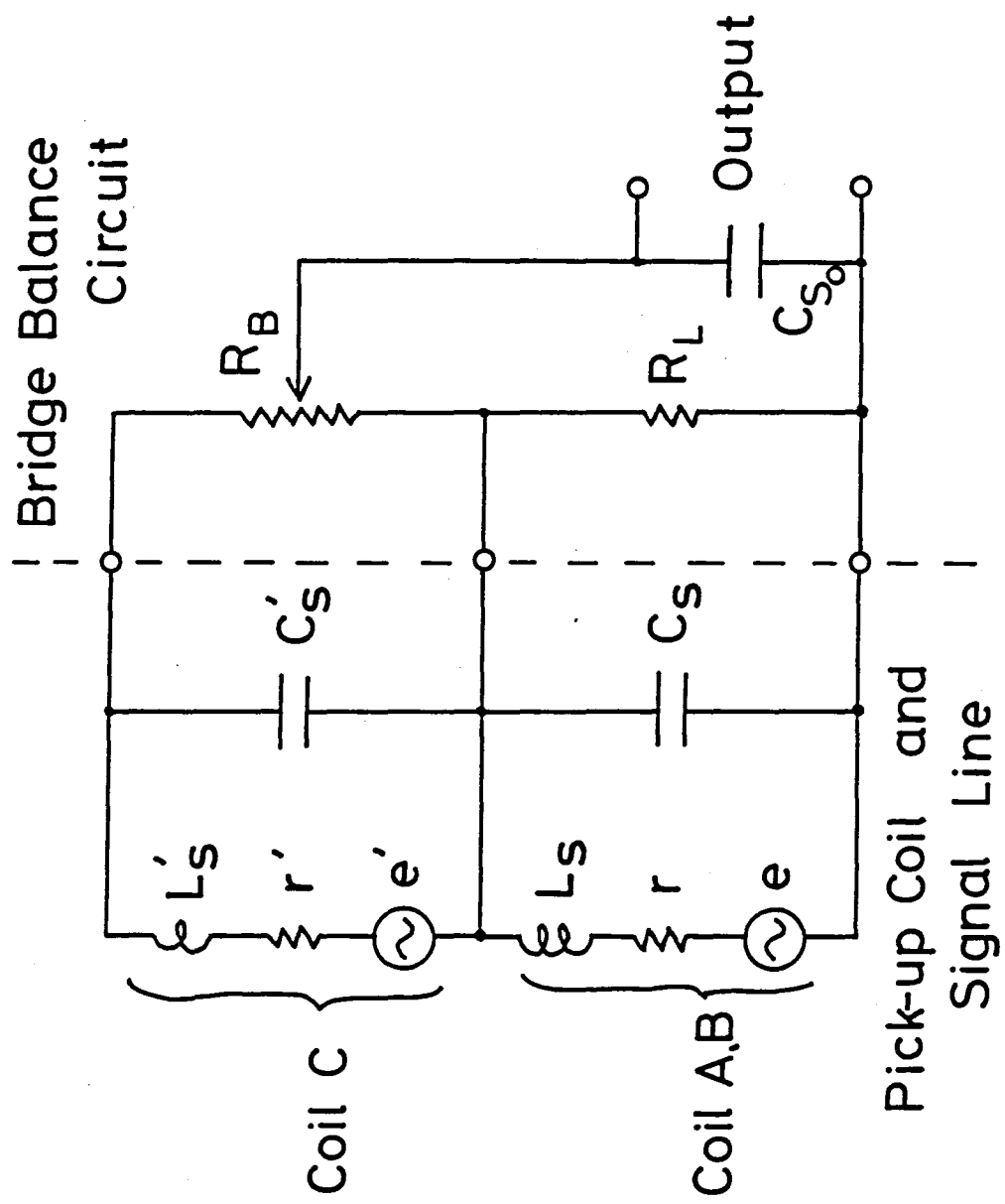


Fig.11 Equivalent circuit for the pick-up coil system.

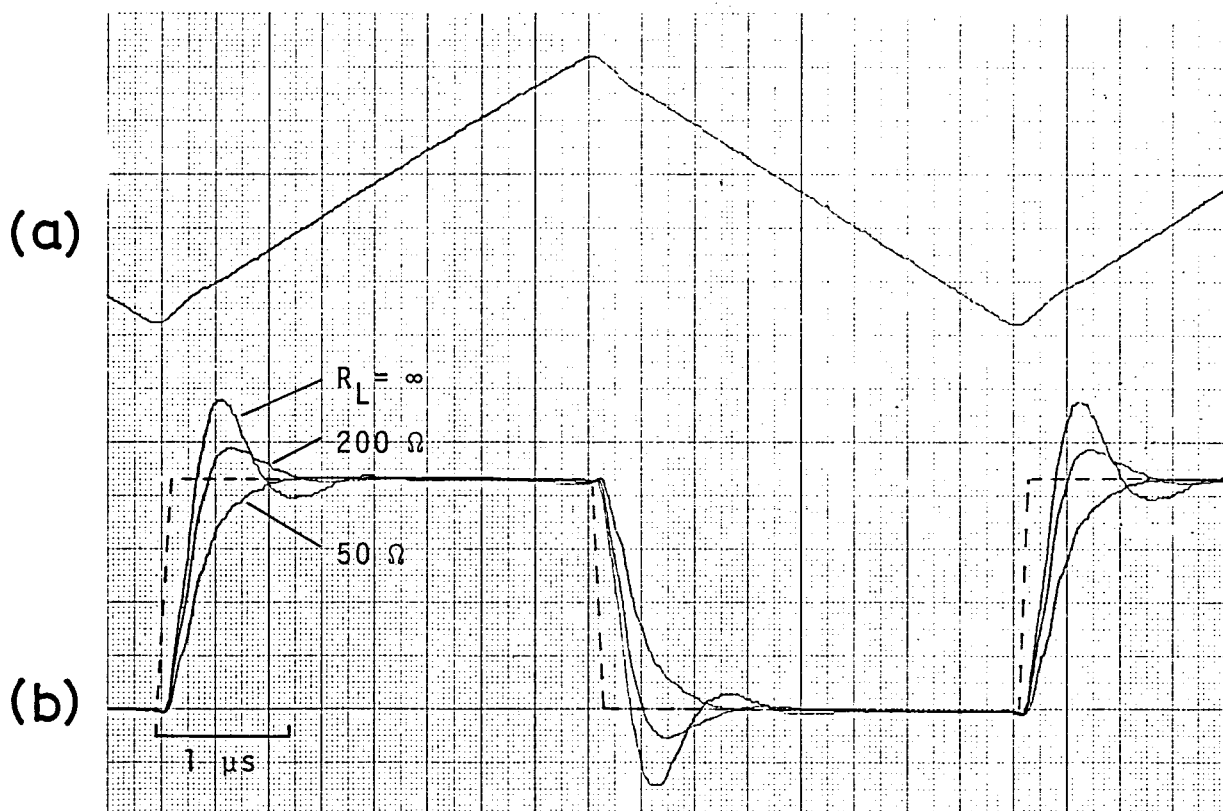
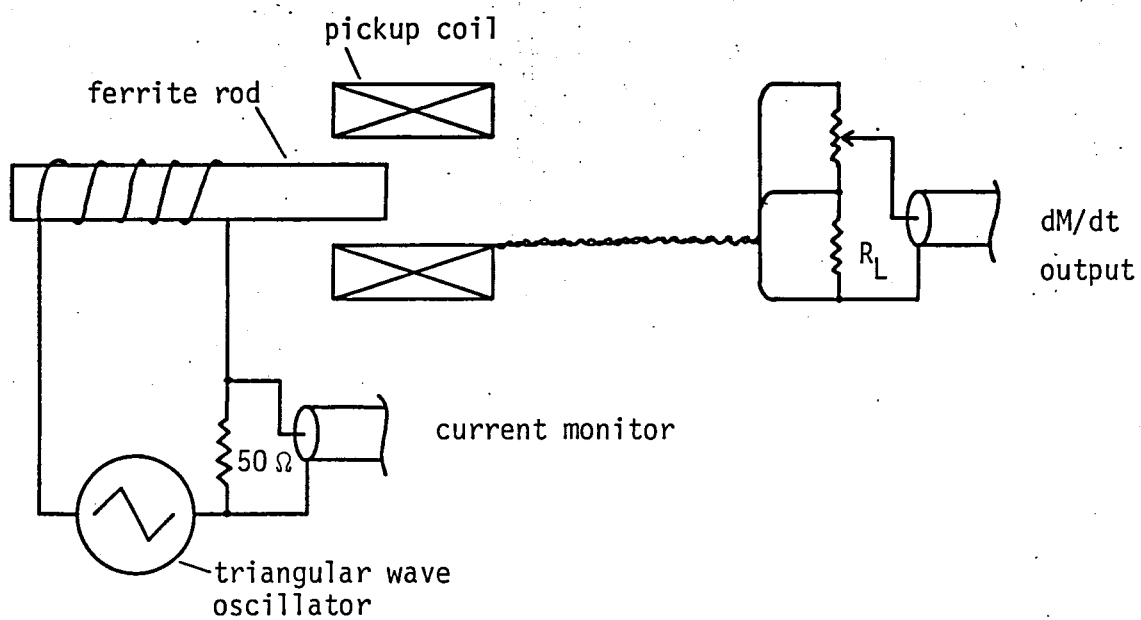


Fig.12. Experimental set up for the pick-up coil response measurement and the results. Curve (a) is the magnetization of the specimen(ferrite rod) and (b) is the corresponding dM/dt output with various load resistor R_L . Dotted line represents the case when there is no signal delay.

through bridge balance circuit and signal transmission cable.

Figure 12(a) shows the current waveform and (b) is the dM/dt output. As the magnetization of the ferrite core follows linearly to the current, the corresponding dM/dt should be like a dotted line in (b). The actual dM/dt signal shows an obvious delay of about $0.2\sim0.4$ μ s depending on R_L . The data were taken with $C_s = C_{s0} = 10^2$ pF, $C_{s0} = 10^3$ pF. Large delay at $R_L = 50\Omega$ is due to the integration effect, while the response at $R_L = \infty$ is found to depend on the resonance frequency which is determined by L_s and C_s, C_{s0} . For the best performance, R_L should be suitably chosen between 50Ω and 200Ω , and the stray capacitances C_s or C_{s0} should be reduced as small as possible. In this respect, the previously used three sheath coaxial cable was found to be inadequate, because it has large C_s (500 pF/m) and the response becomes worse. Use of suitable buffer amplifier will be needed.

Signal delay obtained above is of course not negligible. However, it may not be a principal origin of the hysteresis of 3 kOe seen in the critical field of $\text{CuCl}_2\text{H}_2\text{O}$ (Fig.10B). The field sweep rate at the critical field is 1 kOe/ μ s in that case so that a hysteresis arising from the signal delay will be less than 1 kOe. Another check of the hysteresis is done on a spin-flop field H_{SF} of MnF_2 ($H_{SF} = 92.4$ kOe⁹) at 4.2K). Cylindrical crystal of 7 mm in length and 2.4 mm in diameter, cut along c-axis, was oriented parallel to the field. At H_{SF} , dM/dt shows a sharp spike so that one can precisely read the field value. One example of the results is shown in Fig.13.

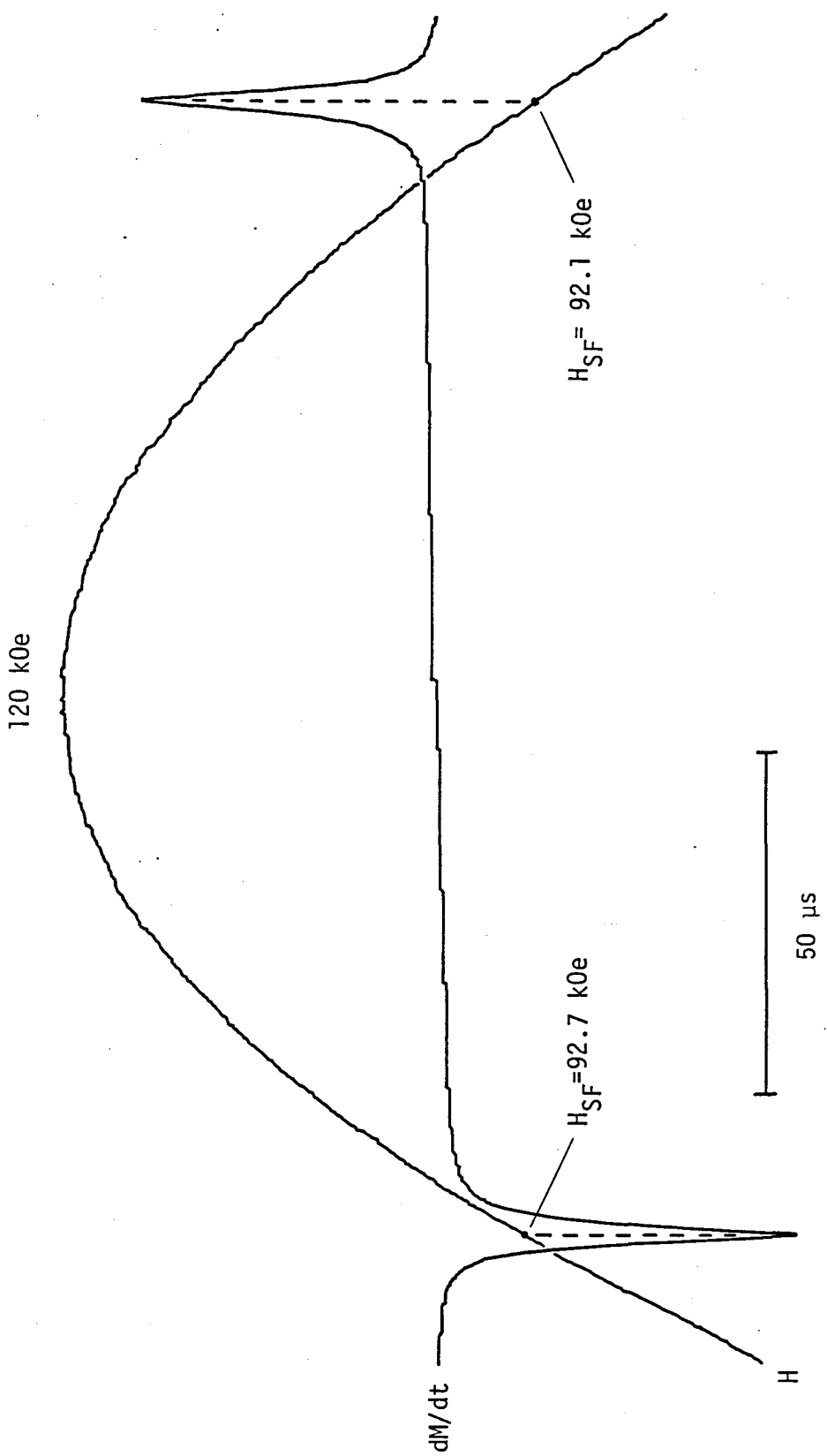


Fig.13 The dM/dt curve of MnF_2 at 4.2 K. The spin-flop transition is marked by sharp spikes in dM/dt . A hysteresis of 0.6 kOe is seen in the spin-flop field H_{SF} .

The result shows a hysteresis of 0.6 kOe in H_{SF} , which is much larger than the value obtained in steady field⁹⁾. Similar measurements are done by changing maximum field and the results are summarized in Fig.14 with those of $\text{CuCl}_2 \cdot 2\text{H}_2\text{O}$. In the figure, the hysteresis value in the critical field is given as a function of field sweep rate. As can be seen, the hysteresis increases systematically with increasing sweep rate for both specimens. Dashed line denotes the value expected from the instrumental signal delay of 0.3 μs . Both results show a larger hysteresis than this value. At present, it is still not clear whether the residual hysteresis is instrumental or not. One may possibly consider the relaxation time of the spin systems, for slightly different results are obtained between MnF_2 and $\text{CuCl}_2 \cdot 2\text{H}_2\text{O}$.

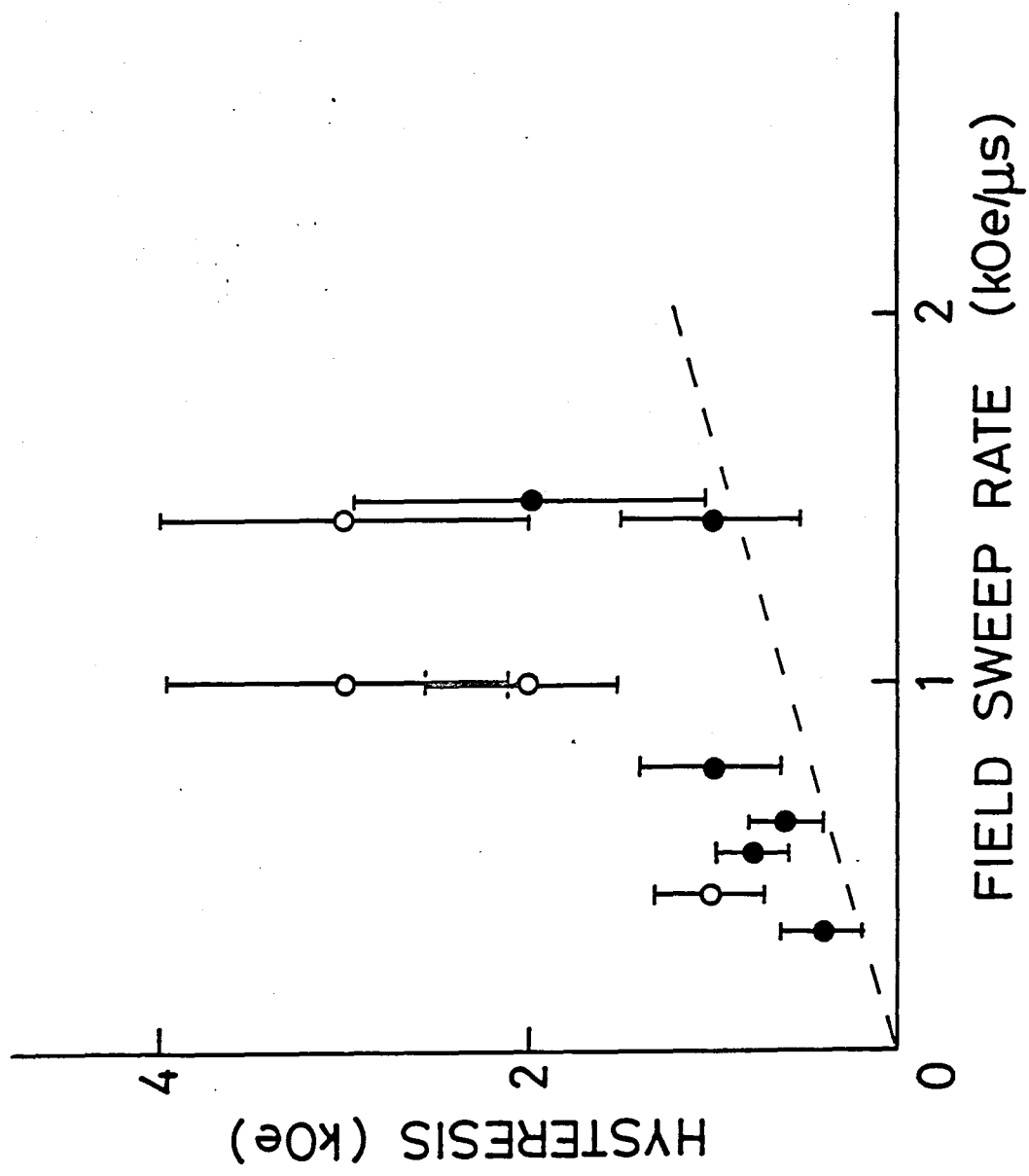


Fig. 14 Hysteresis observed in the spin-flop field of MnF₂ (solid circles) and the antiferromagnetic to paramagnetic critical field of CuCl₂·2H₂O (open circles) as a function of the field sweep rate. Dashed line represents the value expected from a signal delay in the measurement system.

2.4 Improvement of the Sensitivity

Well balanced pick-up coil completely compensates the background flux change that is in phase with and proportional to the applied field. However there still remains an uncompensated signal which makes a background noise V_n . The output dM/dt of pick-up coil is digitally recorded so that a signal from a specimen smaller than $V_n/2^m$, where m is the bit number of the recorder, is undetectable. Sensitivity of the measurement, therefore, is limited by V_n . The sensitivity of the standard pick-up coil is 5×10^{-6} emu/cm³ in a susceptibility measurement.

There are three ways to improve the sensitivity. One is to reduce V_n , the second is to increase m and the third is to make use of some modulation method. To increase m is, however, not easy. Moreover, it does not improve the quality of the data. The modulation method will be effective in some cases. However, considering the field duration time, the modulation frequency should be taken as over than 10^6 Hz so that slow relaxating system can not be measured. Metallic specimen also can not be measured due to skin effect. Therefore, reduction of V_n is attempted.

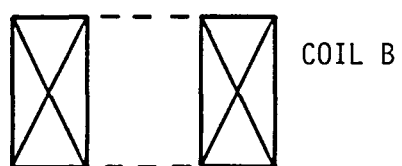
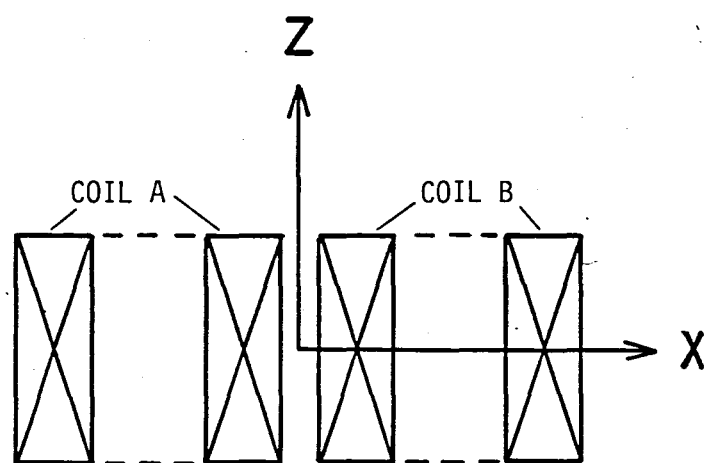
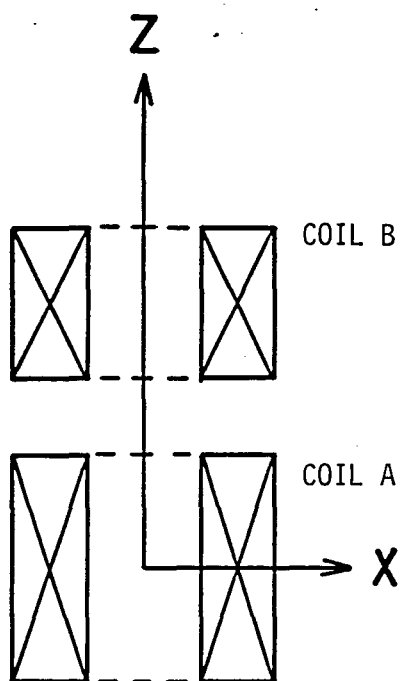
First of all, possible origins of the background noise are considered. As are shown in Fig.11, pick-up coil has self inductance L_s (coil A,B), L_s' (coil C) and internal resistance r (coil A,B), r' (coil C). First, the difference in L_s and L_s' will cause the signal delay in different amount

between the outputs of coil C and coil A,B, and this will produce an out of phase component at the flux compensation. This effect is, however, found to be less dominant. As is shown in Fig.12, the delay time changes with R_L , but no significant change is observed in the background noise waveform. One should also be careful about a magnetoresistance of a coil wire. Change of r or r' causes a shift in a bridge balance point, so that the magnetoresistance of the coil wire will make the flux compensation worse under high field. The magnetoresistance of the coil wire, 2%-tin doped Cu, is measured at 4.2 K and $\Delta\rho/\rho$ is found as $0.5\% \pm 0.2\%$ at 300 kOe. The magnetoresistance is very small and does not contribute to the background dominantly.

A possible and dominant origin of the background noise may come from a field inhomogeneity. Magnetic field $H_o(t)$ around the pick-up coil can be expressed as

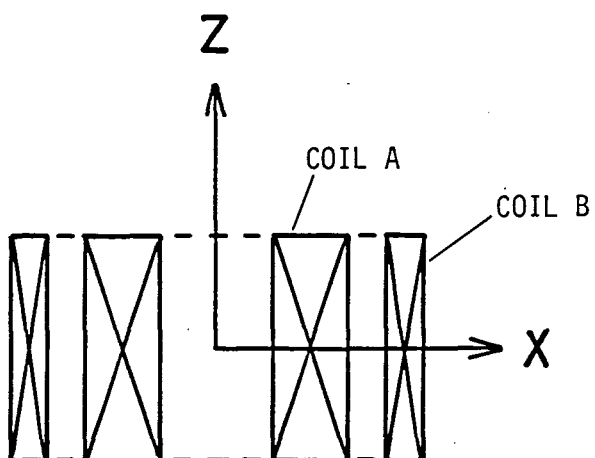
$$H_o(t) = H_u(t) + H_i(t) , \quad (7)$$

where H_u is the uniform field and H_i is the inhomogeneous component that mainly comes from the edge effect of the magnet. A balanced pick-up coil can completely compensate H_u but is usually sensitive to H_i , depending on the coil design. This point is explained in Fig. 15, where three types of pick-up coils tested by our group are shown schematically. Consider type I for example. Coils A and B are first adjusted so as to compensate H_u . If there is a field gradient along z direction in H_i , coils A and B will detect the flux in different amount



Type II

Type I



Type III

Fig.15 Cut view of the three types of pick-up coils.
External field is applied along z-axis.

so that the initial balance between coils A and B is destroyed. In the same sense, type II is sensitive to the field gradient along x direction. The magnitude of H_i is about 0.3 % of that of H_u within the coil dimension, but it is enhanced by the coil turns of A and B that are of the order of 10^2 . Of course, the field inhomogeneity does not lead directly to the background noise. One can always readjust the balance between A and B to compensate H_i so long as H_i is in phase with H_u . However, it is not the case. For example, an elastic distortion of the magnet during the application of strong field will cause change in H_i that is not proportional to $H_u(t)$. Moreover, current distribution of the magnet itself has complex out of phase components. From these reasons, the time rate of change of H_i is not proportional to H_u , so that one can not compensate H_i by readjustment. This may be the origin of the background noise. To reduce the background, one should design a pick-up coil less sensitive to the field inhomogeneity. In this respect, it is natural that type III showed better balance than other types in the previous test²¹⁾. This type is less sensitive to the field gradient along x or z direction as compared with other types. However, the type III, which has been used as a standard pick-up coil, still picks up some higher order inhomogeneity. This is confirmed experimentally. The standard coaxial type pick-up coil whose inner diameter is 3 mm is set at the center of D-1 100(1L)34 magnet and pulsed field of 31 kOe is applied. The pick-up coil is moved along the axial direction of the magnet, z-axis, and the radial

direction of the magnet, x-axis. Change in the flux compensation is then examined. Figure 16 gives the examples of the results. Curve A in the figure is the field trace and B shows the change of the background when the pick-up coil is moved by ± 1 mm along z-direction. Large change in the background is observed. It is found that the net amount of the flux picked up by coils A and B changes linearly with z, although the reason is not clear. On the other hand, the displacement along x direction substantially caused no change in the background. Considering these points, we have designed and tested a new type of pick-up coil, whose cut view is shown in Fig.17. The new type consists of two coaxial type pick-up coil which are called coil 1 and coil 2. Each coil has same structure as is shown in Fig.1 and the inner diameter is 3 mm and the length is 3 mm. Coils 1 and 2 are set in parallel with and close to each other along x direction. Outputs of coils 1 and 2 are connected in series and oppositely. As is clear from the results in Fig.16, coils 1 and 2 will pick up the inhomogeneous field in almost same amount so that subtraction of the signal between these coils will reduce the background. The test is done and the results are shown in Fig.18. Figure 18a shows the change of the background against the displacement along z direction, measured in the same condition with that of Fig.16 B. Note that the scale of Fig.18 (a) is magnified by five times. The new type is found to be much less sensitive to the displacement z. In Fig.18 (b), the background noise of the new type (curve A)

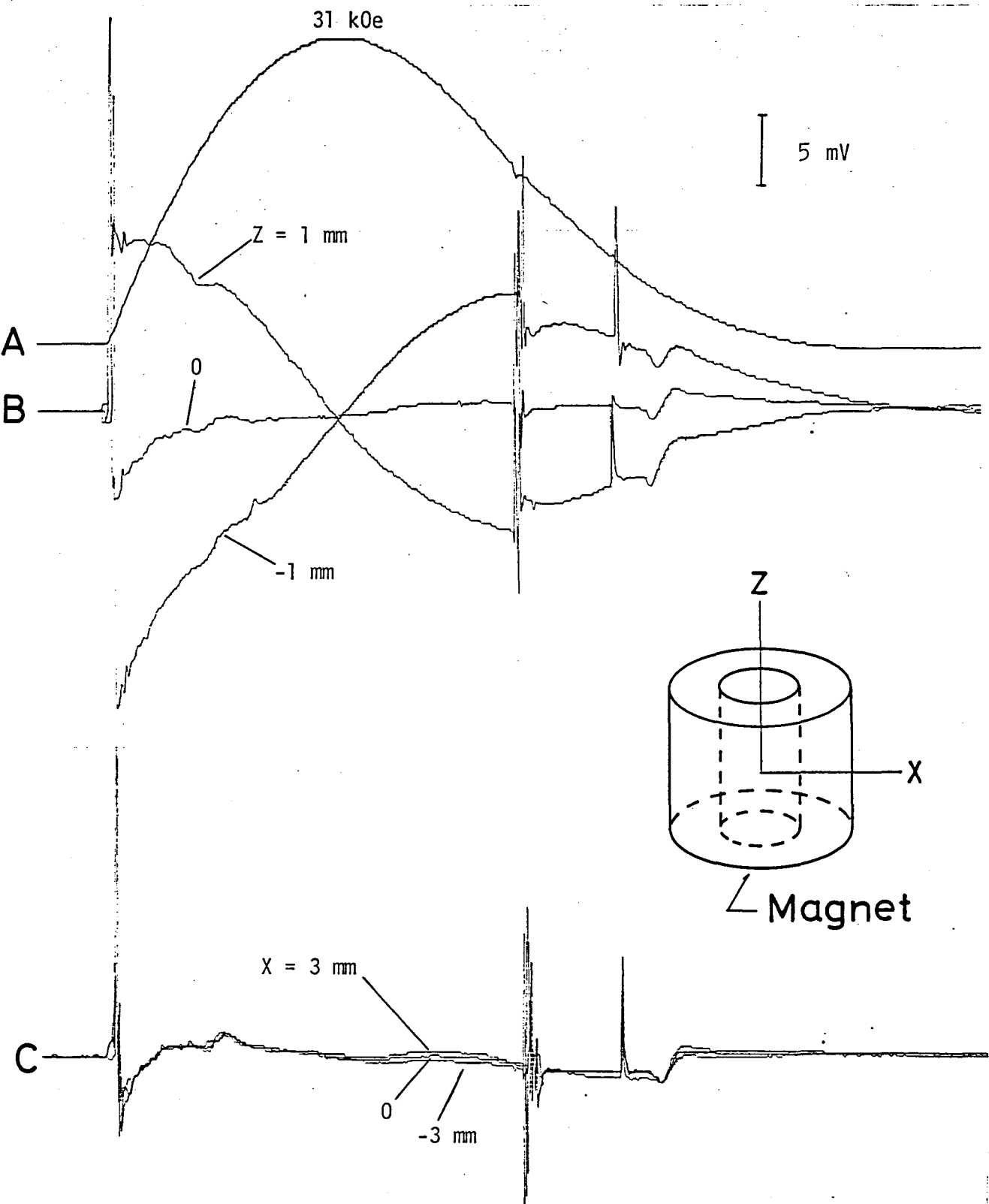


Fig.16 Background noise of a standard pick-up coil at an applied field of 31 k0e shown by curve A. When the coil is displaced along z-direction in the magnet, large change in the background is observed as is shown in B while little change is found at the displacement along x-direction.

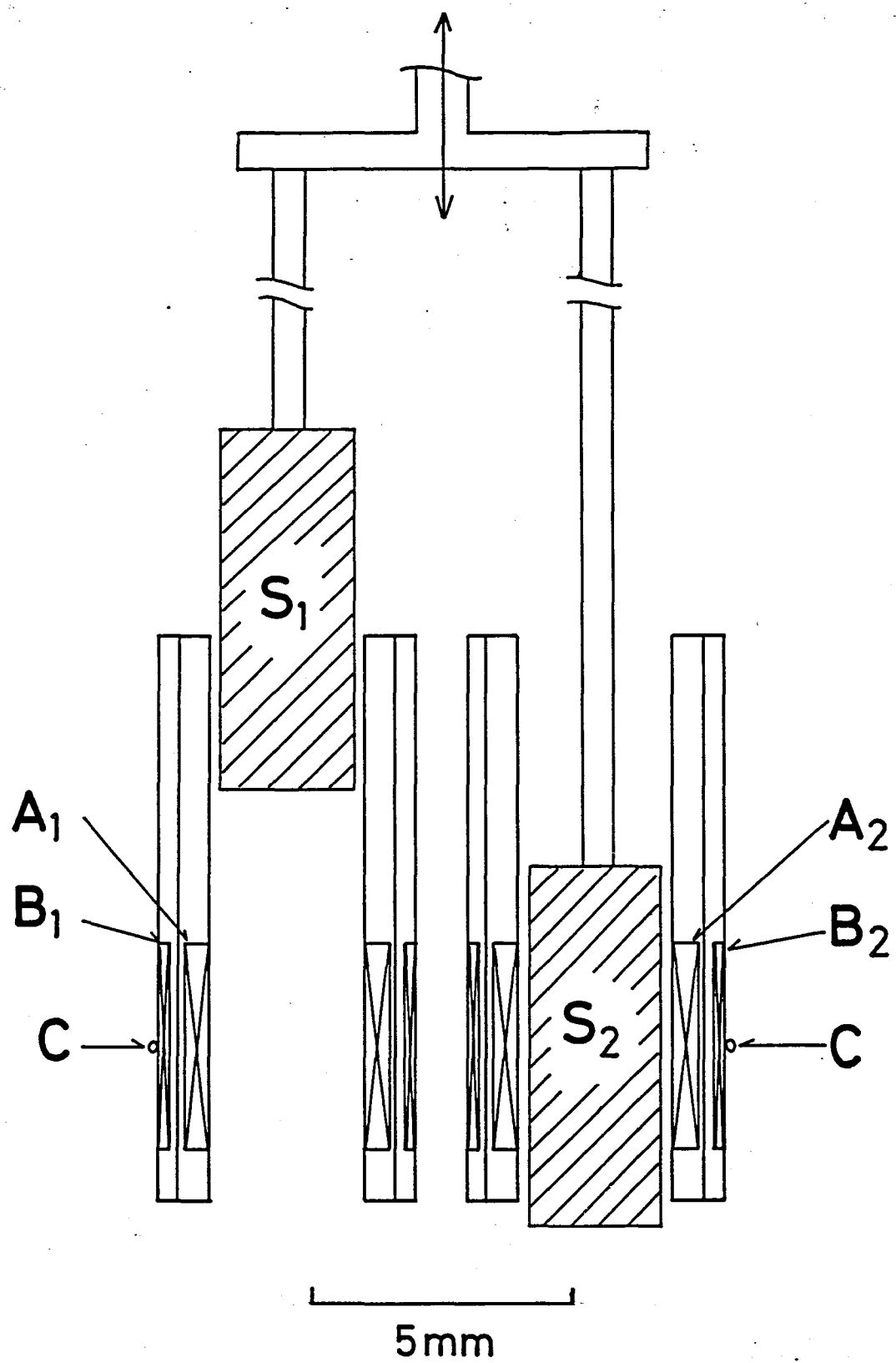


Fig.17 Cut view of the twin-coaxial type pick-up coil.

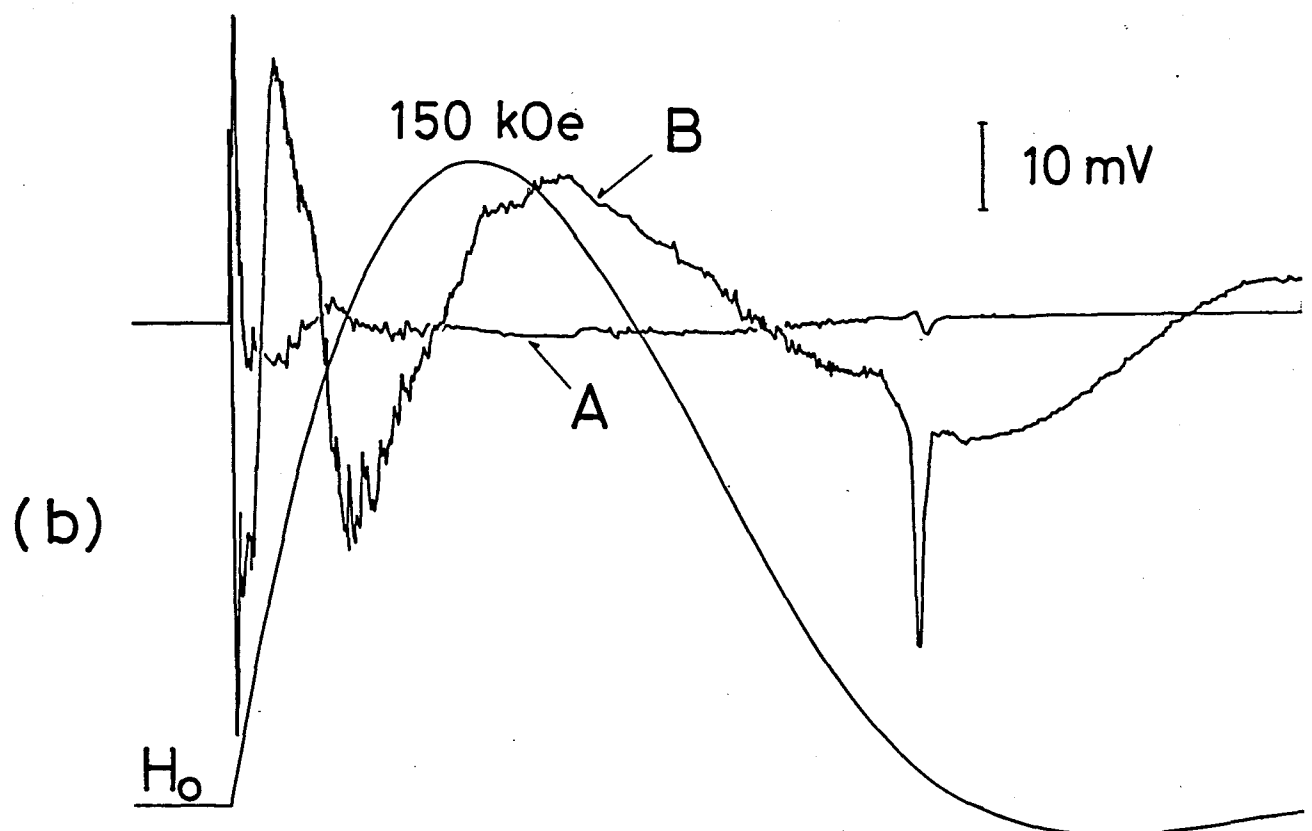
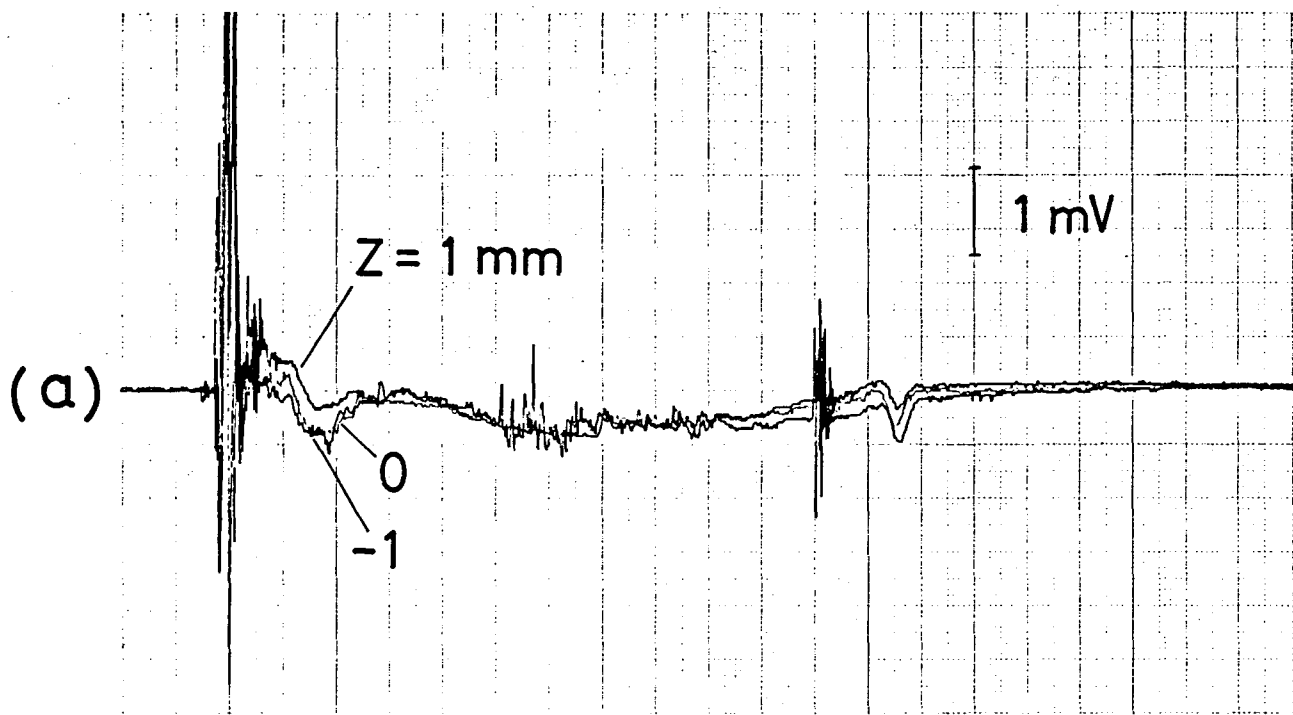


Fig.18 Background noise of the twin-coaxial type pick-up coil. Figure (a) shows the position dependence of the background along the z-direction in the magnet. Figure (b) compares the background of the twin-coaxial type(A) with that of the standard type (B) at the field up to 150 kOe.

and the standard coaxial type (curve B) is compared. The new type has actually improved the flux compensation. The sensitivity is estimated as better than 1×10^{-6} emu/cm³, more than 5 times better than the previous value. In addition to the improved sensitivity, the new type has another advantage. As it is less sensitive to the displacement along any direction, operator is free from an undesirable drift of the background noise caused by thermal expansion of the cryostat. This point is very important in a high sensitivity measurement.

The new type, called twin coaxial pick-up coil, is now used for very high sensitivity measurements. One example is shown on a typical spin-Peierls system $\text{MEM}-(\text{TCNQ})_2$. This material is a one dimensional organic antiferromagnet and exhibits a progressive spin-lattice dimerization to non-magnetic state below 20 K. Under a magnetic field, the system undergoes a transition to some magnetic state around 200 kOe. As the field is fairly large, the character of the phase transition is still not clear and strong field measurement is highly desired^{27~29}. Technically speaking, however, the magnetization of this material is very small ($\chi_{\text{max}} = 3 \times 10^{-6}$ emu/cm³) so that pulsed field measurement was difficult. We have succeeded to observe clear phase transitions. One of the results is shown in Fig.19. Curve A is the dM/dt signal of $\text{MEM}-(\text{TCNQ})_2$ measured by a coaxial type pick-up coil and B is that of twin coaxial type, and C is the field trace. Arrows in the figure indicate the transition points. The transition points are masked by noise and ambiguous in curve A. The quality of the data is improved in great amount in Fig.19 B.

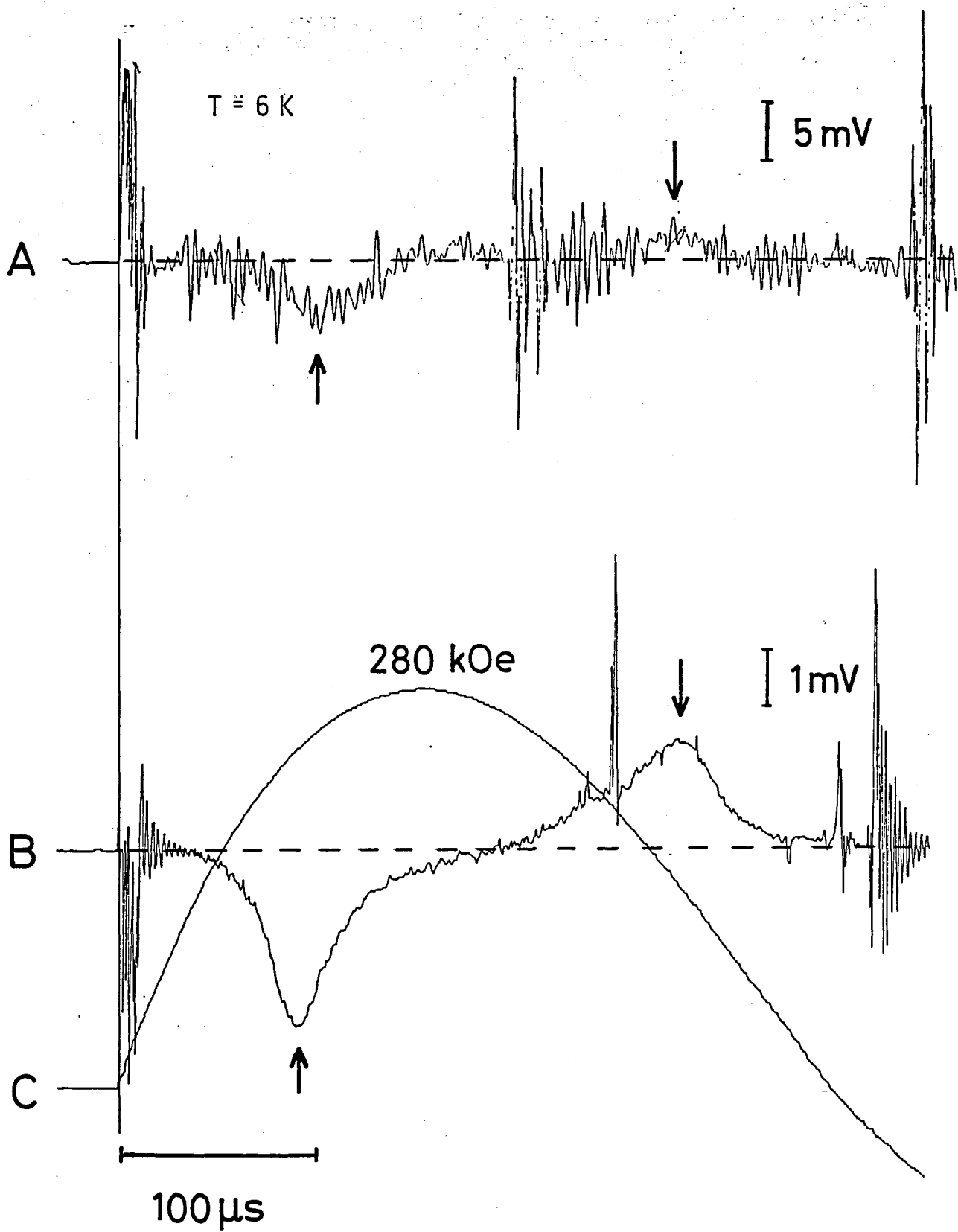


Fig.19 The dM/dt of MEM-(TCNQ)_2 obtained by standard type (curve A) and twin-coaxial type (curve B) pick-up coils. Magnetic transition points are indicated by arrows. Field trace is shown by curve C.

§ 3. MAGNETORESISTANCE MEASUREMENT UNDER PULSED HIGH MAGNETIC FIELD

3.1 Outline of the system

The principle of the magnetoresistance measurement of the present system is same with that of D.C. four-probe method. The block diagram is shown in Fig.20. The different point from a static field measurement is an introduction of the flux compensation. A small coil is wound close to a specimen and a noise voltage induced by the flux change in the four-probe circuit under the transient field is compensated by taking a bridge balance. The output signal voltage is recorded in a digital memory DM-901, IWATSU. The current for the specimen is supplied from a pulsed current source, which covers the field duration time. The magnetic field is monitored by a single loop field pick-up coil and recorded in the digital memory through a field integrator. A simplified circuit of the pulsed current source, and the signal and current transmission is shown in Fig.21. A 50 μ m Cu wire is used for the current and signal leads of the specimen. An ohmic contact between the leads and the specimen is done effectively by the conductive adhesive, DUPONT SILVER #4817. These leads should be twisted well so as not to pick-up the flux of the transient field much. Suppressing the residual magnetic flux by the compensation coil, one can reduce a background noise in the signal output to be less than 10 mV even under the pulsed field of 400 kOe. As the noise intensity is still larger than that of a static field

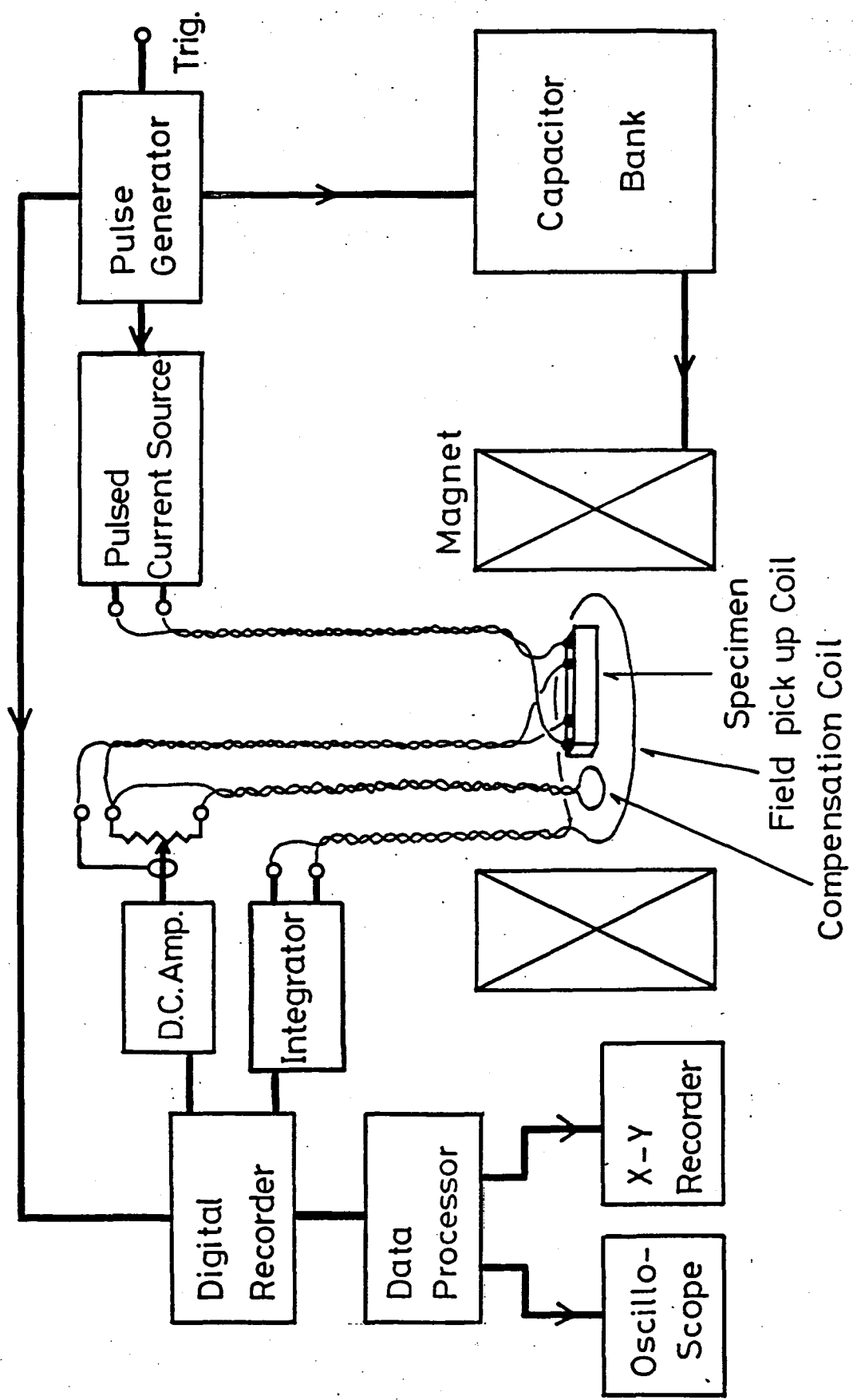


Fig. 20 Block diagram of the magnetoresistance measurement system.

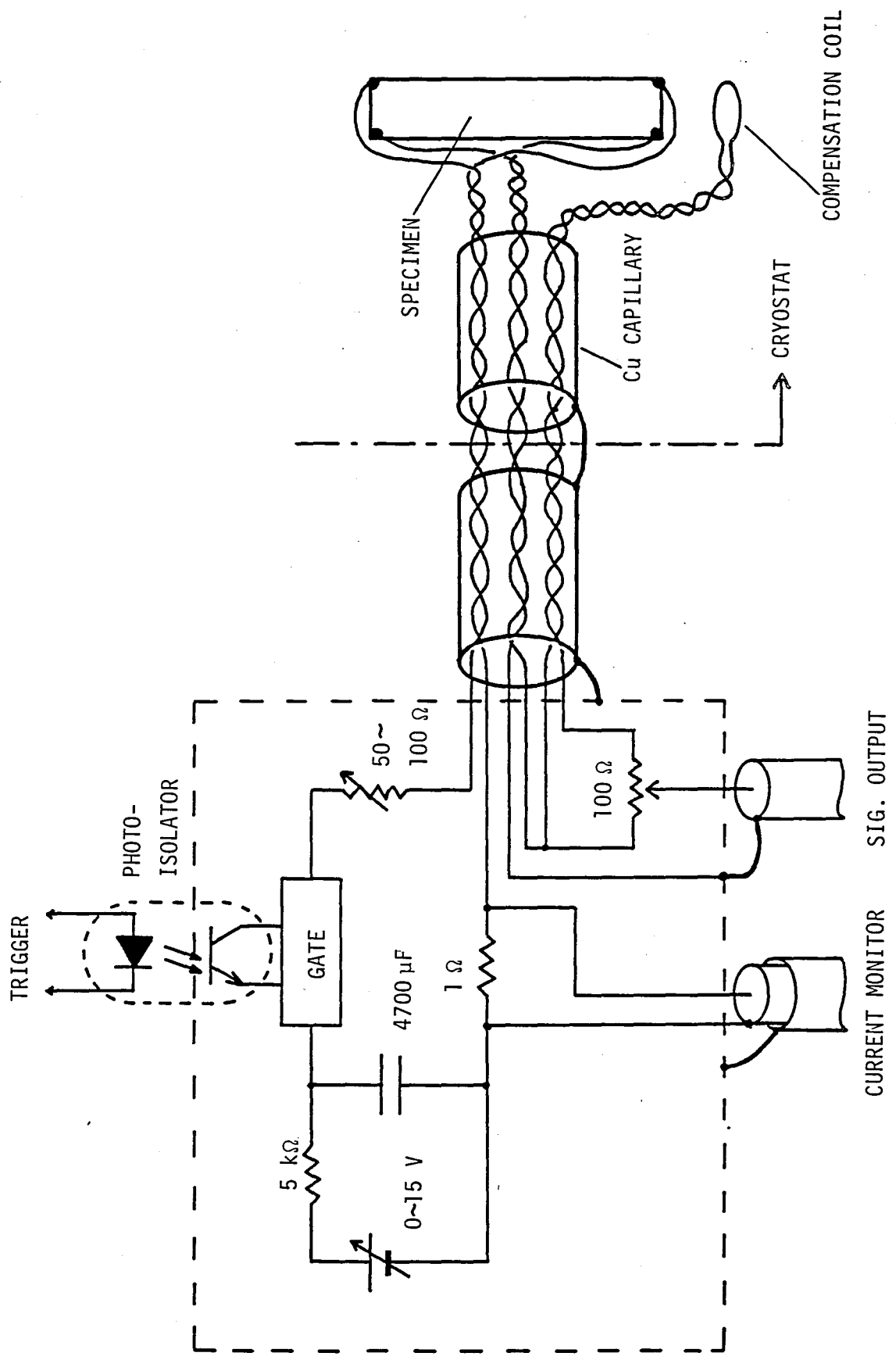


Fig. 21 Current source and signal transmission.

so that larger current is applied to the specimen to improve a quality of the data. The current is gated into a rectangular pulse which covers only the field duration time, so as to avoid excess Joule heating. Photo-isolator is effective for cutting off a noise coming through a triggering line. The current is monitored only at an initial stage of the adjustment of the current value. The monitor cable is taken off during the measurement to avoid an excess noise. The specimen is mounted on a tip of a Bakelite rod for the measurement at liq. He temperature. A sapphire holder is used for the measurement under temperature control, which will be shown in detail later.

Usual measurement is done by applying two shots of pulsed field. The second datum is taken with the specimen current reversed to the first one. A final reduction of the background noise is done at a Data Processor SM-1330, IWATSU, by making a subtraction between these two data. An example of the final result is given in Fig.22. The material is a single crystalline MnSi, a typical itinerant weakly helimagnet. The crystal, whose size is $0.05 \times 0.1 \times 7 \text{ mm}^3$, is set in the D-2 1L magnet and the current of 150 mA is applied perpendicular to the field. Figure 22 shows the recorder trace of the applied field H_o and the background-reduced output signal V_R that is proportional to the resistivity change of the specimen. High frequency noises indicated by A and B come from switchings of the D-2 bank system. A clear reduction in the resistivity of $38 \pm 1 \%$ is observed at 220 kOe due to the suppression of the spin fluctuation by the strong field. Further details are given in ref.32).

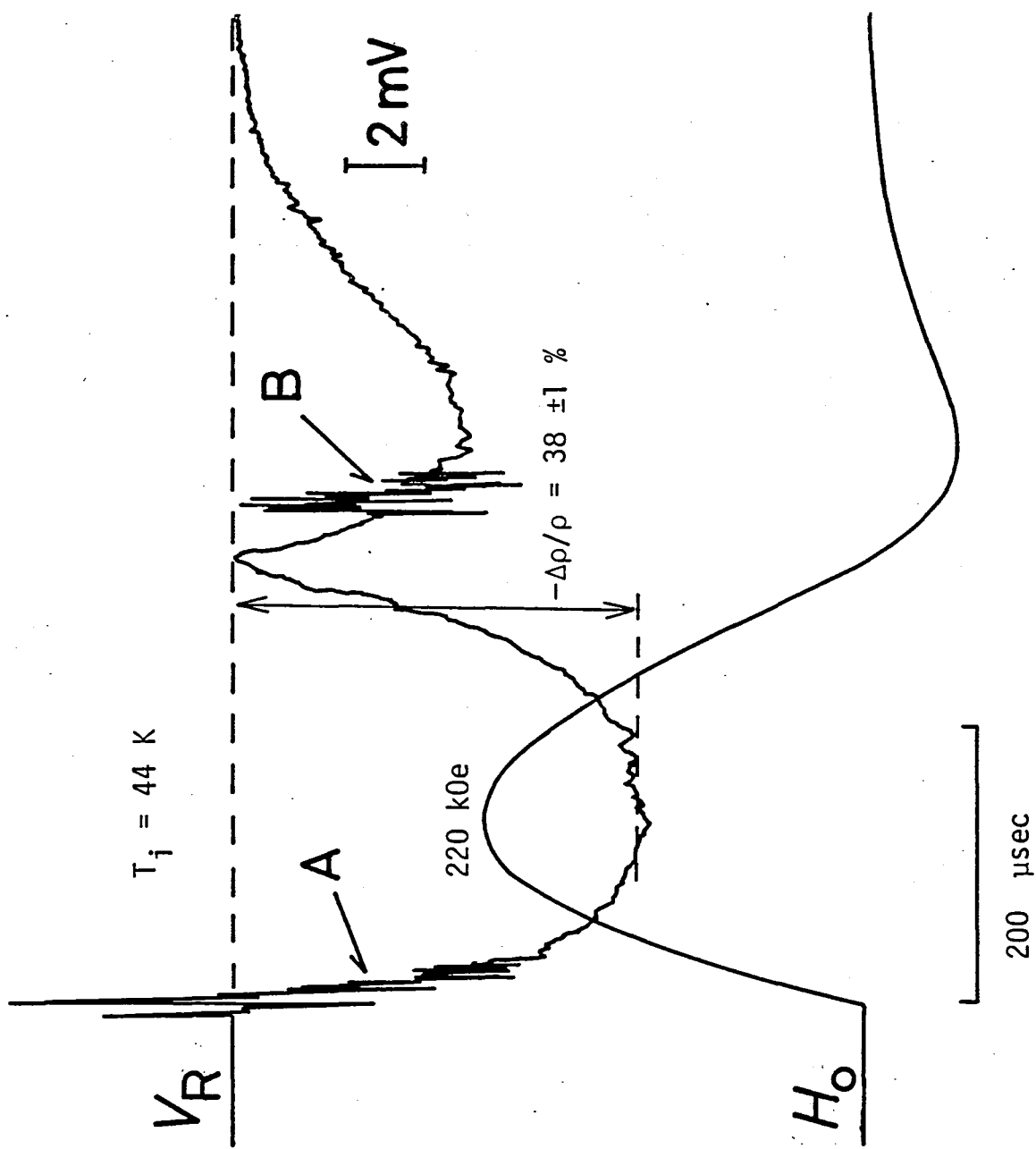


Fig. 22 Magnetoresistance of MnSi measured at 44 K. The signal V_R corresponds to the resistivity change, and H_0 is the field trace.

3.2 Joule Heating of the Specimen due to the Eddy Current

One of the serious problems in the magnetoresistance measurement under the pulsed field is the effects of eddy current that is induced in a specimen. It will cause a phase delay in the signal and, what is worse, heat up the specimen during the measurement. One can avoid these effects by reducing the size D of the specimen much less than the skin depth δ , i.e., $D \ll \delta$. The practical condition for D is given here.

We consider Joule heat of a conductive long cylinder placed under sinusoidally oscillating field $H_0(t) = H_0 e^{-i\omega t}$, applied along the cylindrical axis. Eddy current then flows around the cylindrical axis. Under quasi-stational condition, the eddy current density $j(r, t)$ at radius r is easily obtained as

$$j(r, t) = \frac{H_0 \beta}{J_0(\beta D/2)} J_1(\beta r) e^{-i\omega t}, \quad (8)$$

where $\beta = \sqrt{i\omega\mu/\rho}$, ρ is the resistivity and μ is the permeability of the material, D is the diameter of the cylinder, and J_0 and J_1 are the Bessel functions of order 0 and 1, respectively.

Time averaged Joule heat P of unit length is given by

$$P = 2\pi\rho \int_0^{D/2} \frac{1}{2} j^*(r, t) j(r, t) r dr. \quad (9)$$

Usual measurements are done within the field rise time, i.e., a quarter period of the oscillation. Therefore, the Joule heat Q during the measurement is given by $Q = \pi P / 2\omega$.

Now, we are concerned with the case $D < \delta$, $\delta = \sqrt{2\rho/\mu\omega}$, or

otherwise, the external field can not penetrate into the cylinder. In this case, $|\beta D| < 1$ so that one can expand J_0 and J_1 in ascending series. Taking only the leading terms for the first approximation, Q is written in MKS unit as

$$Q = (\pi \mu H_0)^2 \omega D^4 / 512 \rho \quad (10)$$

To estimate temperature increase ΔT of the specimen at low temperature region, we assume the molar heat capacity in the form

$$C = \gamma T + A T^3, \quad (11)$$

where γ is the electronic part and A is the lattice part. The temperature increase ΔT with the initial temperature T_i is then obtained by the relation

$$Q = \frac{\pi D^2 \rho_s}{4 M_s} \int_{T_i}^{T_i + \Delta T} (\gamma T + A T^3) dT, \quad (12)$$

where ρ_s is the specific gravity and M_s is the molar weight of the specimen. Change in the resistivity ρ is neglected.

Some results for ΔT are given in Fig. 23 as a function of field. The radius D is taken as $50 \mu\text{m}$, which may be the lower limit of easily obtainable dimension for most cases. Angular frequency ω is assumed as $10^4/\text{sec}$, which is near the characteristic frequency of D-1 and D-2 pulse-magnet. Other parameters are tentatively taken as follows: $\mu = 4\pi \times 10^{-7} \text{ Hm}^{-1}$, $\gamma = 1 \text{ mJ/mole K}^2$, $A = 0.049 \text{ mJ/mole K}^4$, $\rho_s = 9 \times 10^3 \text{ kg/m}^3$, $M_s = 64 \times 10^{-3} \text{ kg}$.

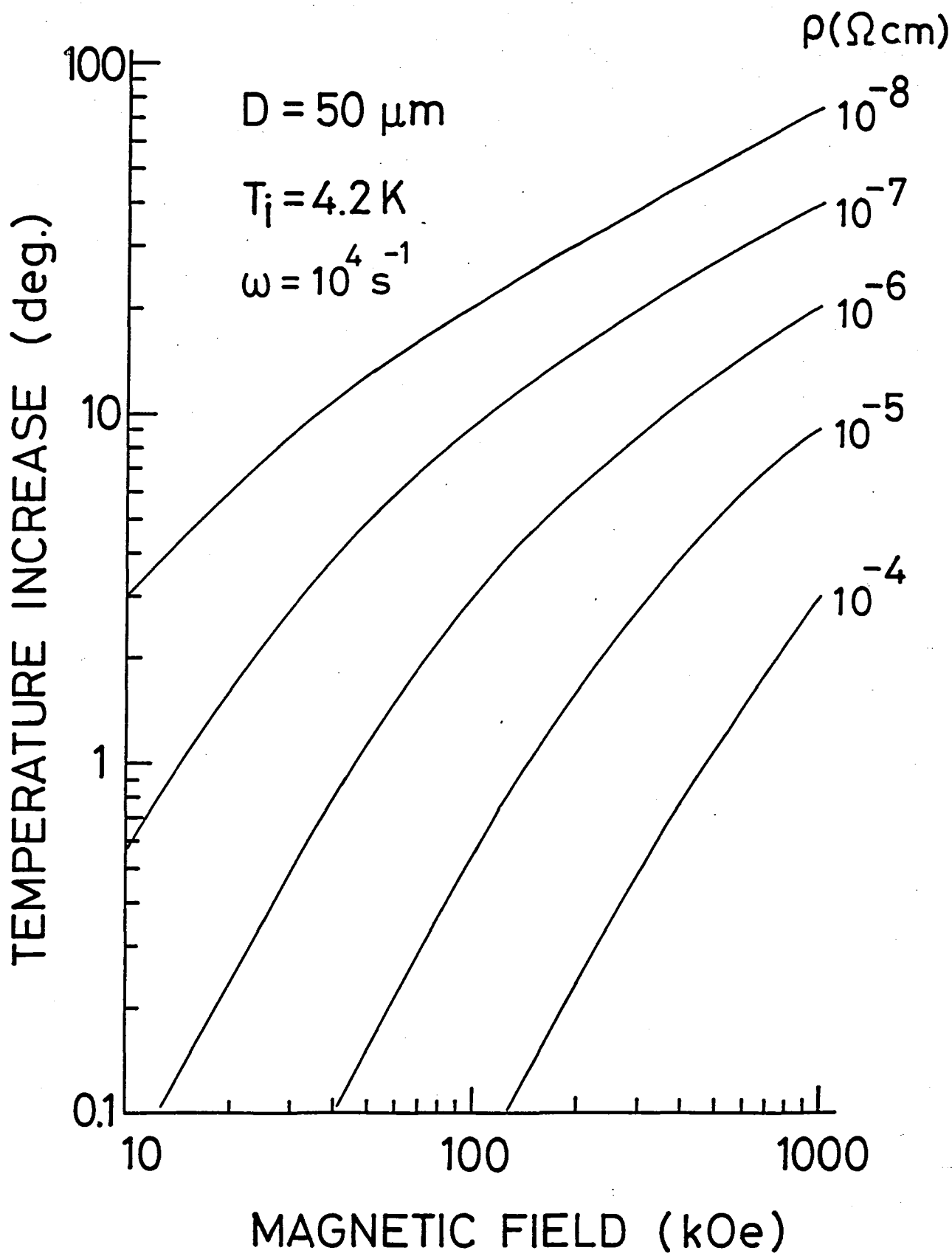


Fig.23 Temperature increase of a conductive cylinder (diameter $D=50 \mu\text{m}$) with various resistivity ρ , within a rise time of a pulsed field whose frequency is $\omega=10^4/\text{s}$.

These values are taken close to those of 3d-transition metals. As is clear from the figure, the temperature increase of the specimen becomes quite serious when the resistivity is smaller than 10^{-5} Ω cm. Figure 24 gives the upper limit of D under various allowable temperature increase ΔT , as a function of field. The initial temperature is taken as 4.2 K and the same parameters with Fig.23 are used. For example, if one wants to measure a material with $\rho=10^{-5}$ Ω cm up to 400 kOe within a temperature increase of 2 K, the diameter should be reduced to less than 30 μ m.

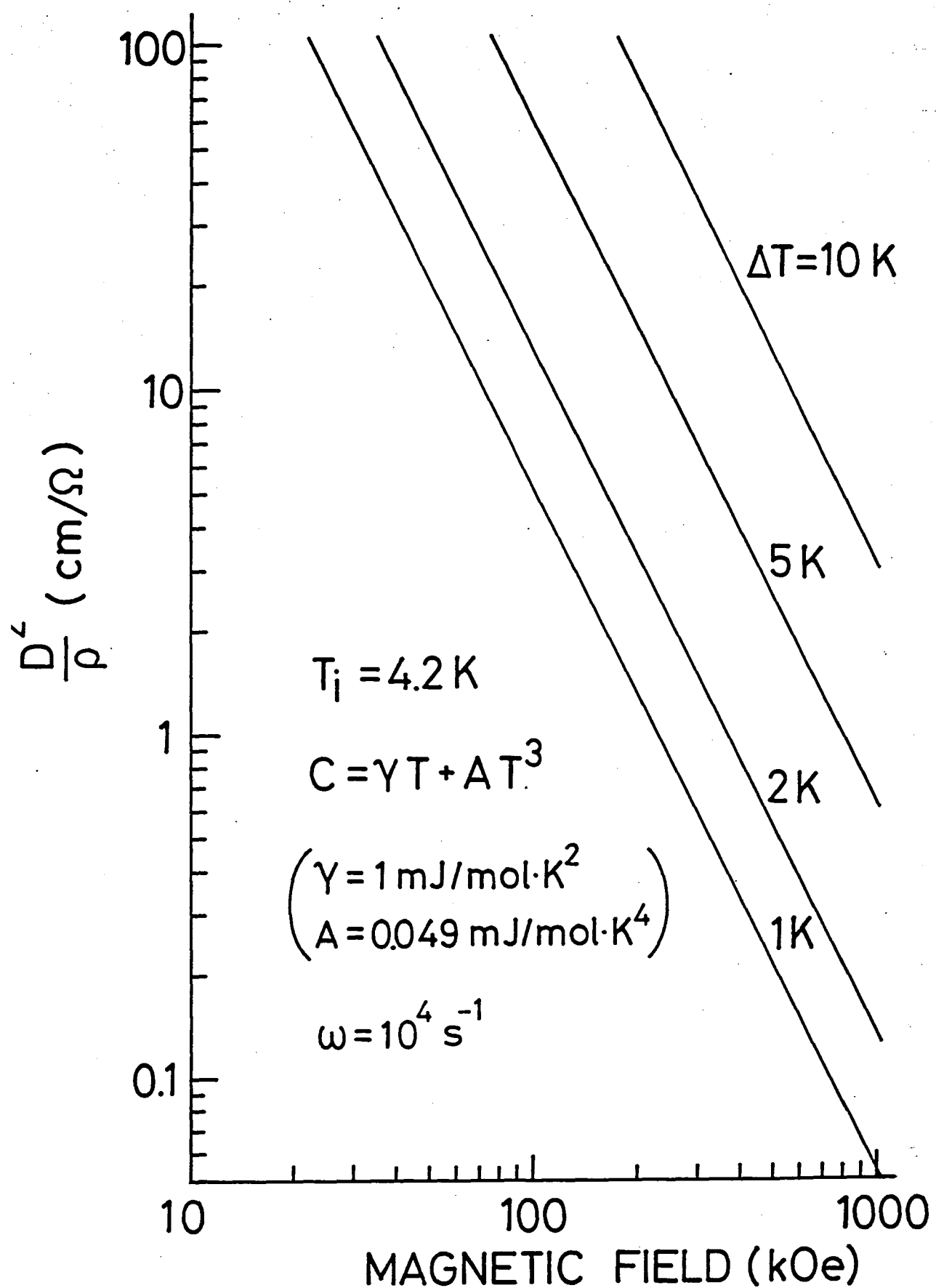


Fig. 24 Condition for D and ρ under various allowable temperature increase ΔT .

§4. TEMPERATURE CONTROL TECHNIQUES UNDER PULSED HIGH MAGNETIC FIELD

4.1 Outline of the System

The precise temperature control of a specimen is an indispensable technique, when one wants to know temperature dependent phenomena such as magnetic phase transitions of antiferromagnets or H_{c2} -T relations of superconducting materials. The temperature control in the range 1.3 K to 4.2 K and 64 K to 77 K can be easily done by regulating the vapor pressure of liquid helium or nitrogen bath, respectively. However, to cover the range 4.2 K to 64 K or above 77 K under the pulsed high magnetic field is not so easy. The most simple method is to do measurement while a specimen is warming up slowly after the liquid helium or nitrogen has run out⁹⁾. This method is not efficient because only one or two shots are available at one run. Moreover, subtraction of a background noise in the signal at same temperature is impossible so that it is not suitable for the precise magnetization and magnetoresistance measurement. If one wishes to do measurements under more precise temperature control, one must introduce heater and a thermal insulation around specimen, as well as some cooling method. To contain the whole assembly, a magnet needs large bore and consequently, large energy source.

For these purpose, large bore one layer magnet 150(1L)60 has been designed in our laboratory²¹⁾. This magnet can produce fields up to 400 kOe repeatedly within an inner diameter

of 6 cm, with D-2 1.25 MJ energy source. The magnet permits insertion of a 2.6 cm i.d. glass Dewar as is shown in Fig.25. The Dewar is specially designed to contain liquid helium of about 120 cc below a specimen for cooling it, and has enough space for the temperature control assembly. Usual silver coating is done on the Dewar, with slits of 10 mm on the sides. The coating is found to have no problem on the field penetration or flux compensation of the pick-up coil. The Dewar is supported mechanically free from the magnet.

The method of temperature regulation is schematically shown in Fig.26. The automatic temperature control system developed in our laboratory is used. Two heaters A and B are set. Heater A is used for heating the specimen, while B is immersed in liquid helium and used for cooling it by evaporating cold helium gas. The temperature of the specimen is monitored by a thermo-couple AuCo-Cu or AuFe-Ag, which is connected to an amplifier through a microvolt generator. The difference between the thermo-electric voltage and the reference voltage produced by the microvolt generator is amplified and negatively fed back to the heaters through a heater current controller. The heater current controller supplies current of maximum 500 mA to the heaters A or B, according to the magnitude and sign of the difference voltage. This system is very compact but can regulate the temperature within ± 0.1 K at the temperature region 4.2 K to 200 K. Liquid helium lasts for about 6~8 hours at one run.

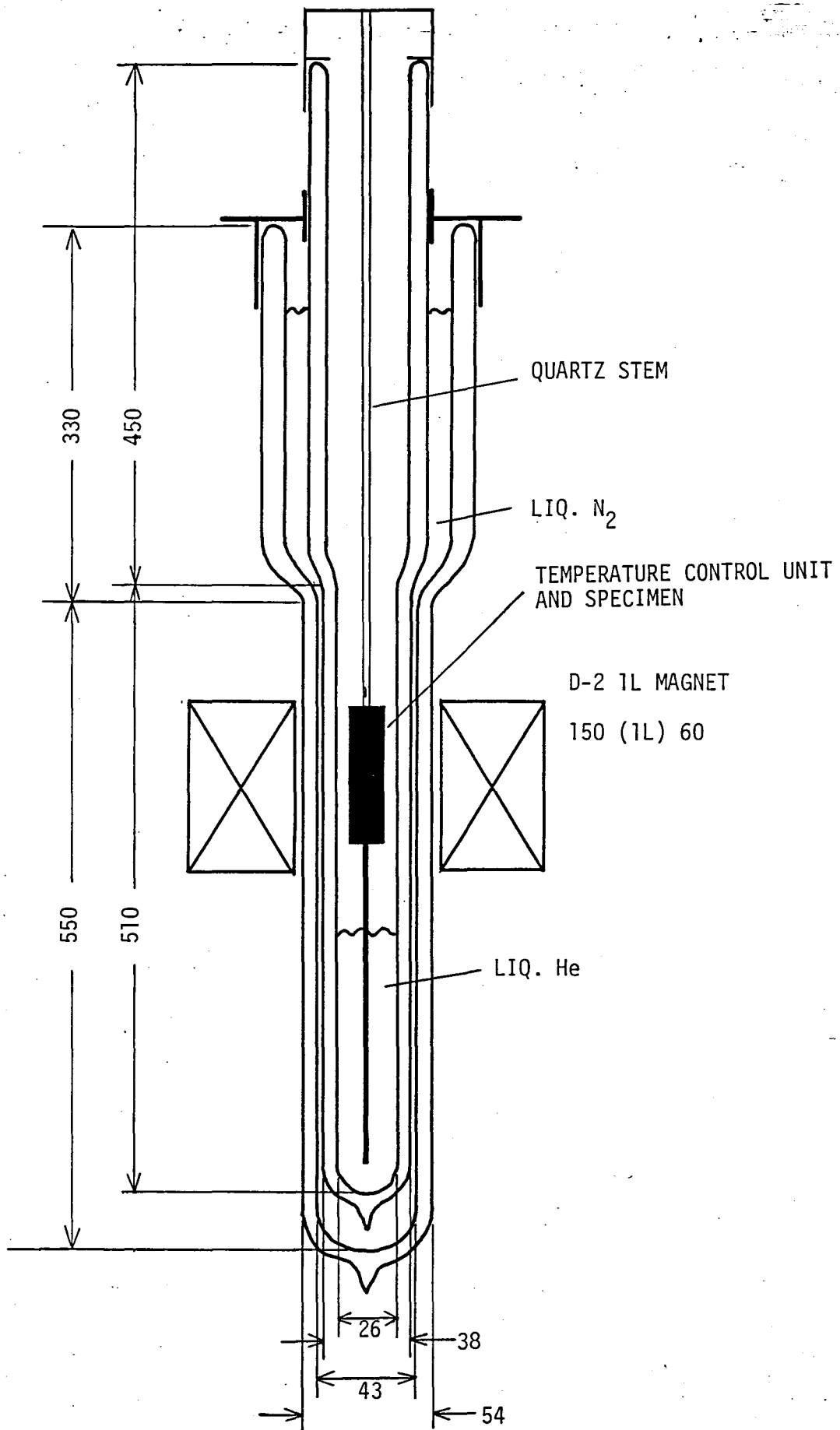


Fig.25 Cut view of the Dewar for the temperature controlled measurement.

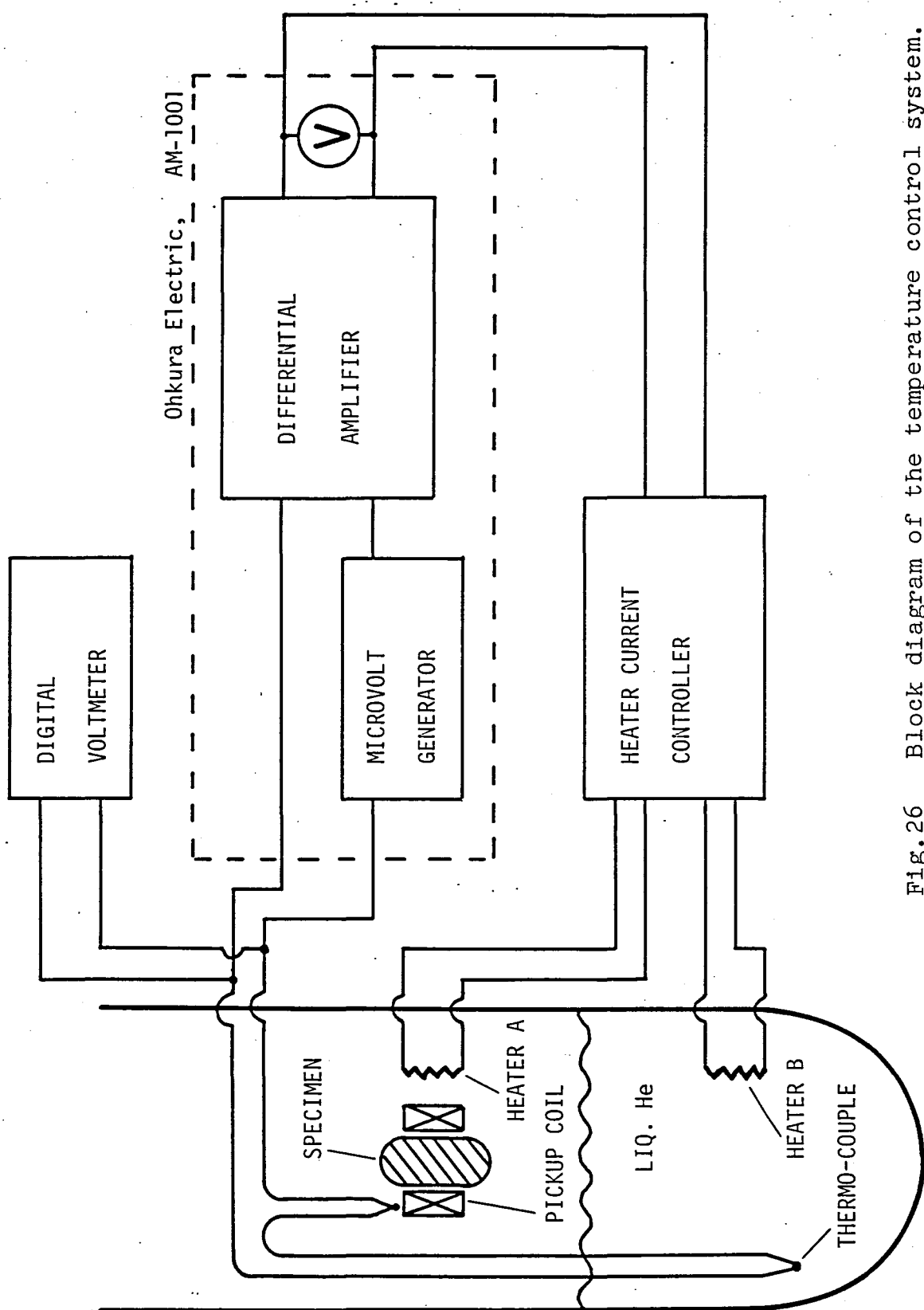


Fig. 26 Block diagram of the temperature control system.

4.2 Temperature Control Units

One technical difficulty encountered when one applies this system under pulsed field is the inability of using bulk metallic materials. For example, bulk copper can not be used as a heat conductor because of skin effect or Joule heat. In principle, only non-magnetic insulating materials are available for the apparatus and consequently, one should be careful for the temperature gradient around the specimen. The practical design of the temperature control units for magnetization and magneto-resistance measurements are shown in Fig.27. The specimen is contained in a thermal insulation cell made of Bakelite of 1.5 mm thick, which is effective to change the temperature gradually. Heater-A is wound non-inductively around the cell with several turns of manganese wire and the resistance is 10Ω . Inside of the cell is filled with atmospheric helium gas.

In the magnetoresistance measurement, a single crystal sapphire disc of 3 mm thick and 2 cm in diameter is used for a specimen stage. The sapphire has good thermal conductivity which is comparable with that of metallic copper below 100 K, so that it is very useful insulating material. Figure 28 compares the thermal conductivity of the sapphire with some materials. The specimen is mounted on the stage with Apiezon N grease and the thermo-couple is attached close to it with GE-7031 varnish. By this arrangement, uniformity of temperature around the specimen and the thermometer can be obtained satisfactorily.

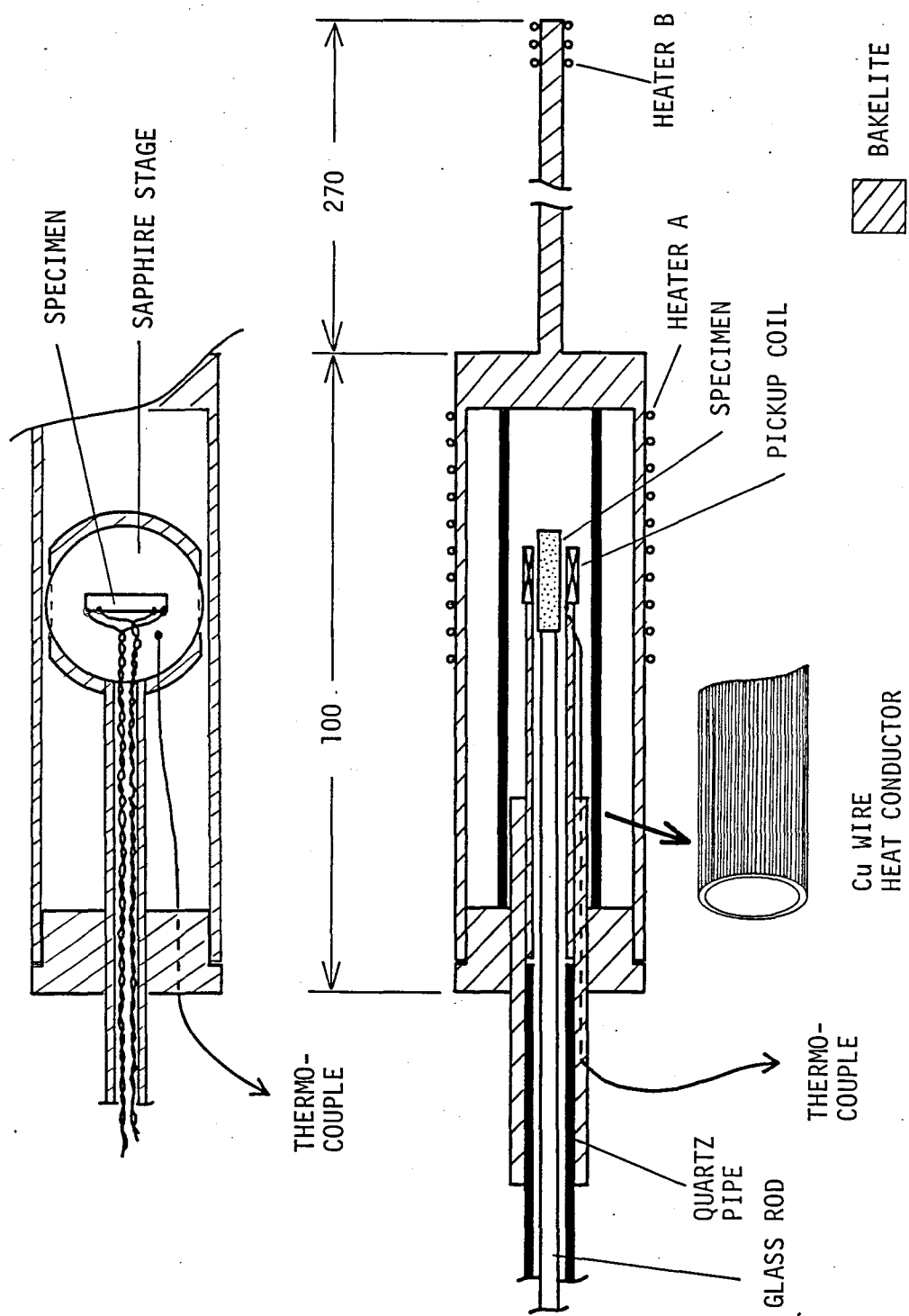


Fig. 27 Cut view of the temperature control units for magnetoresistance (upper) and magnetization(lower) measurement.

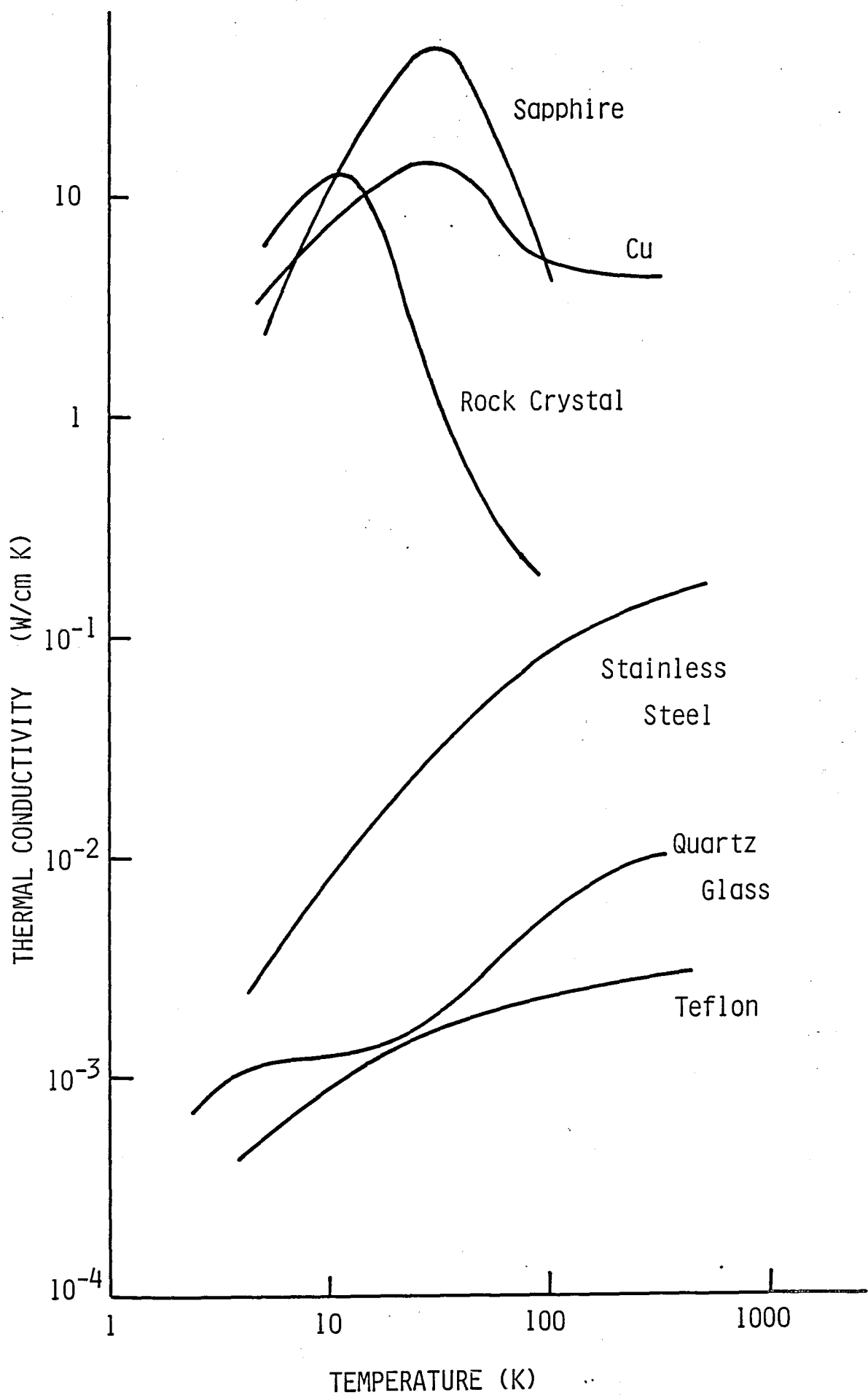


Fig.28 Thermal conductivity of some materials.

In the magnetization measurement, one needs datum without a specimen in a pick-up coil to subtract the effect of the background noise, so that the specimen is frequently moved along the pick-up coil for the insertion and extraction during the experiment. Consequently, the temperature gradient along the pick-up coil is undesirable and should be reduced as small as possible. For this purpose, a copper wire heat conductor is set just around the pick-up coil as is shown in Fig.27. The heat conductor is made of about 1200 urethane-coated $50\mu\text{m}$ Cu-wires which are aligned along a thin Bakelite pipe and fixed with GE-7031 varnish on it. The thermometer is set close to the specimen through a hole made in the bobbin of the pick-up coil. The temperature uniformity is examined and an example of the results is given in Fig.29. A thermo-couple mounted on the tip of a glass rod is moved in the pick-up coil along the axis, and the temperature difference with respect to the center of the coil is plotted against the position. The data are taken at 25 K, ten minutes after decreasing the temperature from 50 K. Black points in Fig.29 are the result with the heat conductor, and the white ones are the result without it. Cut view of the pick-up coil and the heat conductor are also shown, and the position of the specimen is indicated for comparison. As is clear from the figure, the Cu-wire heat conductor is effective for improving the temperature uniformity along the pick-up coil. The temperature gradient is less than 0.1 K within the length of the specimen(~ 15 mm), and less than 0.5 K

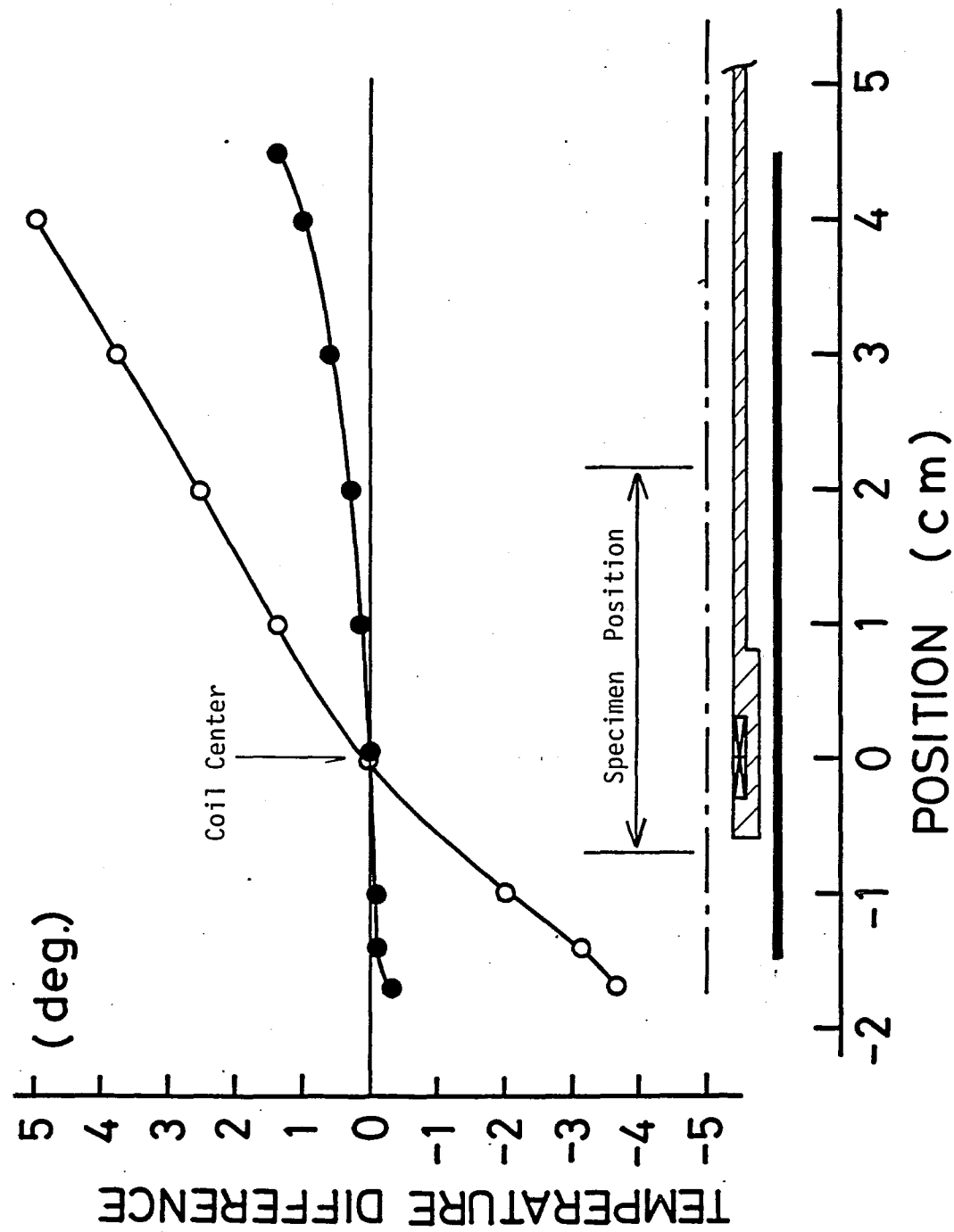


Fig. 29 Temperature distribution along the pick-up coil shown in Fig. 27. Black circles are measured at $T=25$ K with the Cu-wire heat conductor, and open circles are the results without it.

within the stroke(20~30 mm). The external field is applied parallel to the wire of the heat conductor so that the eddy current effects are smallest. No change is observed in the flux compensation of the pick-up coil. However, the temperature increases by several degrees after a shot of 300 kOe. Although the heat up of the Cu-wire does not affect the temperature of the specimen during the shot, it should be better to use sapphire, instead of Cu-wire. As the pick-up coil is very sensitive to the movement along its axial direction, the whole assembly is suspended by a quartz pipe which has very small coefficient of thermal expansion.

Examples of the temperature controlled magnetization measurements are shown in Fig.30. The material examined is a weakly itinerant helimagnet MnSi³²⁾ with $T_N=30$ K. The specimen is powdered within the particle radius of 40 μ m and cast into a cylinder of 3mm D x 15 mm by Araldite. Solid lines in the figure are the pulsed field results with the present apparatus, and dotted lines denote the results of steady field measurement by Bloch et al⁴⁵⁾, showing good agreement between the two.

One remark is made on the resistance of the pick-up coil wire. The resistivity of the wire material, 2% tin-doped Cu, is shown in Fig.31 as a function of temperature, where that of pure Cu is also shown for comparison. Although the temperature dependence of the material is weaker than Cu, it is not negligible in the temperature dependent experiments. For

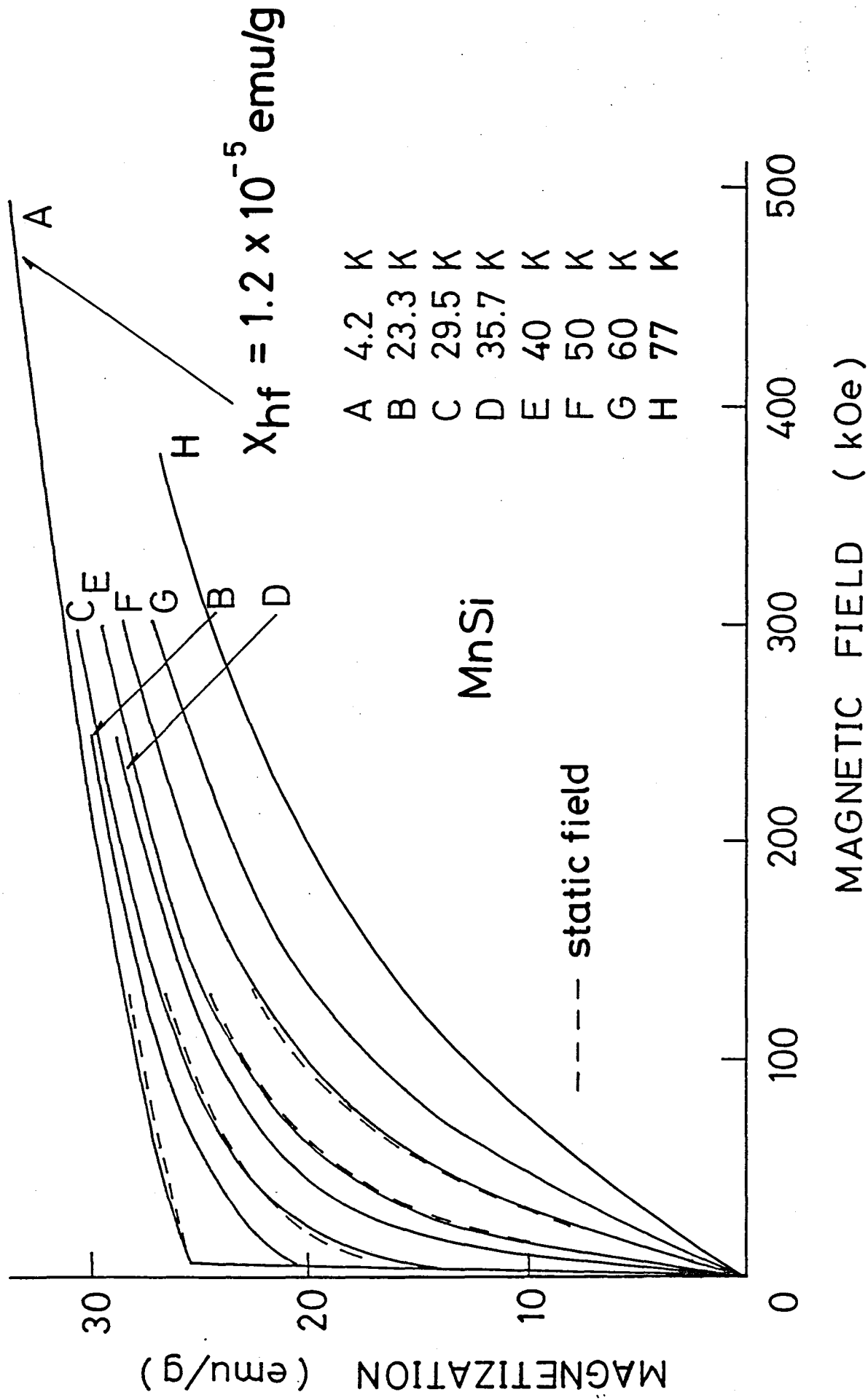


Fig. 30 Magnetization of MnSi. Dotted lines are static field results.

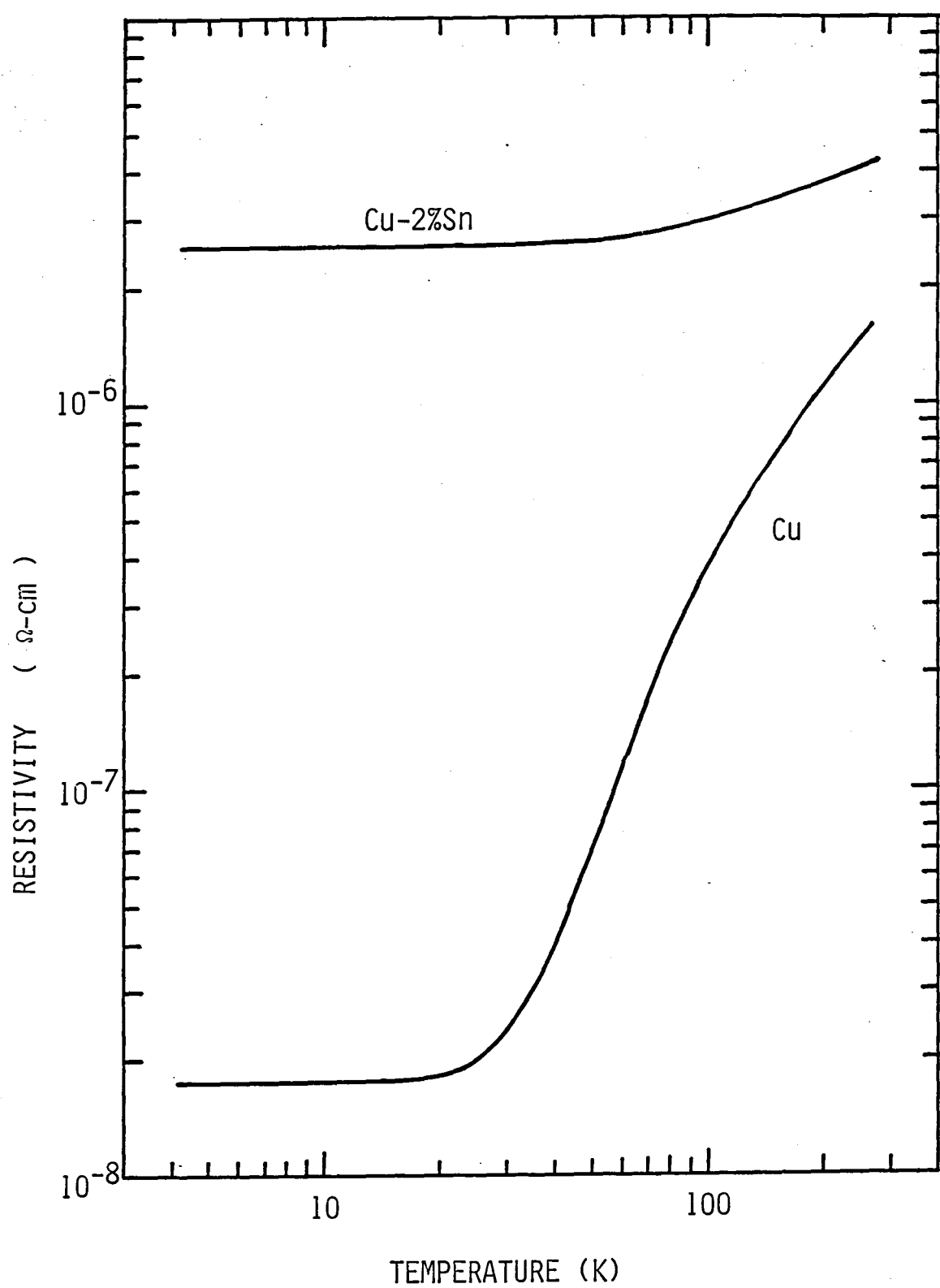


Fig. 31 Temperature dependence of the resistivity of Cu-2%Sn, compared with that of commercial Cu wire.

example, the internal resistance of the standard type pick-up coil changes from 10Ω to 18Ω at temperature range 4.2 K to R.T.. Therefore, pick-up coil load resistance R_L in Fig.1 should be taken off in the temperature controlled measurements, to avoid change in the output signal voltage.

4.2 Magnetocaloric Effect under Pulsed Field Measurement

One difficulty with the thermometry in the pulsed field measurements arises from the fact that the temperature is measured at zero field before and after the pulse, but not during the pulse. During the application of pulse field, the specimen may not be in thermal equilibrium with its surrounding heat bath because the thermal relaxation time may not be short compared with the duration of the field. Therefore, the temperature measured at $H_0=0$ may not be exactly the same as the temperature under the field. In consequence, one should be very careful for heating effects under pulsed magnetic field.

There are two heating effects under pulsed field . One is the Joule heating due to eddy current, and the other is the magnetocaloric effect. The former one can be avoided by reducing the dimension of the specimen, as is discussed in the preceding section. On the other hand, special care must be taken for the latter effect because it is thermodynamically intrinsic so that does not depend on the size of the specimen. Therefore, thermal relaxation time of the specimen becomes important.

The thermal relaxation time of the specimen depends on various conditions, such as spin-lattice relaxation time τ_{SL} , lattice-bath relaxation time τ_{LB} , lattice entropy, dimension D of the specimen, temperature and so on. Therefore, it is difficult to treat these things generally. The example of magnetization process when τ_{SL} is longer than the field duration T was given by Mollymoto²¹⁾. We consider here another case in which τ_{SL} is much shorter than T and the lattice has enough entropy. In such case, one can measure in nearly isothermal condition, or at least one can estimate and correct the temperature change under the pulsed field.

The material investigated is MnSi and the magnetization curve is already shown in Fig.30. τ_{SL} of this material is considered to be short enough, so that the spin system is always in thermal equilibrium with the lattice. In the magnetization measurement, powdered specimen molded with epoxy resin was used. In this case, τ_{LB} is of the order of D/v , where D is the particle radius (less than $40\mu\text{m}$) and v is the phonon velocity, and is estimated as less than $1\ \mu\text{s}$. Therefore, the spin system is also in thermal equilibrium with heat bath (epoxy resin) which has enough heat capacity, and the magnetization process is nearly isothermal. On the other hand, the magnetoresistance measurement of this material found to be in quite different situation, due to the use of single crystal specimen and poor thermal contact with the surroundings(helium gas). So, the thermal relaxation time was measured and the example is shown

in Fig.32. The single crystal of size $0.05 \times 0.1 \times 7$ mm was set in the cryostat with $T=32$ K. Current of 50mA (DC) was applied through the current terminals and the resistance was monitored. After applying heat-up current of 1 ampere for 0.5 ms (Fig.32b), the resistance recovered with time constant 2.5 ms (Fig.32a), and this may corresponds to τ_{LB} . The relaxation time τ_{LB} obtained is about ten times longer than the field rise time, so that adiabatic condition may hold. In this case, the temperature change dT due to magnetic field increase dH is given by standard formula as

$$dT = -(\partial S / \partial H)_T / (\partial S / \partial T)_H dH , \quad (13)$$

where S is the entropy of the system. Making use of the following relations

$$(\partial S / \partial H)_T = (\partial M / \partial T)_H , \quad (14)$$

$$(\partial S / \partial T)_H = C_H / T , \quad (15)$$

(13) can be written as

$$dT = - \frac{T}{C_H} (\partial M / \partial T)_H dH , \quad (16)$$

where C_H is the specific heat under the field. We can obtain $(\partial M / \partial T)_H$ by replottting Fig.30 as a function of T and the results

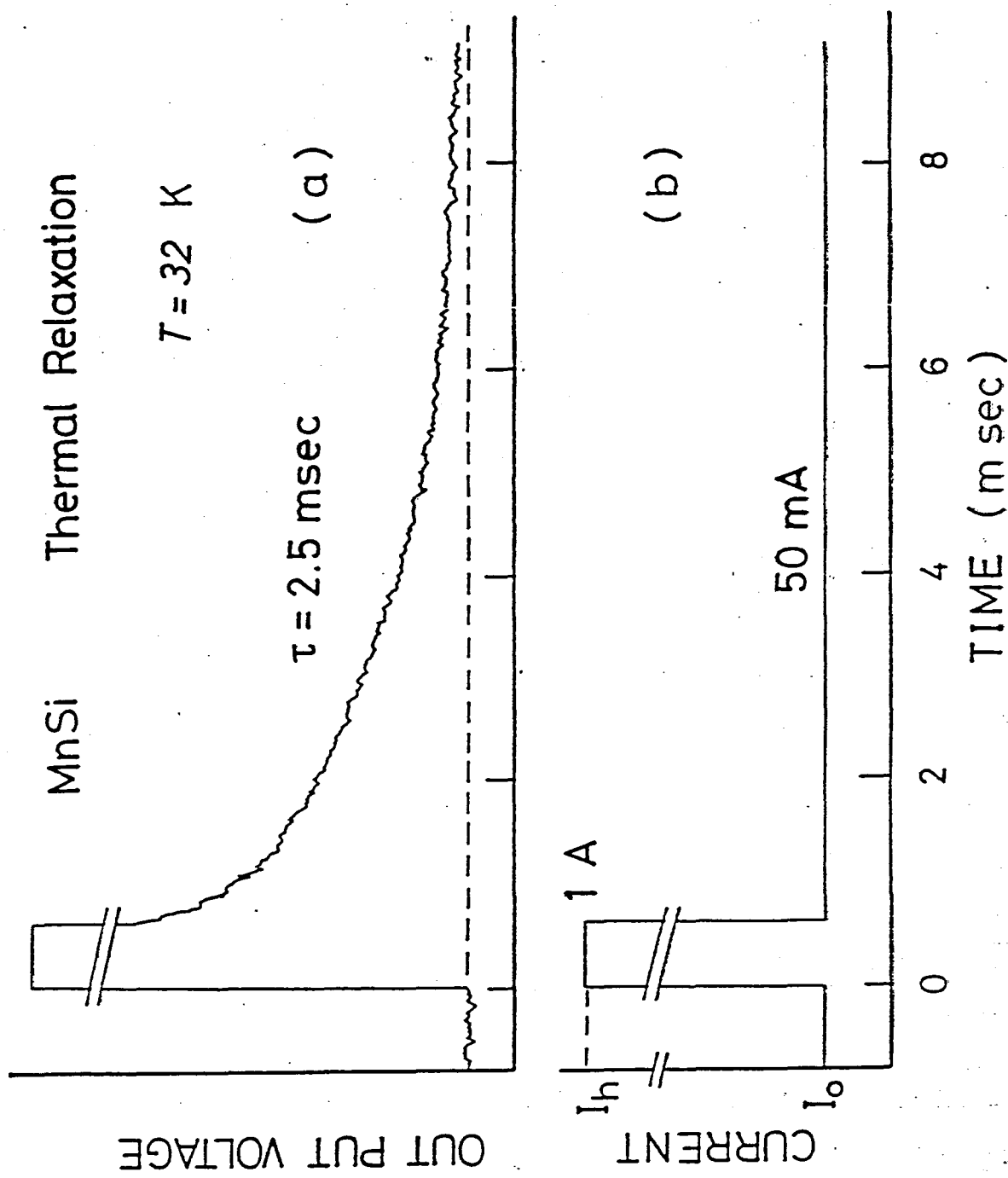


Fig. 32 Thermal relaxation of the specimen used in the magnetoresistance measurement. Figure (a) shows the recovery of the resistance with the

are given in Fig.33. C_H/T of course depends on H , but in this case the dominant contribution comes from electronic and lattice part so that the field dependence is weak. Making use of the static field data up to H_1 (9 kOe in ref.46), small change in C_H at higher field can be taken into account by the relation

$$C_H/T = C_{H1}/T + \int_{H1}^H (\partial^2 M/\partial T^2)_H dH. \quad (17)$$

From eqs.(16) and (17), one can estimate the temperature increase ΔT and the example of the results is given in Fig.34. Method of correction and the results of magnetoresistance measurement are shown in Fig.35. Consider the point A in the figure as an example of initial zero field resistivity. Applying magnetic field of 320 kOe adiabatically, the apparent resistivity decrease ΔR is observed (point B). The temperature increase ΔT is then estimated and the apparent temperature B is found to corresponds to the value at point C. In this manner, the true resistivity curve under pulsed magnetic field can be obtained³²⁾.

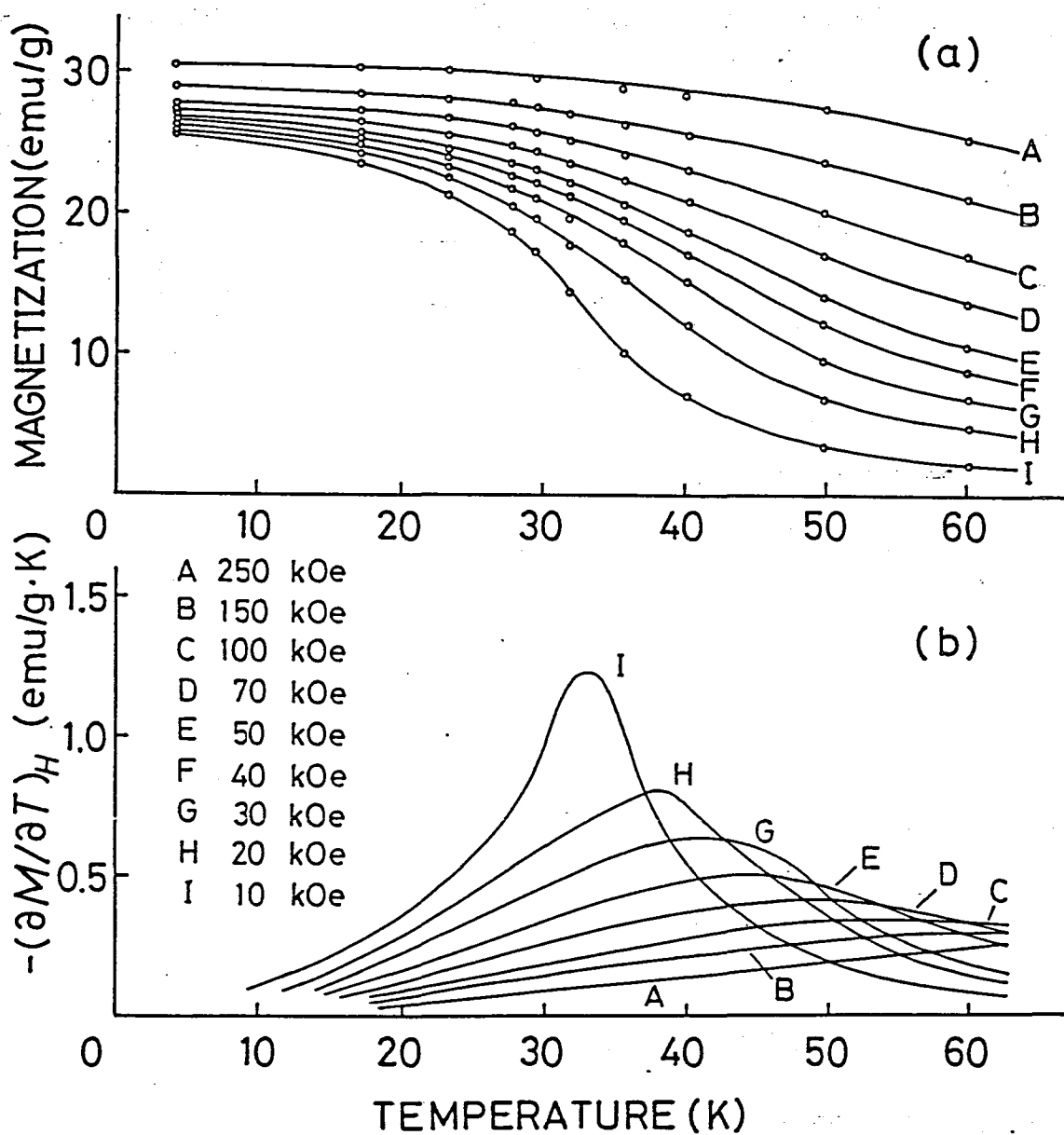


Fig.33 (a) Magnetization of MnSi powder specimen at various fields reproduced from the isothermal magnetization curves.
 (b) Temperature derivative of the magnetization.

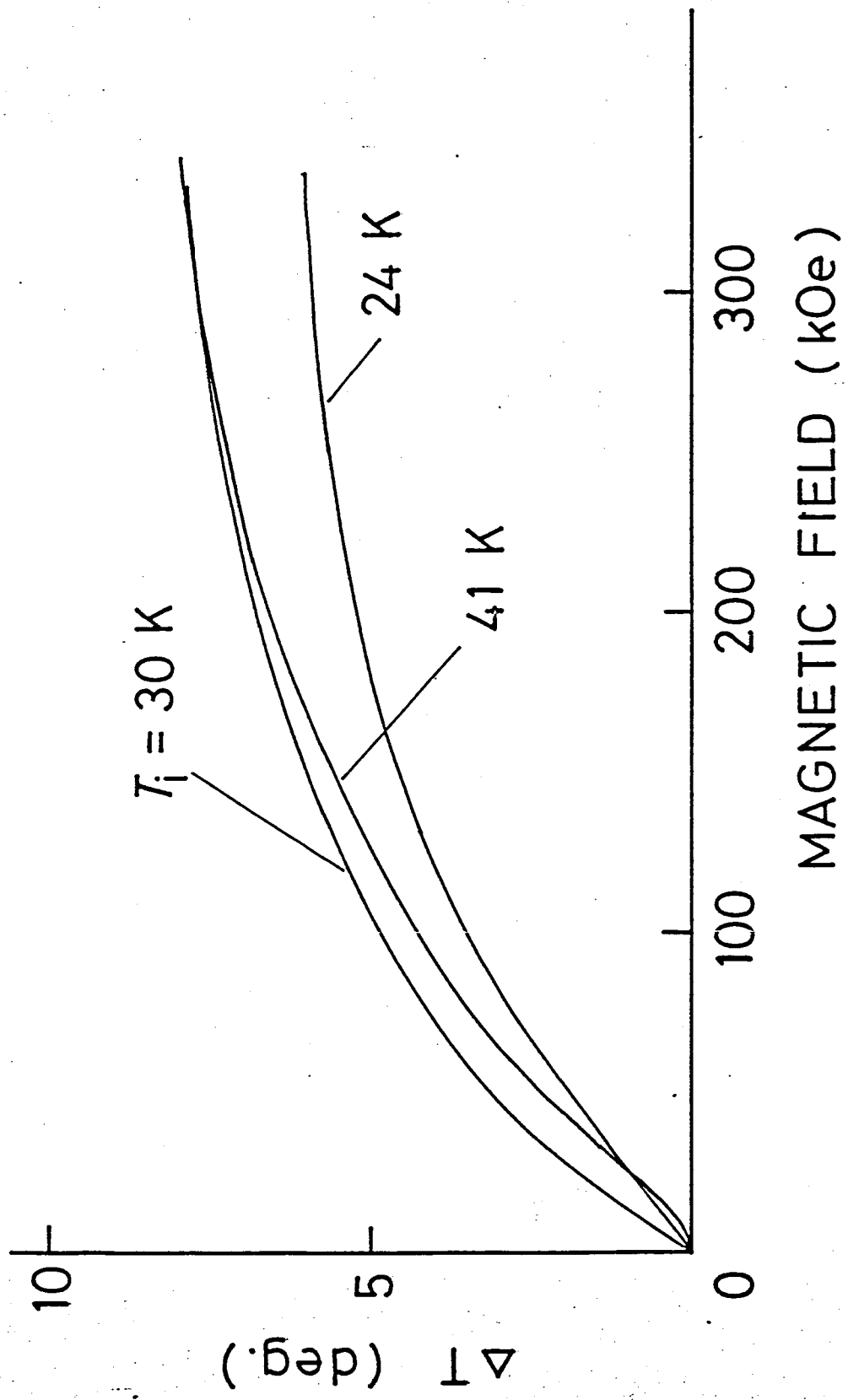


Fig. 34 Calculated temperature increase of MnSi under an adiabatic condition.

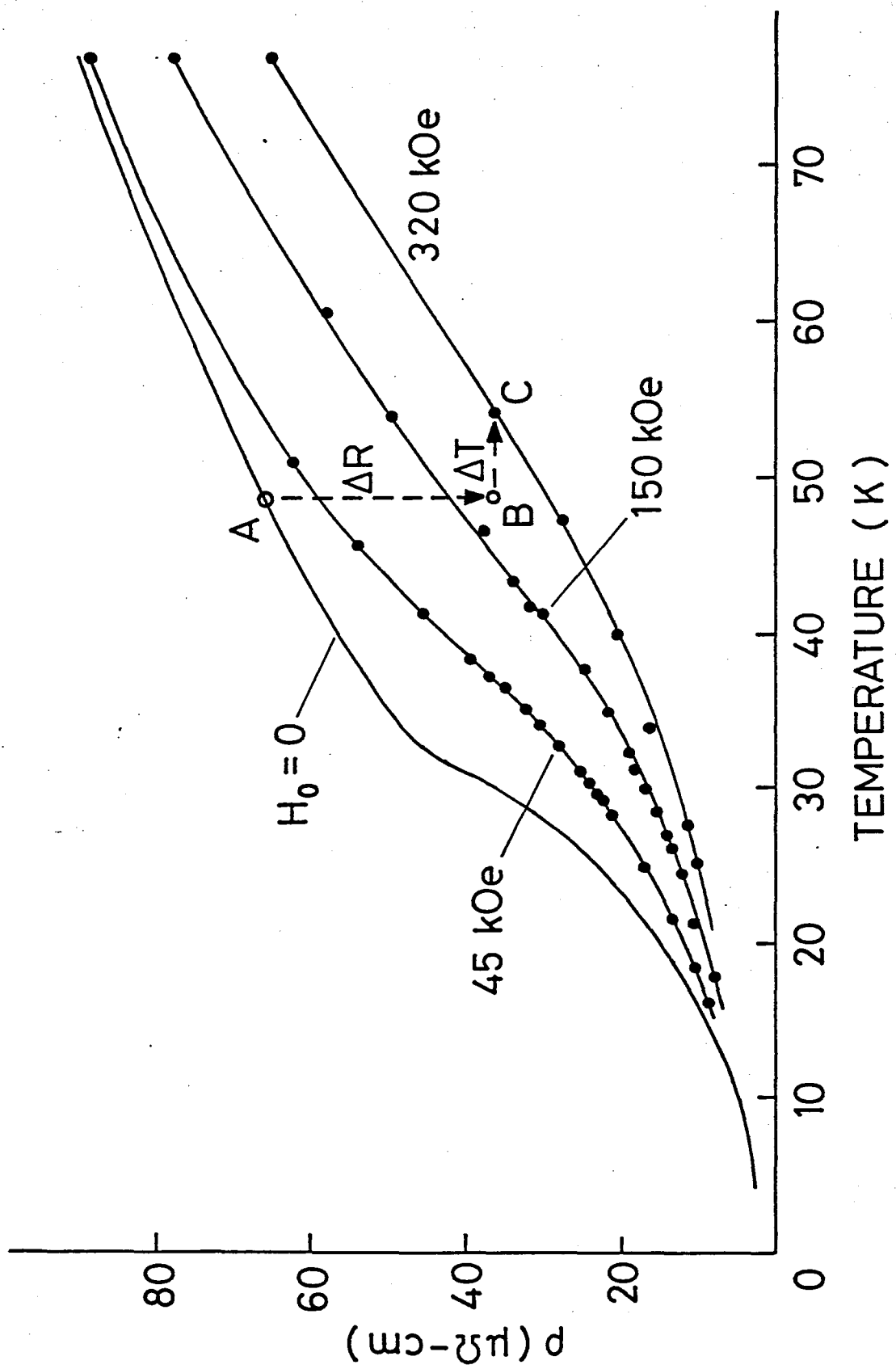


Fig. 35 Temperature corrected resistivity of MnS1 under pulsed magnetic field. Method of the correction is also shown.

REFERENCES

- 1) For example, T. Nagamiya, K. Yosida and R. Kubo: *Advan. Phys.* 4 (1955) 1.
- 2) Magnetism, ed. by Rado and Suhl, Academic Press, 1963.
- 3) S. Foner: *Phys. Rev.* 130 (1963) 183.
- 4) M. Date and M. Motokawa: *Phys. Rev. Lett.* 16 (1966) 1111.
- 5) M. Motokawa and M. Date: *J. Phys. Soc. Jpn.* 23 (1967) 1216.
- 6) For example, *Physics in High Magnetic Fields*, ed. by S. Chikazumi and N. Miura, Springer-Verlag, 1981; *Proc. Int. Symposium on High Field Magnetism*, Osaka, 1982.
- 7) M.J. Leupold, J.R. Hale, Y. Iwasa, L.G. Rubin and R.J. Weggel: *IEEE Trans Magnetics MAG-17* (1981) 1779.
- 8) R. Gersdorf, F.R. de Boer, J.C. Wolfrat, F.A. Muller and L.W. Roeland: *Proc. Int. Symposium on High Field Magnetism*, Osaka, 1982.
- 9) Y. Shapira and S. Foner: *Phys. Rev. B1* (1970) 3038.
- 10) Y. Shapira: *Phys. Rev. B2* (1970) 2725.
- 11) A.R. Fert, J. Gelard and P. Carrara: *Solid State Commun.* 13 (1973) 1219.
- 12) G. Busch, O. Vogt and H. Bartholin: *J. Physique Colloq.* 40 (1979) C4-64.
- 13) J. Kaczer and P. Novotny: *Phys. Stat. Sol.* 39 (1977) 351.
- 14) H. Bartholin, D. Florence, Wang Tcheng-si and O. Vogt: *Phys. Stat. Sol.* 29 (1975) 275.
- 15) H. Bartholin, D. Florence, Wang Tcheng-si and O. Vogt: *Phys. Stat. Sol.* 24 (1974) 631.

- 16) N.P. Grazhdankina, E.A. Zavadskii and I.G. Fakidov:
Sov. Phys. Solid State 11 (1970) 1879.
- 17) K. Selte, A. Kjeshus, A.F. Andersen and A. Zieba:
J. Phys. Chem. Solids 38 (1977) 719.
- 18) C.J. Schinkel, R. Hartog and F.H.A.M. Hochstenbach:
J. Phys. F4 (1974) 1412.
- 19) K. Adachi, M. Matsui, Y. Omata, H. Mollymoto, M. Motokawa
and M. Date: J. Phys. Soc. Jpn. 47 (1979) 675.
- 20) M. Date: J. Phys. Soc. Jpn. 39 (1975) 892; IEEE Trans.
Magnetics MAG-12 (1976) 1024; see also A. Seki: Thesis,
Osaka University, 1974.
- 21) H. Mollymoto: Thesis, Osaka University, 1980.
- 22) M. Matsuura, Y. Okuda, M. Morotomi, H. Mollymoto and M. Date:
J. Phys. Soc. Jpn. 46 (1979) 1031.
- 23) K. Okuda, H. Mollymoto and M. Date: J. Phys. Soc. Jpn. 47
(1979) 1015.
- 24) Y. Miyako, S. Chikazawa, T. Sato, Y.G. Yuochnuas,
M. Kobayashi, K. Katsumata, H. Mollymoto and M. Date:
J. Mag. Mag. Materials 15-18 (1980) 71.
- 25) H. Mollymoto, E. Fujiwara, M. Motokawa and M. Date:
J. Phys. Soc. Jpn. 48 (1980) 1771.
- 26) H. Mollymoto, M. Motokawa and M. Date: J. Phys. Soc. Jpn.
49 (1980) 108.
- 27) J.W. Bray, L.V. Interrante, I.S. Jacobs and J.C. Bonner:
Technical Information Series of General Electric Co,
No. 81CRD221, 1981.

(28) D. Bloch, J. Voiron and L.J. de Jongh: Proc. Int. Symposium on High Field Magnetism, Osaka, 1982.

(29) I. Harada and A. Kotani: J. Phys. Soc. Jpn. 51 (1982) 1737.

(30) K. Okuda, M. Kitagawa, T. Sakakibara and M. Date: J. Phys. Soc. Jpn. 48 (1980) 2157.

(31) K. Okuda, S. Noguchi, T. Honda and M. Date: to be published

(32) T. Sakakibara, H. Mollymoto and M. Date: J. Phys. Soc. Jpn. 51 (1982) 2439.

(33) M. Date, M. Motokawa, K. Okuda, H. Hori, H. Mollymoto and T. Sakakibara: J. Mag. Mag. Materials 15-18 (1980) 1559.

(34) A.R. King, V. Jaccarino, T. Sakakibara, M. Motokawa and M. Date; Phys. Rev. Lett. 47 (1981) 117; J. Appl. Phys. 53 (1982) 1874 ; Proc. Int. Conf. Mag. Kyoto, 1982.

(35) H. Suematsu, K. Ohmatsu, K. Sugiyama, T. Sakakibara and M. Date: Solid State Commun. 40 (1981) 241.

(36) M. Sugita, S. Kunii, K. Takegahara, N. Sato, T. Sakakibara, P.J. Markowski, M. Fujioka, M. Date and T. Kasuya: Crystalline Field Effects in f-Electron Magnetism, ed. by Guertin, Suski and Zolnierenk, Plenum Publishing Co, 1982.

(37) T. Sakakibara, K. Okuda and M. Date: Proc. Int. Conf. Mag. Kyoto, 1982.

(38) M. Date, M. Motokawa, A. Yamagishi, H. Hori, T. Sakakibara and K. Sugiyama: Proc. Int. Conf. Mag. Kyoto, 1982.

(39) V. Jaccarino, A.R. King, M. Motokawa, T. Sakakibara and M. Date: Proc. Int. Conf. Mag. Kyoto, 1982.

(40) T. Sakakibara, H. Mollymoto, M. Motokawa and M. Date:
Proc. Int. Symposium on High Field Magnetism, Osaka, 1982.

(41) T. Suzuki, S. Takagi, N. Niitsuma, K. Takegahara, T. Kasuya,
A. Yanase, T. Sakakibara, M. Date, P.J. Markowski and Z.
Henkie: Proc. Int. Symposium on High Field Magnetism, Osaka,
1982.

(42) K. Hanzawa, T. Kasuya, T. Komatsubara, T. Sakakibara and
M. Date: Proc. Int. Symposium on High Field Magnetism,
Osaka, 1982.

(43) M. Date, T. Sakakibara, K. Sugiyama and H. Suematsu:
Proc. Int. Symposium on High Field Magnetism, Osaka, 1982.

(44) H. Ido, T. Harada, K. Sugiyama, T. Sakakibara and M. Date:
Proc. Int. Symposium on High Field Magnetism, Osaka, 1982.

(45) D. Bloch, J. Voiron, V. Jaccarino and J.H. Wernick: Phys.
Lett. 51A (1975) 259.

(46) E. Fawcett, J.P. Maita and J.H. Wernick: Int. Magn. 1
(1970) 29.

PART II

FOUR-SPIN EXCHANGE IN

EUROPIUM GRAPHITE INTERCALATION COMPOUND C_6Eu

ABSTRACT

High field magnetizations of europium graphite intercalation compound C_6Eu are measured up to 400 kOe in a temperature range 4.2 K to $T_N=40$ K. A clear metamagnetic plateau with 1/3 moment of saturated value is observed in the c-plane magnetization. Analysis of the magnetization process based on molecular field theory has shown strong evidence for the existence of a weak four-spin exchange interaction in addition to usual two-spin exchange. This is the first clear example of the four-spin exchange coupling in the Ruderman-Kittel-Kasuya-Yosida(RKKY) interaction system. The coefficients of four-spin-ring and biquadratic terms are determined satisfactorily.

§1. INTRODUCTION

Graphite intercalation compounds (GIC) with magnetic intercalants have been attracting much attention in these years. The main interests are taken on the low dimensional character of their magnetic interactions. One can separate the magnetic layers by controlling the number of graphite layers (stages) between them. For example, high stage compounds of graphite- MCl_2 , ($M=Fe, Co, Ni$) are expected as prototype of 2-dimensional XY-ferromagnet and their magnetic orderings are studied^{1,2)}. In addition to the low dimensionality, it may also be interesting and important point that the intercalants form triangular lattices in these compounds. When the magnetic interaction in the intercalant plane is antiferromagnetic, competition or frustration of the interaction will provide variety of magnetic properties^{3~5)}.

Recently, first stage europium-GIC C_6Eu was synthesized⁶⁾ and the magnetic measurements were done⁷⁾. The compound was revealed as an antiferromagnet with XY-like anisotropy. However, the magnetization showed an anomalous behaviour and no clear result was obtained because the field strength was not enough to observe the whole magnetization process. To clarify this point, we have measured high field magnetizations of C_6Eu ⁸⁾. The purpose of the present paper is to report the experimental results and the analysis on the magnetization process of this compound.

We have found a ferrimagnetic plateau with $1/3$ of the full moment in the magnetization process along the intercalant plane. As will be shown later, the plateau can not be explained by considering only usual two-spin exchange interactions. It is found that weak four-spin exchange interactions between localized Eu spins are necessary to explain the experimental results.⁹⁾

Historically speaking, importance of the four-spin exchange was first pointed out on solid ^3He , a quantum solid with nuclear spin $1/2$. The anomalous magnetic properties and structure were well explained successfully by considering strong four-spin exchange interaction caused by large quantum fluctuation of ^3He atoms^{10,11)}. The second example is NiS_2 , a typical Mott insulator located near the metal-insulator phase boundary^{12~14)}. Perturbation expansion of the Hubbard model from the insulator limit showed that higher order exchange interactions will become important in such case^{12,15)}. Taking into account the four-spin exchange, complex spin structure of NiS_2 was explained¹⁴⁾. The possible spin structures of electron Wigner lattice on liq. ^4He surface is also discussed by taking the four-spin exchange interaction into account¹⁶⁾. These systems are rather exceptional cases where large fluctuation of the systems cause considerable amount of higher order interactions. In usual well localized spin systems, on the other hand, magnitude of the higher order terms are very small but they should exist definitely¹⁷⁾.

In fact, the existence of biquadratic exchange interaction of the form $(S_i S_j)^2$ is reported on some Mn-compounds^{18,19}.

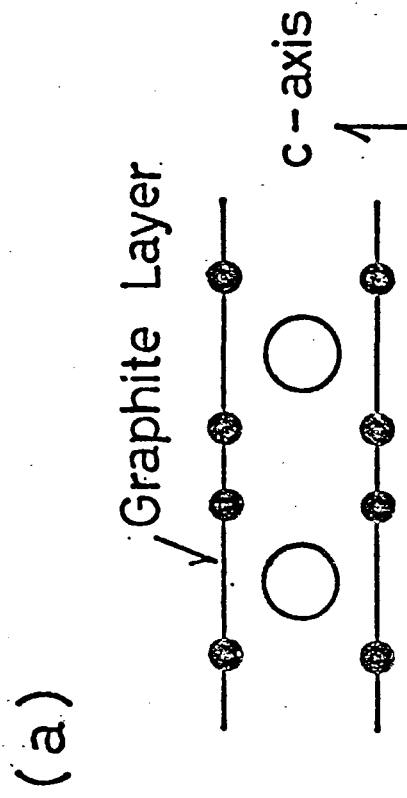
The four-spin exchange found in C_6Eu is actually very small in its magnitude, reflecting well defined local moment of Eu. The reasons that we could confirm such weak interaction in this system are followings: Eu is in nearly spherical divalent state with large spin value, and the spins form an antiferromagnetic triangular lattice. The latter means that the spin structure can easily be modified by introducing weak interactions⁴). As an example, we have also found that the spin-triangular state (120°-state), which is the ground state of a triangular lattice easy plane antiferromagnet, is intrinsically unstable against weak interaction between two adjacent triangular planes in the hexagonal closed pack (hcp) lattice. The details will be given in APPENDIX.

§ 2. CRYSTAL STRUCTURE AND MAGNETIC PROPERTIES OF C_6Eu

Crystal structure of C_6Eu is shown in Fig.1. This system is so called first stage compound. Eu atoms are located on center of graphite hexagons and form triangular lattices which are separated by single carbon layer. The inter layer distance between the Eu layers is 4.87 \AA^6 . Eu atoms form a hexagonal closed pack (hcp) structure as shown in Fig.1 (b). In the figure, exchange constants J_0 , J_1 and J' are given for later discussions.

The temperature dependence of the electrical resistivity along the Eu-plane (c-plane) is given in Fig.2 (a). The graphite π -band of this system shows metallic conductivity because it accepts two excess electrons from Eu atom. The electrical resistivity ρ_{\perp} in c-plane is of the order of $10^{-6} \Omega\text{cm}$ at 4.2 K, while ρ_{\parallel} along c-axis is about 10^2 times larger than ρ_{\perp} . Therefore, the system can be looked at as an example of a two dimensional conductor.

Magnetic properties of C_6Eu have first been studied by Suematsu et al.⁸⁾, using c-axis oriented polycrystalline specimen obtained from HOPG (highly oriented pyrolytic graphite). The magnetic susceptibility shows Curie-Weiss law above 40 K with the Weiss constant 1.3 K. An antiferromagnetic order is observed below the Néel temperature $T_N = 40$ K. Figure 2b shows inverse susceptibility χ^{-1} in the c-plane. Below T_N , χ is measured at high magnetic field (100 kOe) because metamagnetic behaviour is found with non-linear magnetization in the low field region⁸⁾.



- 84 -

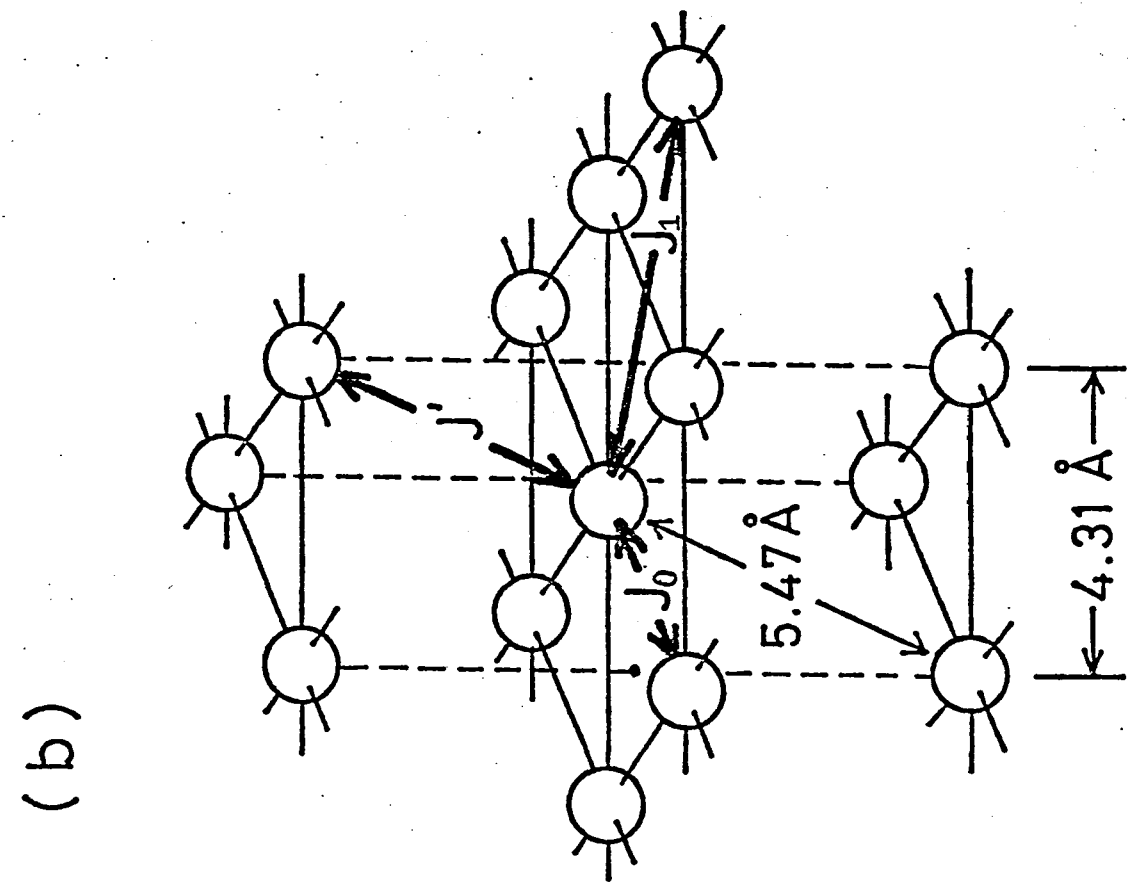


Fig.1 Crystal structure of C_6Eu . Europium layer is separated by one graphite layer as shown in (a). Europium atoms form hcp lattice given in (b). Three exchange parameters J_0 , J_1 and J' are defined.

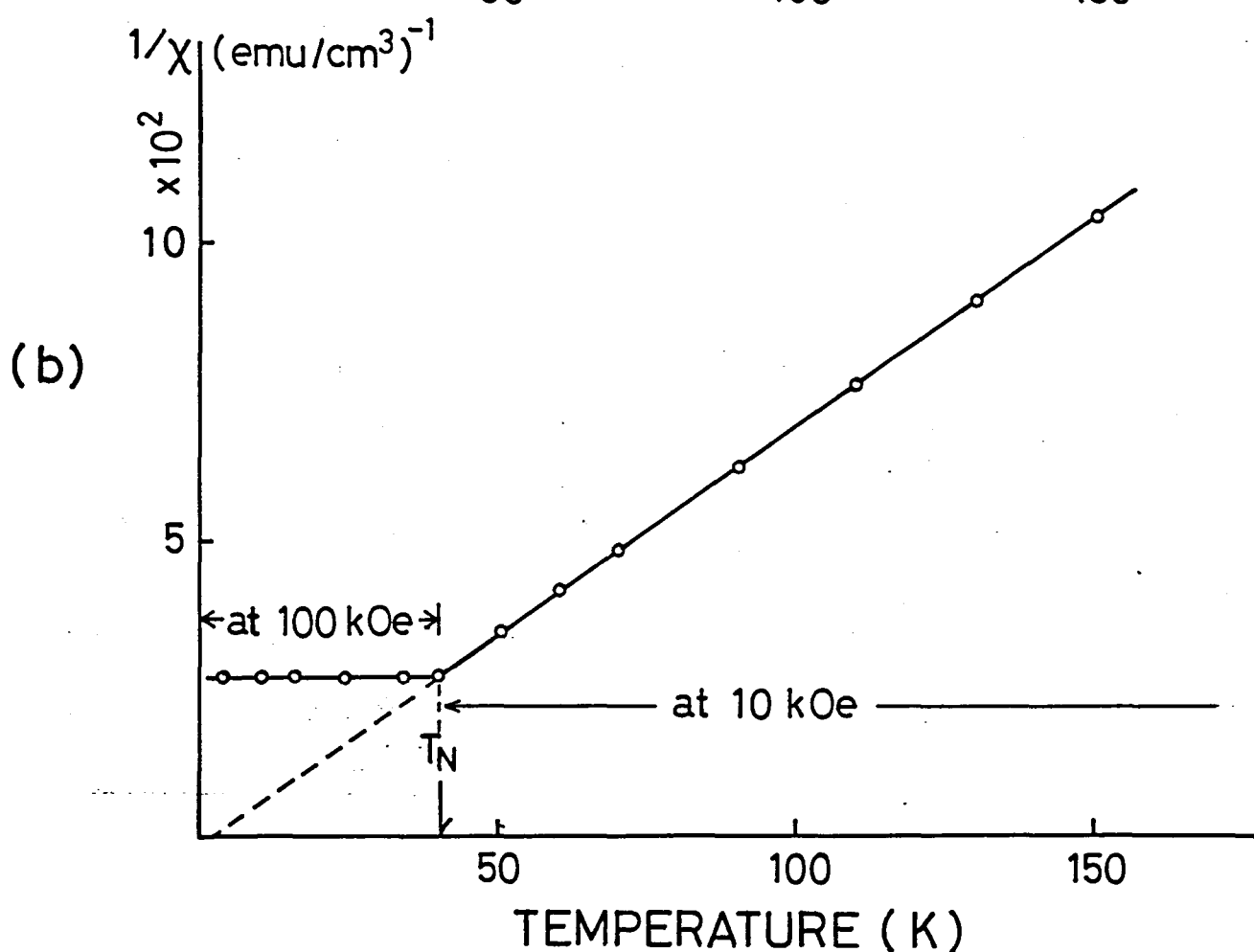
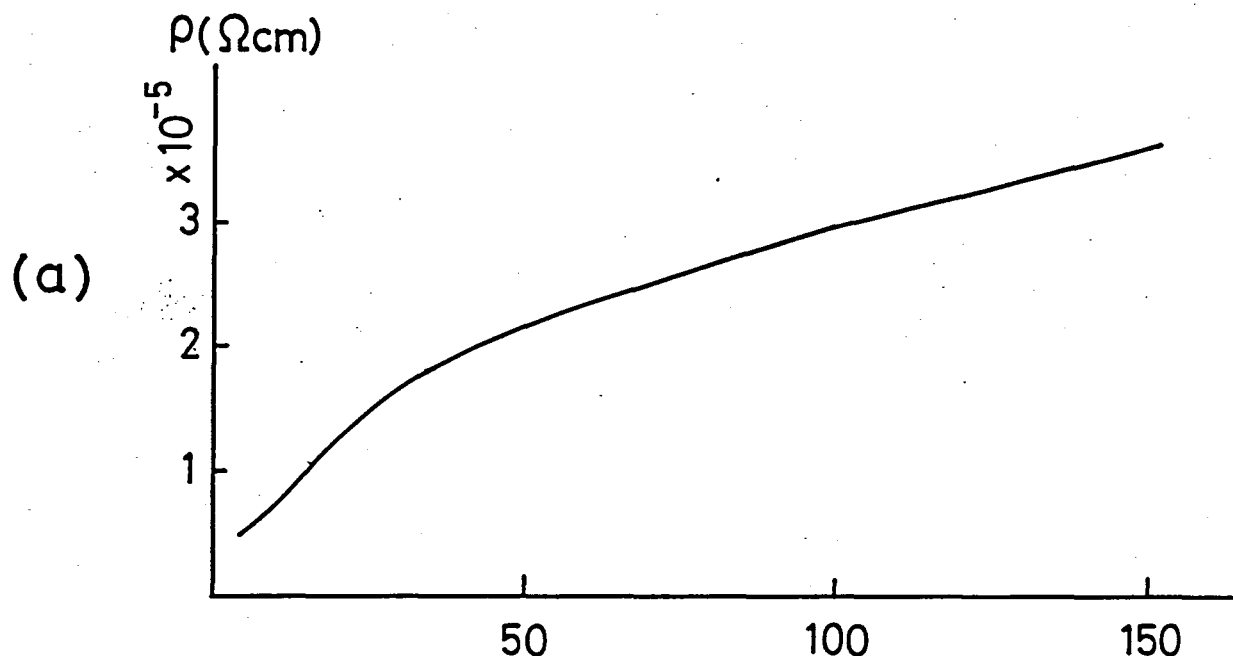


Fig.2 (a) Electrical resistivity of C_6Eu along c-plane.
 (b) Magnetic susceptibility of C_6Eu , $H_0//\text{c-plane}$.

As χ shows little temperature dependence below T_N , the in-plane magnetic anisotropy of this system will be weak. The susceptibility along c-axis is similar in the temperature dependence to that in the c-plane, but the magnitude is a little smaller than the in-plane value. From the Curie constant, Eu atom is determined as in divalent state. This point is recently confirmed by ^{151}Eu -Mössbauer spectroscopy²⁰⁾, which revealed no trace of Eu^{3+} in this system. Thus, noticing that the ground state of Eu^{2+} is $^8\text{S}_{7/2}$, C_6Eu can be considered as an easy-plane antiferromagnet with weak magnetic anisotropy in the c-direction.

Considering both the electric and magnetic properties described above, the following model may be accepted: dominant exchange interactions, which mainly come from RKKY interactions, may be in the triangular spin plane although the interplane exchange interaction can not be negligible. The fact that the Weiss constant is very small compared with T_N probably indicates the averaging of in-plane exchange as is expected from the long range RKKY interaction.

§ 3. RESULTS OF HIGH FIELD MAGNETIZATION MEASUREMENTS

The high field magnetization measurements at 4.2 K were done using D-1 1L magnet. The D-2 1L magnet and the temperature controlled cryostat were used to cover the temperature range 4.2 K to T_N . The samples were polycrystalline HOPG C_6Eu , the same specimens used in Ref.8. The typical size of the specimen was 1.6 x 2.3 x 0.67 mm and the shortest axis was the c-axis. The external field was applied parallel or perpendicular to the c-axis. The data taken at 4.2 K are shown in Fig.3. Three critical fields H_{c0} , H_{c1} and H_{c2} , which are obtained as 16, 64 and 215 kOe respectively, are found when the field H_0 is applied in the c-plane ($H_0 \perp c$). The magnetic moment is saturated above H_{c2} . The saturation value is about $6.5\mu_B/Eu$, nearly equal to the full moment of $7\mu_B$ expected for Eu^{2+} . Between H_{c0} and H_{c1} , a metamagnetic plateau with $1/3$ moment of the saturation magnetization is observed. The magnetization process between H_{c1} and H_{c2} is nearly straight line that can be extrapolated to the origin. On the other hand, no plateau is observed for $H_0 // c$ -axis, although the eddy current induced in the conductive c-plane has caused large hysteresis in the magnetization. Figure 4 shows the temperature dependence of the plateau. The plateau is clearly seen at low temperature but it becomes broad as the temperature increases, and disappears around 30 K, far below T_N . Low field region of our experimental results (below 50 kOe) is in good agreement with the results of Ref.8.

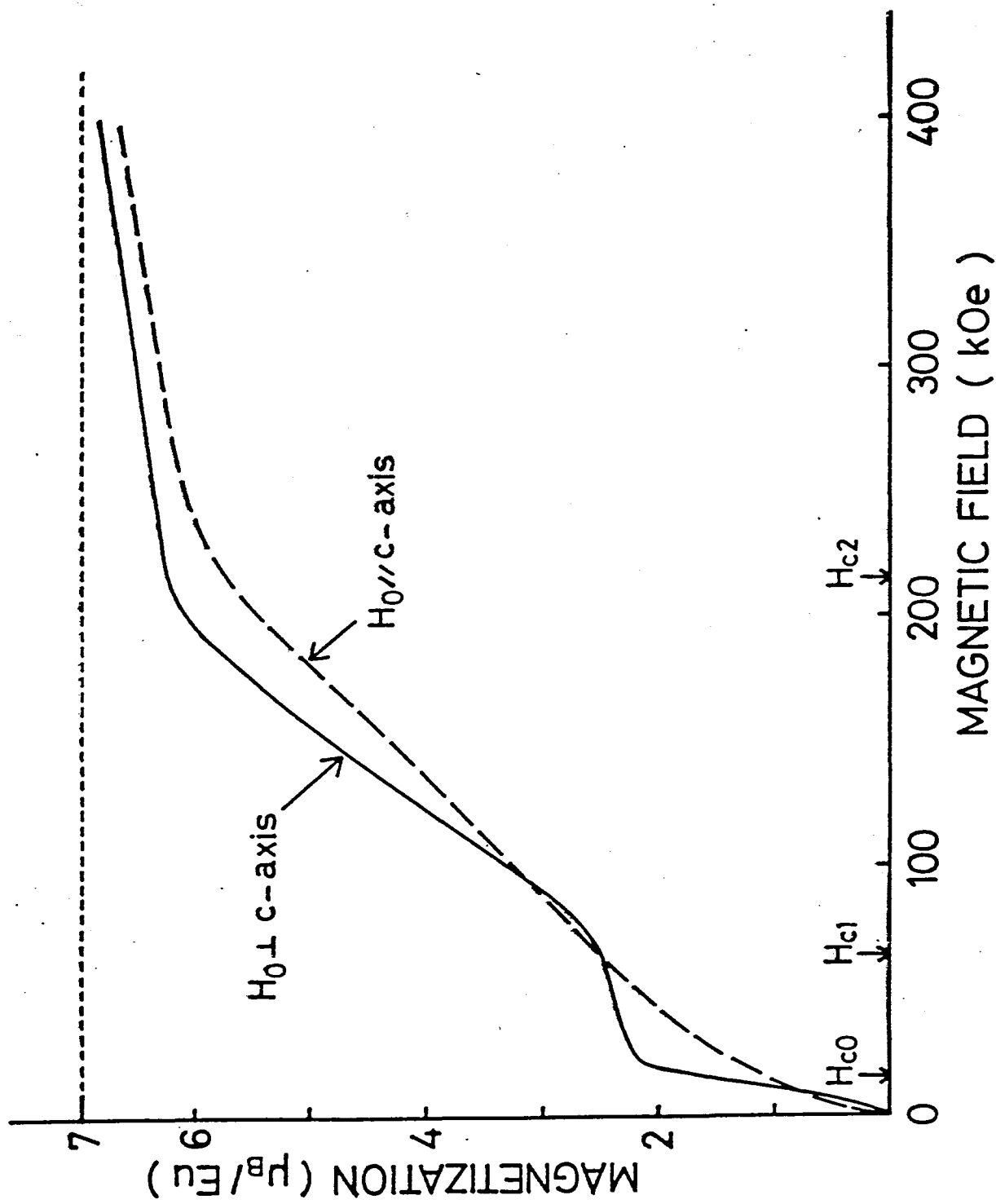


Fig. 3 Magnetization curves of C₆Eu at 4.2 K. Three critical fields H_{c0}, H_{c1} and H_{c2} are defined.

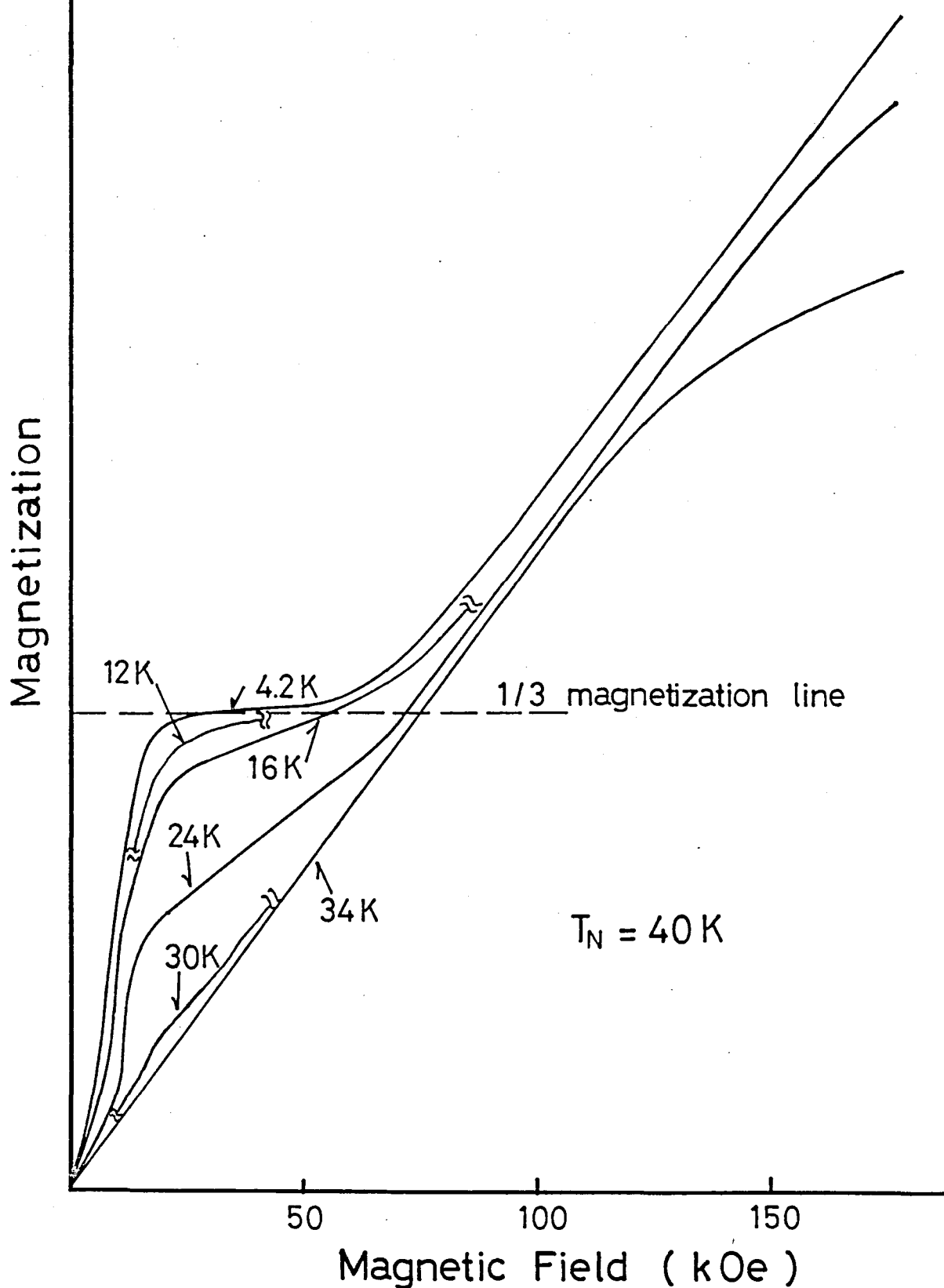


Fig.4 Temperature dependence of the magnetization curves of C_6Eu . Magnetic field is applied along the c-plane.

§ 4. MAGNETIZATION PROCESS WITHOUT FOUR-SPIN EXCHANGE

In this section, the c-plane magnetization process of C_6Eu is discussed in terms of usual two-spin (bilinear) exchange interactions. For simplicity, we first consider only the dominant intraplane nearest neighbour exchange interaction J_0 defined in Fig.1 (b). In this case, J_0 should be antiferromagnetic ($J_0 < 0$). In the absence of an external field, the stable spin structure of the triangular lattice is the well known spin-triangular state (Δ -state) as is shown in Fig.5 (a), where spins are rotating successively by 120° . On the other hand, the experimentally observed metamagnetic plateau with $1/3$ -moment should be the ferrimagnetic state (FI-state) as has been reported in $CuCl_2 \cdot 2H_2O^{21}$, and the structure is given in Fig.5 (b). Both states can be described by the same three sublattice model with magnetic moments \vec{M}_1 , \vec{M}_2 and \vec{M}_3 ($|\vec{M}_1| = |\vec{M}_2| = |\vec{M}_3| = M = Ng\mu_B S/3$) coupled to each other by a molecular field constant $\lambda = -18J_0/Ng^2\mu_B^2$, where N is the total spin number, g is the g -value and μ_B is the Bohr magneton. When the external field H_0 is applied, the three sublattice free energy at $T=0$ is given by

$$U = \lambda(\vec{M}_1\vec{M}_2 + \vec{M}_2\vec{M}_3 + \vec{M}_3\vec{M}_1) - \vec{H}_0(\vec{M}_1 + \vec{M}_2 + \vec{M}_3). \quad (1)$$

Defining angles α , β , β_1 and β_2 as in Fig.6 (a) and (c), the free energies of Δ - and FI-states are written in the page 93 as

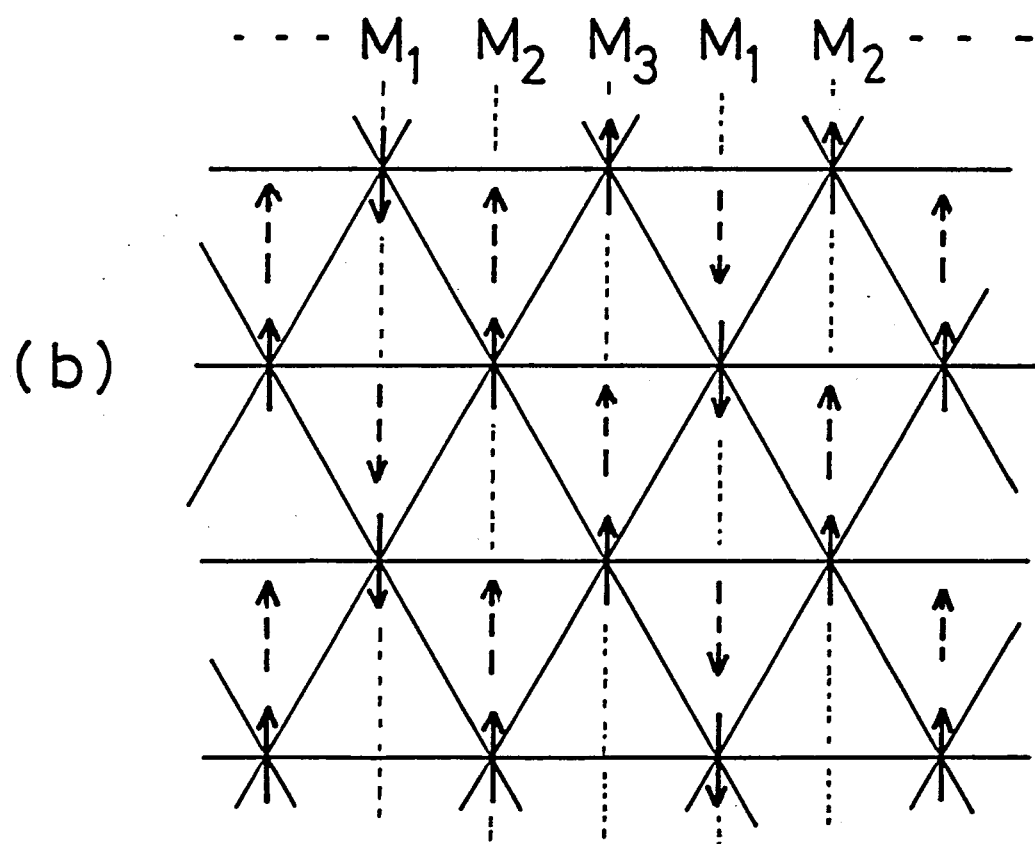
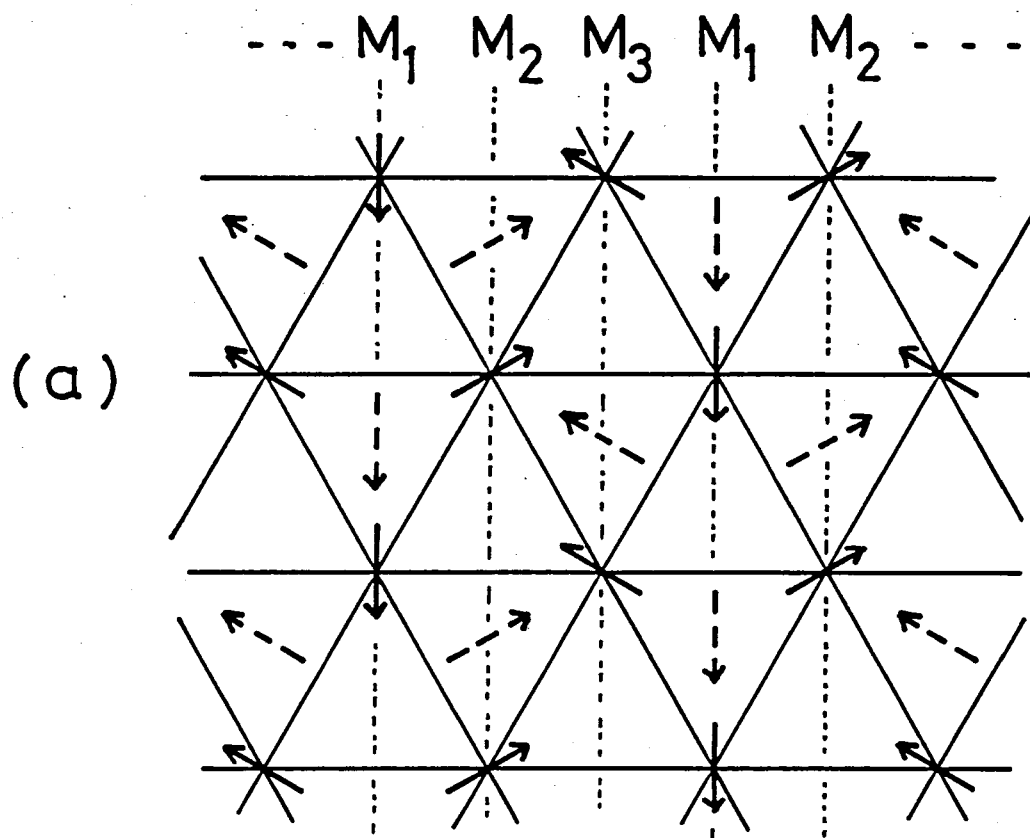


Fig.5 Spin structure of spin-triangular state(a) and ferrimagnetic state(b). Dotted arrows denote the spins on the adjacent plane. Three sublattices M_1 , M_2 and M_3 are shown.

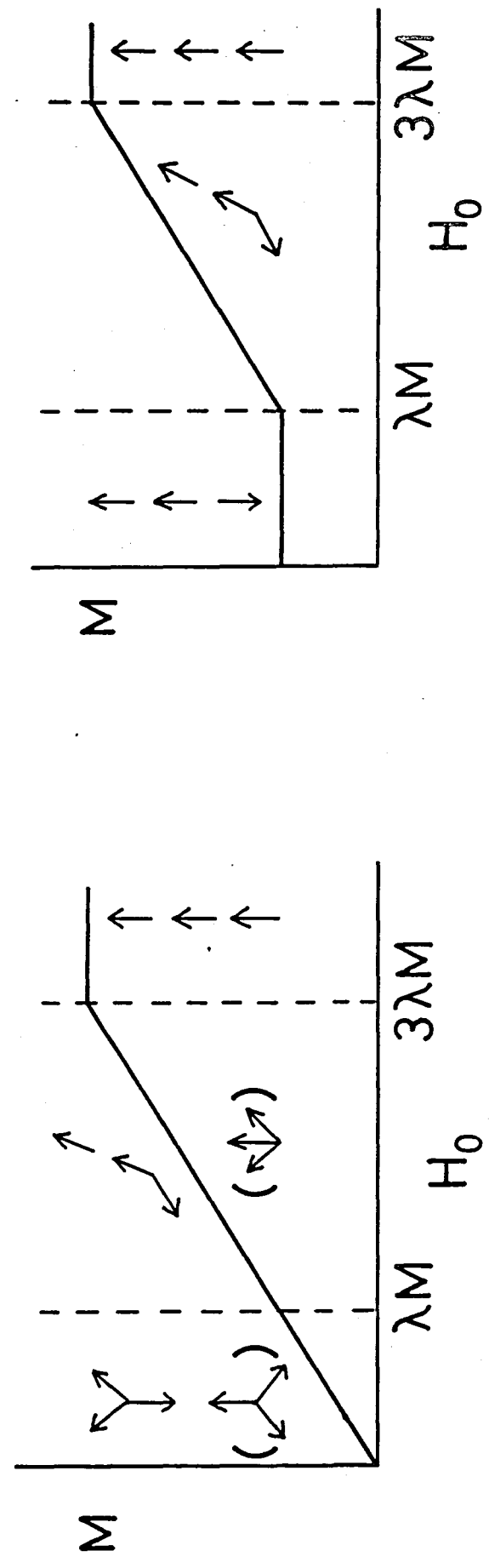
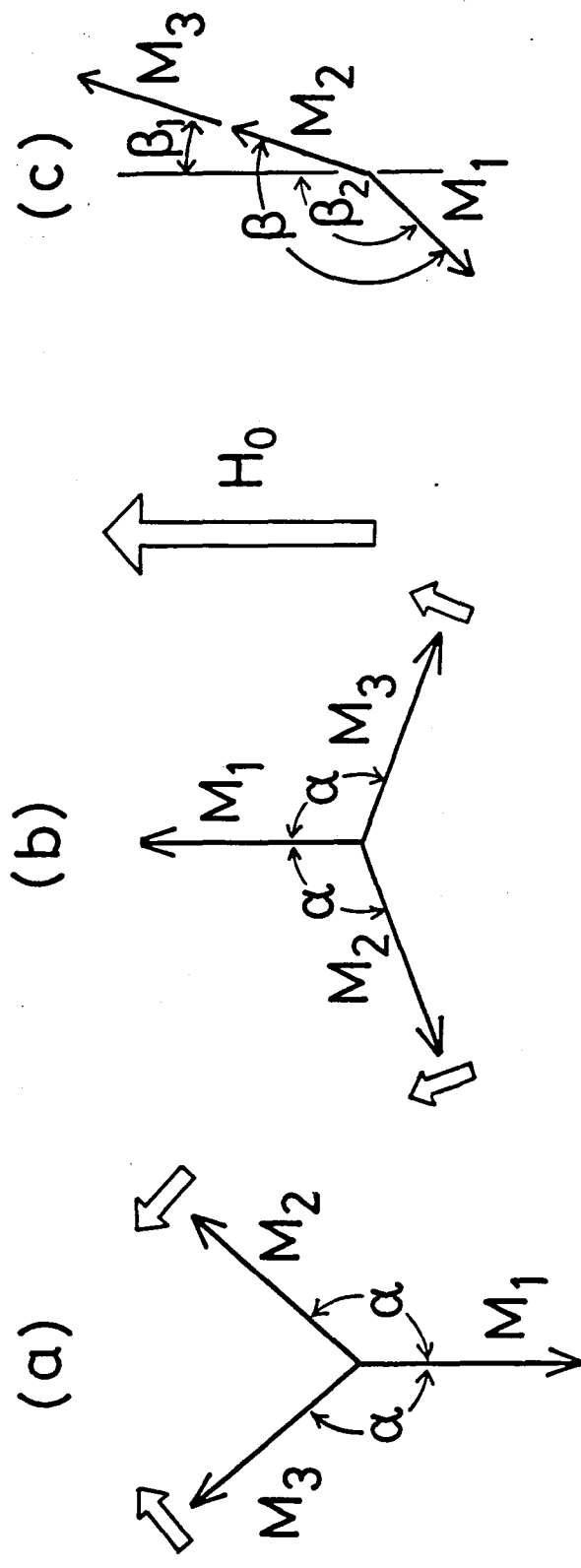


Fig.6 Models of magnetization process for Δ -state (a,b) and FI-state (c).
State-(b) becomes unstable when four-spin exchange is taken into account.

$$U_{\Delta} = \lambda M^2 (2\cos\alpha + \cos 2\alpha) + M H_0 (1 + 2\cos\alpha), \quad (2)$$

$$U_{FI} = \lambda M^2 (1 + 2\cos\beta) - M H_0 (2\cos\beta_1 + \cos\beta_2), \quad (3)$$

where the intrasublattice energy is not shown. The theoretical magnetization curves can be obtained by minimizing the free energies with respect to the angles under the condition

$$\sin\beta_2 = 2\sin\beta_1. \quad (4)$$

The FI-state is considered first. The magnetization process is divided into three regions by two critical fields $H_{c1} = \lambda M$ and $H_{c2} = 3\lambda M$. The free energy of each region is given as

$$U_{FI} = \begin{cases} -\lambda M^2 - M H_0, & (H_0 < H_{c1}), \end{cases} \quad (5)$$

$$U_{FI} = \begin{cases} -\frac{H_0^2}{2\lambda} - \frac{3}{2}\lambda M^2, & (H_{c1} < H_0 < H_{c2}), \end{cases} \quad (6)$$

$$U_{FI} = \begin{cases} -3M H_0 + 3\lambda M^2, & (H_{c2} < H_0). \end{cases} \quad (7)$$

The corresponding magnetization curve is given in Fig.6 (c). The magnetization has constant value M in the region $H_0 < H_{c1}$ while the system shows a canted spin structure between H_{c1} and H_{c2} where the magnetization increases linearly proportional to H_0/λ , and the ferromagnetic state appears above H_{c2} .

On the other hand, the magnetization of Δ -state increases linearly up to $H_0 = \lambda M$ with the free energy expressed as

$$U_{\Delta} = -\frac{H_0^2}{2\lambda} - \frac{3}{2}\lambda M^2, \quad (H_0 < \lambda M). \quad (8)$$

At $H_0 = \lambda M$, the Δ -state defined by Fig.6 (a) undergoes a phase transition to FI-state. The Δ -state is exactly ferrimagnetic at $H_0 = \lambda M$ and follows the same magnetization process as FI-state above $H_0 = \lambda M$. In other words, Δ -state only exist below $H_0 = \lambda M$. It is noticed that the spin configuration given by Fig.6 (b) is also possible with equal energy. In this case, there is no phase transition at $H_0 = \lambda M$ and the system is triangular up to $H_0 = 3\lambda M$. As will be shown later, however, the state given by Fig.6 (b) can not be stable when higher order exchanges are taken into account.

Free energies of Δ - and FI-state are compared in Fig.7, where the magnetization process of each state is also shown. Below $H_0 = H_{c1}$ ($= \lambda M$), Δ -state is lower in the energy so that the magnetization of the spin system first increases linearly. At $H_0 = H_{c1}$, the free energy of Δ -state coincides with FI-state and the system becomes ferrimagnetic. However, the FI-state takes a canted structure above H_{c1} so that the magnetization is again linear between H_{c1} and H_{c2} . Therefore, the whole magnetization process is linear up to $H_0 = H_{c2}$, as is expected.

In the next place, intraplane second neighbour exchange J_1 and interplane exchange interaction J' are considered

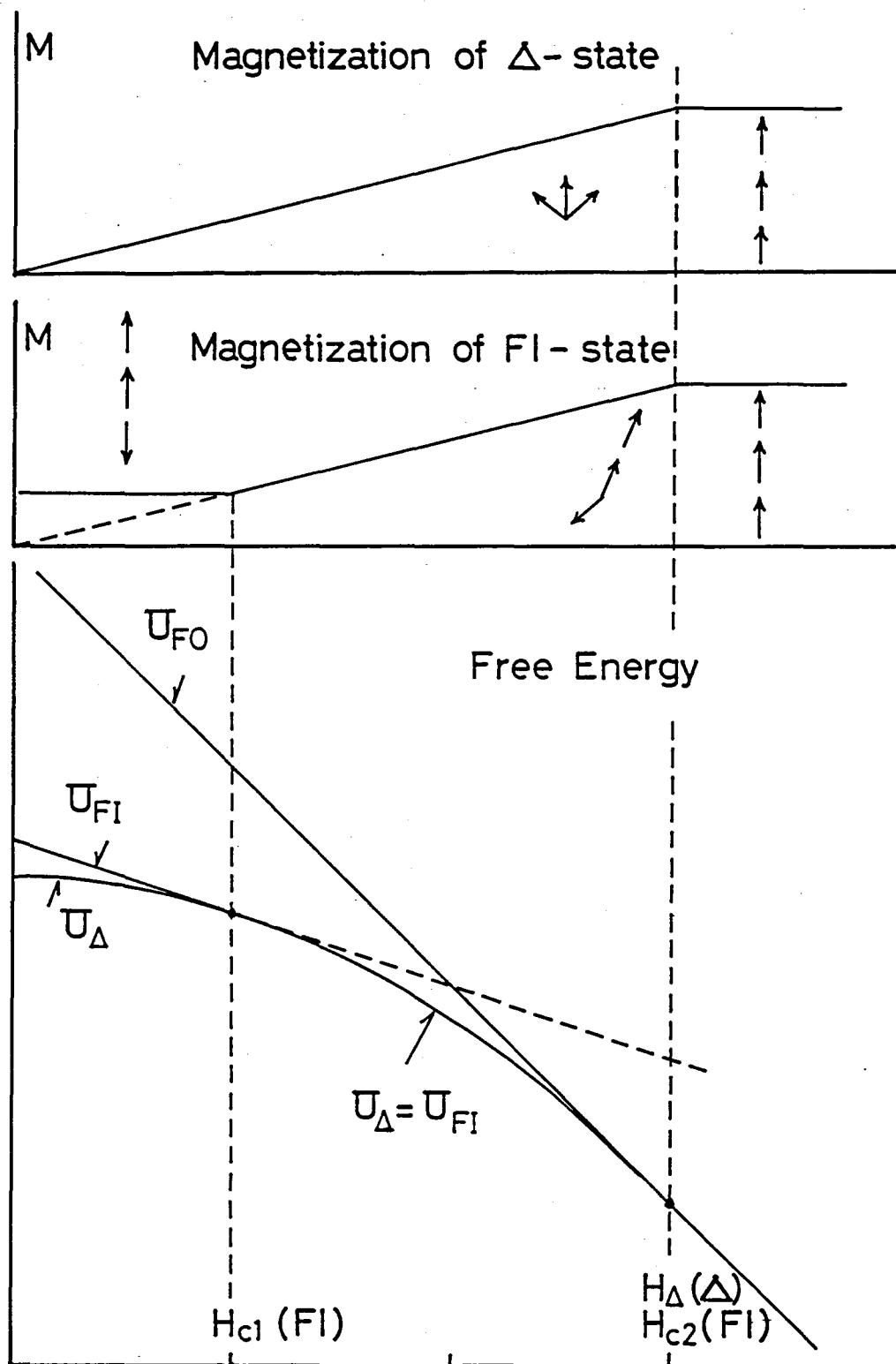


Fig.7 Magnetizations and free energies without four-spin exchange. Suffixes Δ and FI mean the triangular and ferrimagnetic states, respectively.

in addition to J_0 . The ground state spin configurations with respect to J_0 , J_1 and J' are first examined and the phase diagrams are given in Fig.8 for (a) $J_0 < 0$ (antiferromagnetic) and (b) $J_0 > 0$ (ferromagnetic). These phase diagrams are obtained by the standard free energy calculations²²⁾ and the details are given in APPENDIX with related discussions. It is found that the introduction of J' causes significant modifications in the spin structure. Five phases are shown in Fig.8 (a) and the corresponding models of the spin structures are given in Fig.9 where large arrows and small ones represent the direction of spins on two adjacent triangular planes of hcp lattice. Only the case $J' > 0$ is shown. One can obtain the structure for $J' < 0$ simply by reversing all the small arrows of Fig.9.

Phase I is a ferromagnetic state and phase II is a simple antiferromagnetic state. Phase V is a helical structure. On the other hand, the Δ -state, where spins are rotating by 120° , is only stable on the J_1 axis above $J_1 = J_0/8$ and is modified into two incommensurate structures III and IV by J' . However, the modification is found to be negligible when $J_1 > 0$ and J' is small. When $J_0 > 0$, there is one helical structure (phase V') in addition to the ferromagnetic state.

It is easily verified that the case $J_0 > 0$ can not explain the metamagnetic plateau, because the FI-state becomes higher in the energy than the ferromagnetic state. Therefore, we concentrate our attention to the case $J_0 < 0$. Furthermore, we can conclude $3J_0 + 2|J'| < 0$, or otherwise the energy of FI-state

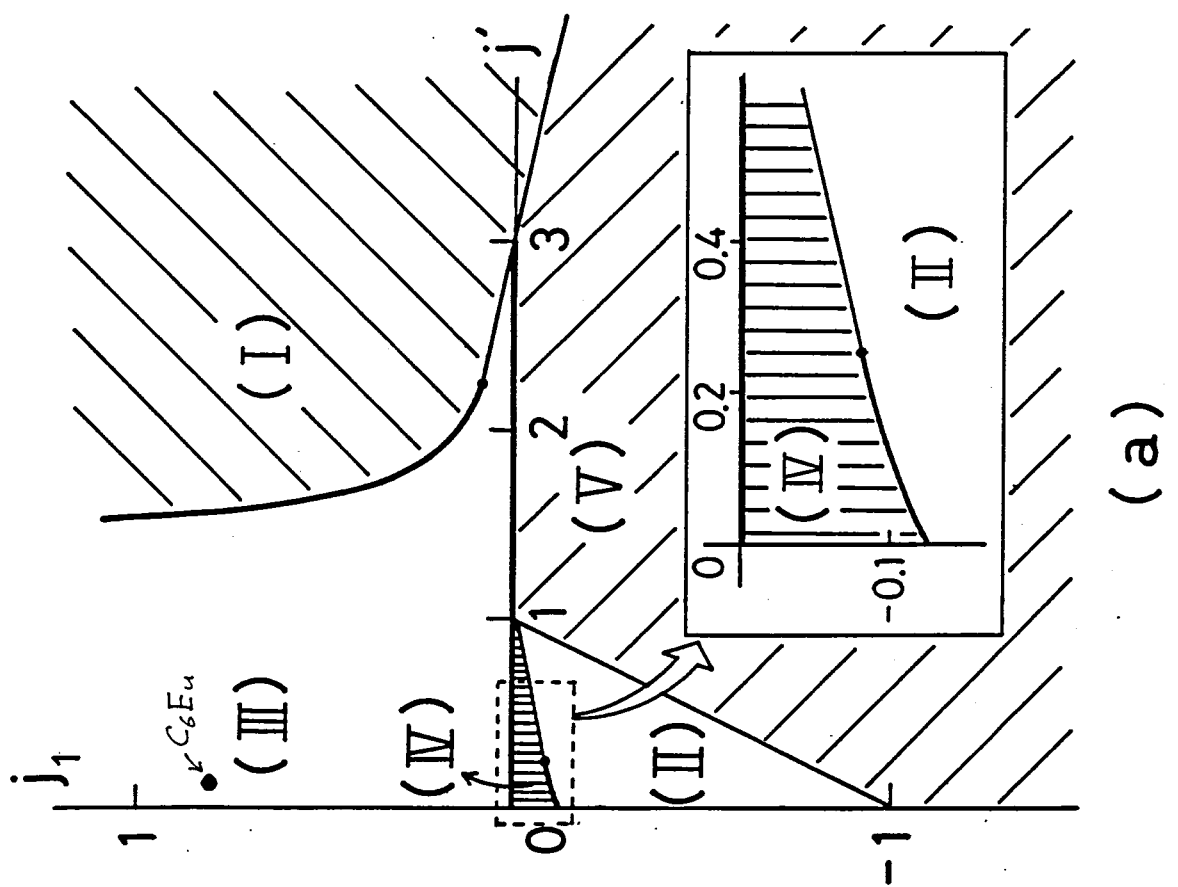
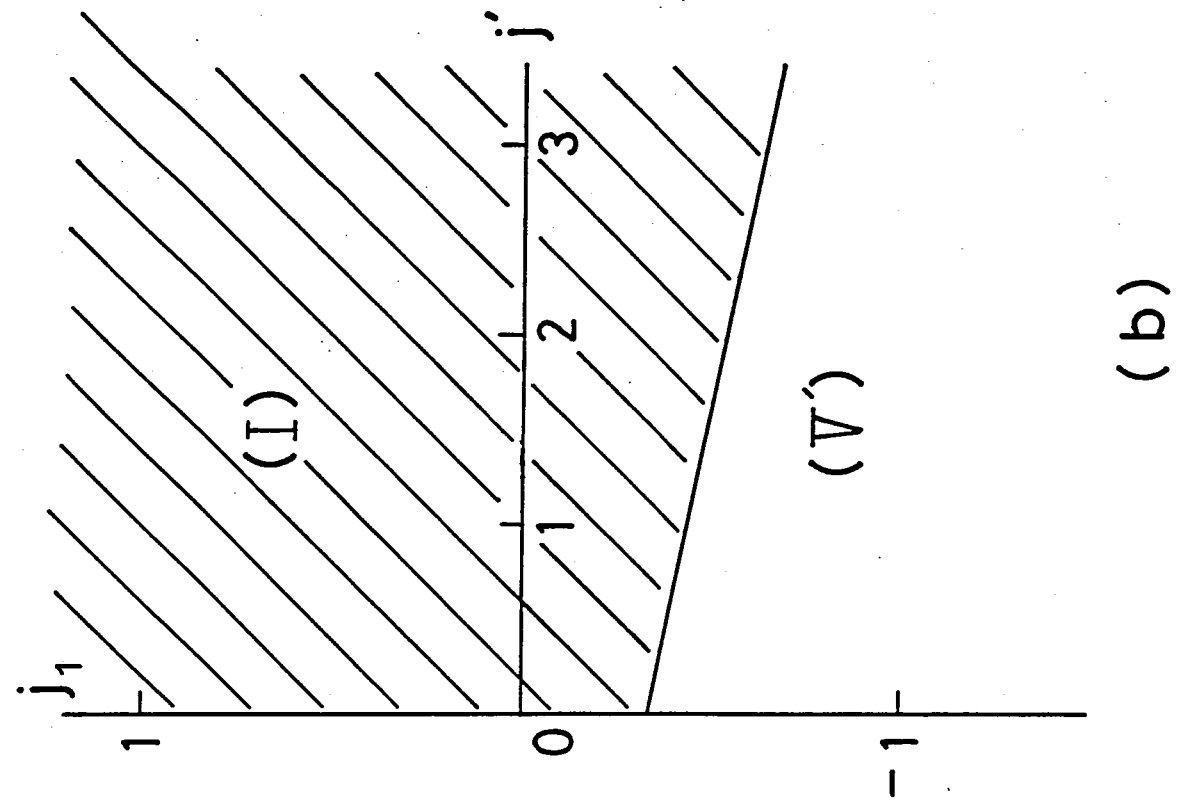


Fig. 8 Phase diagrams of hcp lattice for $J_0 < 0$ (a) and $J_0 > 0$ (b).
 $j_1 = J_1 / |J_0|$, $j' = |J'| / |J_0|$. Thick solid lines indicate the first order phase boundaries, and the others are the second order boundaries.

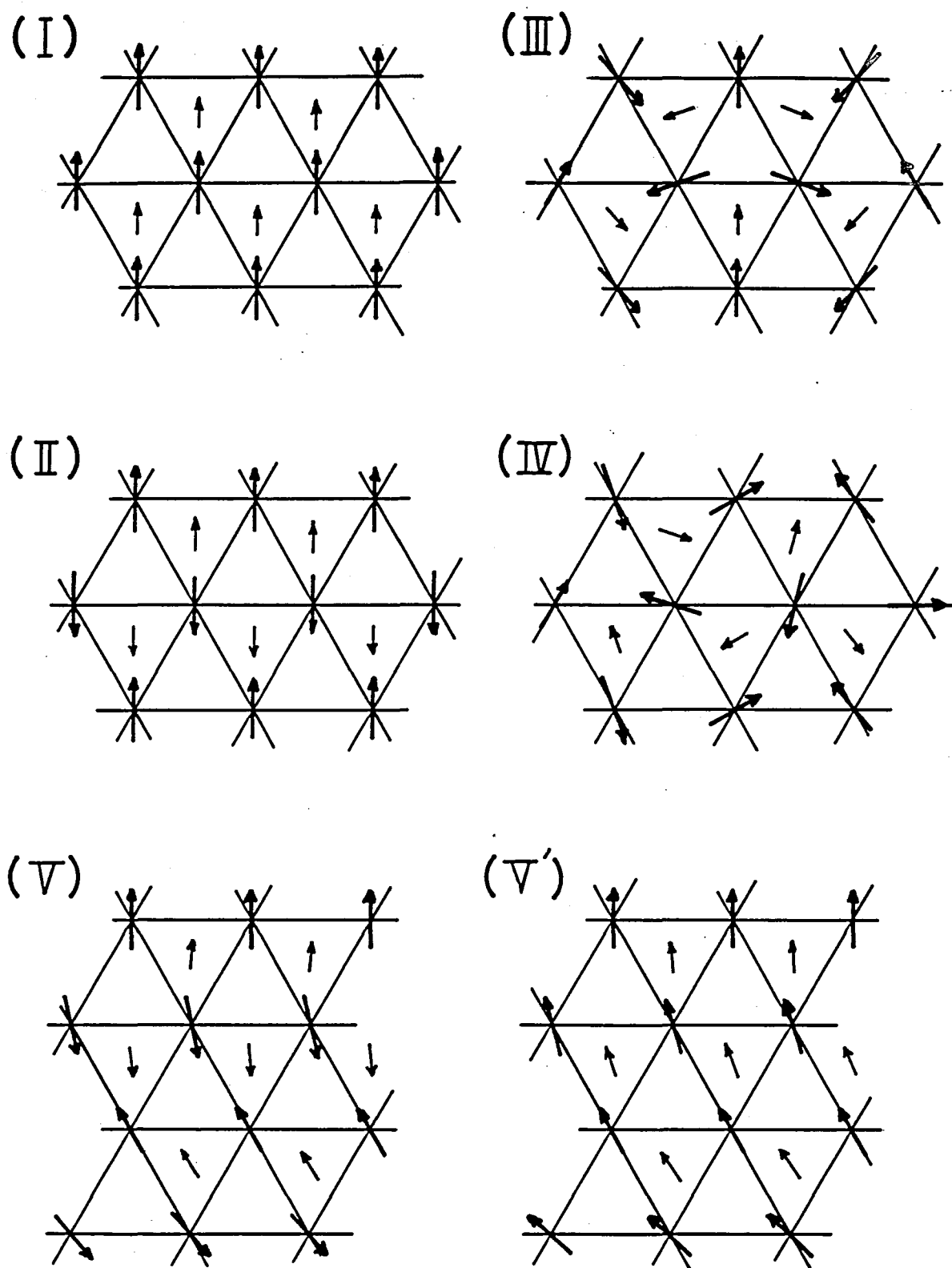


Fig.9 Models of spin structures of corresponding phases shown in Fig.8. Small arrows indicate the direction of spins on the adjacent plane.

again becomes higher than that of the ferromagnetic state.

There seems to be still many possibilities for the ground state of C_6Eu in the phase diagram. However, we can prove that the ferrimagnetic plateau can not appear in the magnetization process no matter what the ground state may be.

We consider the Δ - and FI-state again. The corresponding free energies are given by the same formulas as (2) and (3) except $\lambda = -6(3J_0 + 2J')/Ng^2\mu_B^2$, instead of $\lambda = -18J_0/Ng^2\mu_B^2$. Then the same argument holds as before and the ferrimagnetic plateau can not appear because Δ -state is always lower in the energy. Furthermore, the above argument can easily be generalized for the case where there exist long range exchange interactions as may be expected in the RKKY-interaction system. As can be seen from Fig.5, rows of three sublattice align as $\cdots \vec{M}_1, \vec{M}_2, \vec{M}_3, \vec{M}_1, \vec{M}_2, \vec{M}_3 \cdots$ along c-plane. Consider one of \vec{M}_1 rows. The alignment of \vec{M}_2 rows on the right hand of the \vec{M}_1 row is exactly symmetric with that of \vec{M}_3 rows on the left side. Therefore, the number of both inter and intraplane n-th nearest neighbour \vec{M}_2 -sites around each \vec{M}_1 site is exactly the same as that of \vec{M}_3 -sites. Thus, the molecular field coefficient of exchange interaction $\vec{M}_1 \vec{M}_2$ is the same as that of $\vec{M}_1 \vec{M}_3$. In the same way, it can be shown that the molecular field coefficients for $\vec{M}_2 \vec{M}_3$ and $\vec{M}_1 \vec{M}_2$ are the same. Therefore, the free energy of the three sublattice model can always be written in the form of eq.(1). Then, the relation between Δ - and FI-state does not change, how far the exchanges

are taken into account.

To realize the experimentally observed metamagnetic plateau, the energy crossing between Δ - and FI-states must occur at the field below H_{c1} . However, the preceding discussion concludes that it can not occur within the usual two-spin exchange. Another effect that should be discussed here may be the magnetic anisotropy of the system. First, dipolar interaction is considered. Taking into account the dipolar energies in the free energies (5) and (8), the triangular to ferrimagnetic transition will occur at $H_0 = \lambda M - \sqrt{2\lambda E_d}$, where E_d is the dipolar anisotropy energy. As the effect of E_d is enhanced by the exchange interaction λ , careful estimation of E_d is necessary. We obtained the dipolar sum on the three sublattice model and found that the dominant dipolar interaction from neighbouring spins on the same plane is isotropic and can be reduced in the free energy (1). The anisotropy E_d arises from the spins on the adjacent plane, and E_d/k_B is obtained as 0.06N K. The value is, however, too small to account the experiment. It is only to modify the crossing field by ~ 9 kOe. Dipole incommensurate structure⁴⁾ may be possible in this compound near T_N , but it will not explain the present experiments performed at well low temperature. Hexagonal in-plane anisotropy should also be considered. The magnetization process of helical spin state with in-plane hexagonal anisotropy was discussed in detail by Nagamiya²²⁾, who revealed the successive phase transitions helical \rightarrow fan \rightarrow ferro with discontinuous change in the

magnetization. However, the ferrimagnetic plateau observed in the present experiment can not be explained by the model. No angular dependence in the c-plane is found in the experiment.

Considering these facts, we can conclude this section as follows: there should be some interactions in the system which stabilize the ferrimagnetic state, but they are not the usual two-spin exchanges nor the anisotropies. The possible candidates will be the four-spin exchange interactions which is discussed in the next section.

§5. EFFECTS OF FOUR-SPIN EXCHANGE INTERACTIONS

The difficulty discussed in the preceding section can be removed by introducing four-spin exchange interactions. We take into account the biquadratic exchange and four-spin cyclic exchange in addition to J_0 , J_1 and J' , as have been done in NiS_2 problem^{12~14)}. The recent applications of the four-spin exchange are given by Yosida²³⁾. The present paper follows his notations and treatment except for the field dependence, which is first treated by us⁹⁾.

The biquadratic exchange energy for spins S_i and S_j is given by

$$U_B = -B(\vec{S}_i \vec{S}_j)^2, \quad B > 0. \quad (9)$$

The four-spin cyclic exchange energy for spins S_i , S_j , S_k and S_l is expressed as

$$U_K = K[(\vec{S}_i \vec{S}_j)(\vec{S}_k \vec{S}_l) + (\vec{S}_i \vec{S}_l)(\vec{S}_k \vec{S}_j) - (\vec{S}_i \vec{S}_k)(\vec{S}_j \vec{S}_l)], \quad K > 0, \quad (10)$$

where we consider only the dominant nearest neighbour cyclic exchange for K . It is noted that sign of K is usually positive¹²⁾ but that of B depends on materials. We assume that it is positive in C_6Eu in accord with the experimental facts.

We first discuss the magnetization process when the magnetic field H_0 is applied along c-plane. In this case all the spins are parallel to c-plane so that eq.(10) can be written in the form as²³⁾

$$U_K = KS^4 \cos(\phi_i - \phi_j + \phi_k - \phi_l), \quad (11)$$

where ϕ_i , ϕ_j , ϕ_k and ϕ_l represent angles between H_0 and each spin. In our three sublattice model, any nearest neighbour exchange path (i,j,k,l) can be reduced to four rings $r_1 \sim r_4$ shown in Fig.10. The calculations of $\cos(\phi_i - \phi_j + \phi_k - \phi_l)$ terms in these rings are listed in Fig.11. Consider, for example, one spin in the \vec{M}_1 -sublattice in Fig.10 (a). The number of rings to be taken into account is 12, 6 for r_1 and 6 for r_2 . The four-spin energies can be calculated by eq.(11), making use of Fig.11, as $KS^4 \cos 3\alpha$ and KS^4 for r_1 and r_2 , respectively, where the notation of the angle defined in Fig.6 is used. Therefore, the total four-spin energy for one \vec{M}_1 -site is expressed as $6KS^4(1+\cos 3\alpha)$. Summing up for all sites in same manner, the four-spin energy for Δ -state is obtained as

$$U_{\Delta K} = KNS^4(1+2\cos 3\alpha). \quad (12)$$

Similarly, the four-spin energy for FI-state is given by

$$U_{FIK} = KNS^4(\cos 2\beta + 2\cos \beta). \quad (13)$$

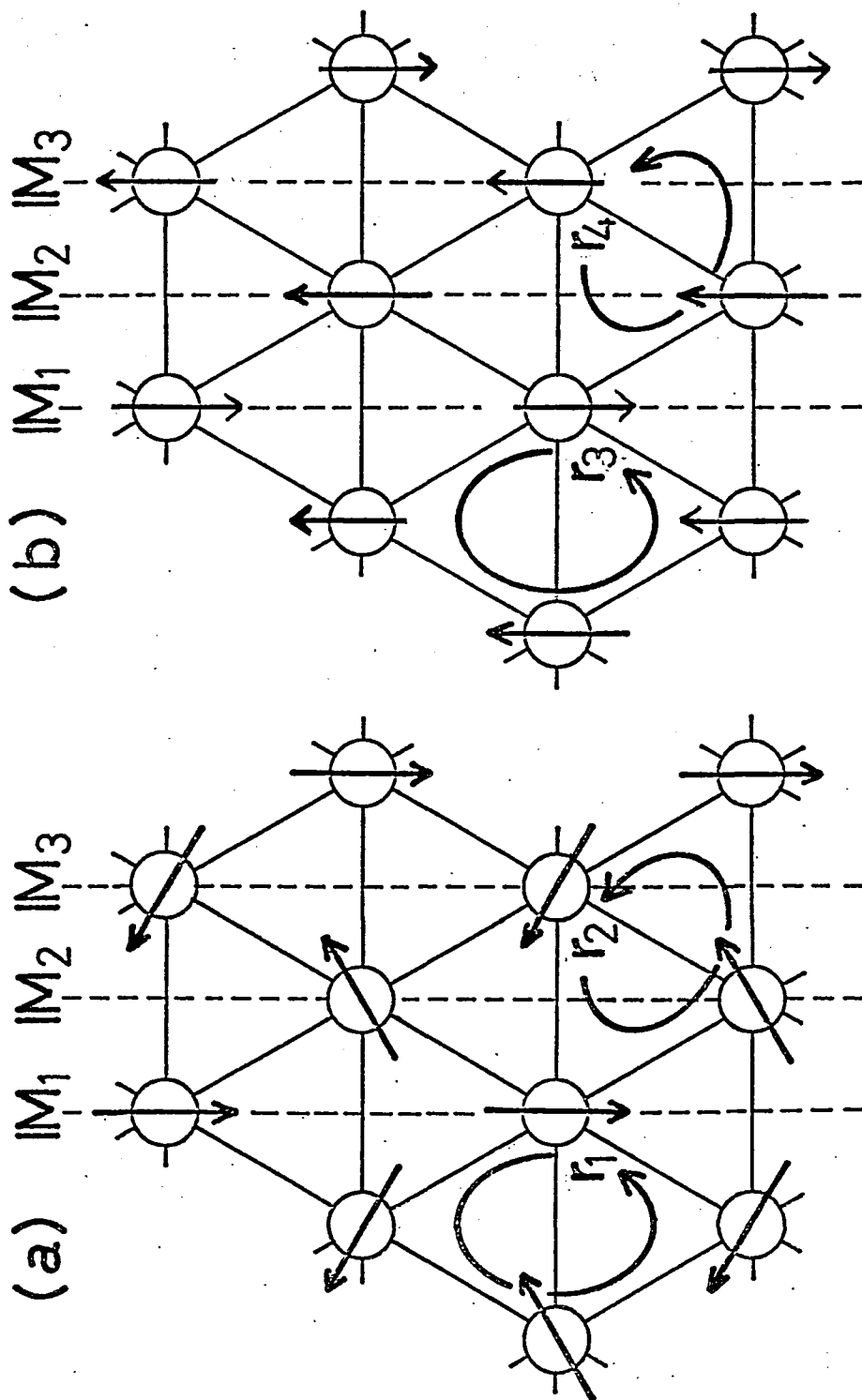
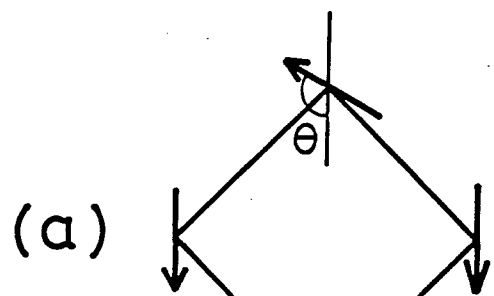
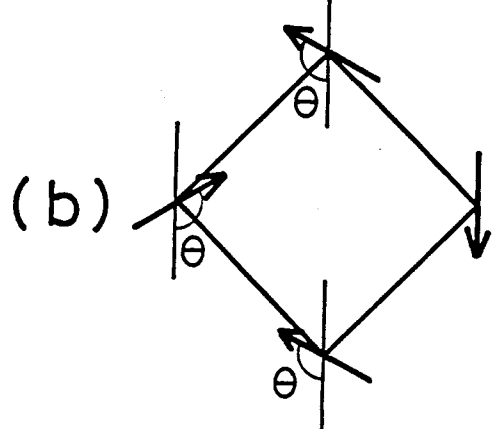


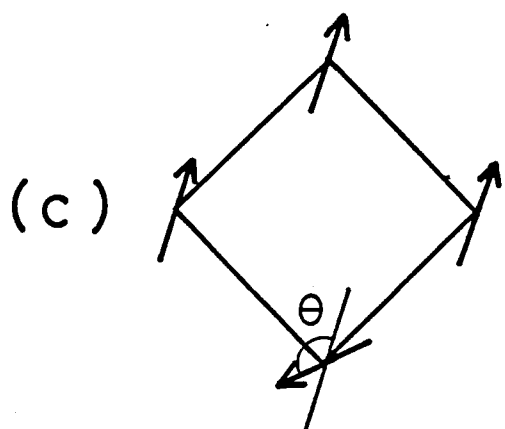
Fig.10 Four-spin nearest neighbour exchange paths for Δ -state(a) and
FI-state(b), indicated by arrows $r_1 \sim r_4$.



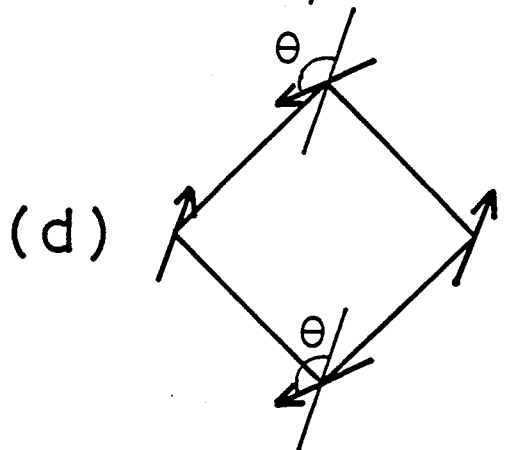
K



$K \cos 3\theta$



$K \cos \theta$



$K \cos 2\theta$

Fig.11 Four-spin ring diagrams and the corresponding energies.

The free energies of biquadratic terms for Δ -state ($U_{\Delta B}$) and FI-state ($U_{FI B}$) are easily obtained as

$$U_{\Delta B} = -BNS^4(\cos^2 2\alpha + 2\cos^2 \alpha), \quad (14)$$

$$U_{FI B} = -BNS^4(1 + 2\cos^2 \beta). \quad (15)$$

The contribution of the four-spin energies (12)~(15) to the magnetization processes of Δ - and FI-state are given in Fig.12. It is easily found that the four-spin energies can stabilize the FI-state against Δ -state below H_{c1} . Therefore, the energy crossing between Δ - and FI-state can occur below H_{c1} . It is noted that the four-spin energy of the configuration given in Fig.6 (b) is found to be higher than that of Fig.6(a), so that we need not consider it.

From eqs. (12)~(15) in addition to (2) and (3), the total free energies of Δ -state and FI-state up to fourth order in S are written as

$$\begin{aligned} U_{4\Delta} = & (1 + 2\cos\alpha)MH_0 + (2\cos\alpha + \cos 2\alpha)MH_E \\ & - (\cos^2 2\alpha + 2\cos^2 \alpha)MH_B + (1 + 2\cos 3\alpha)MH_K, \end{aligned} \quad (16)$$

$$\begin{aligned} U_{4FI} = & -(2\cos\beta_1 + \cos\beta_2)MH_0 + (1 + 2\cos\beta)MH_E \\ & - (1 + 2\cos^2 \beta)MH_B + (\cos 2\beta + 2\cos\beta)MH_K, \end{aligned} \quad (17)$$

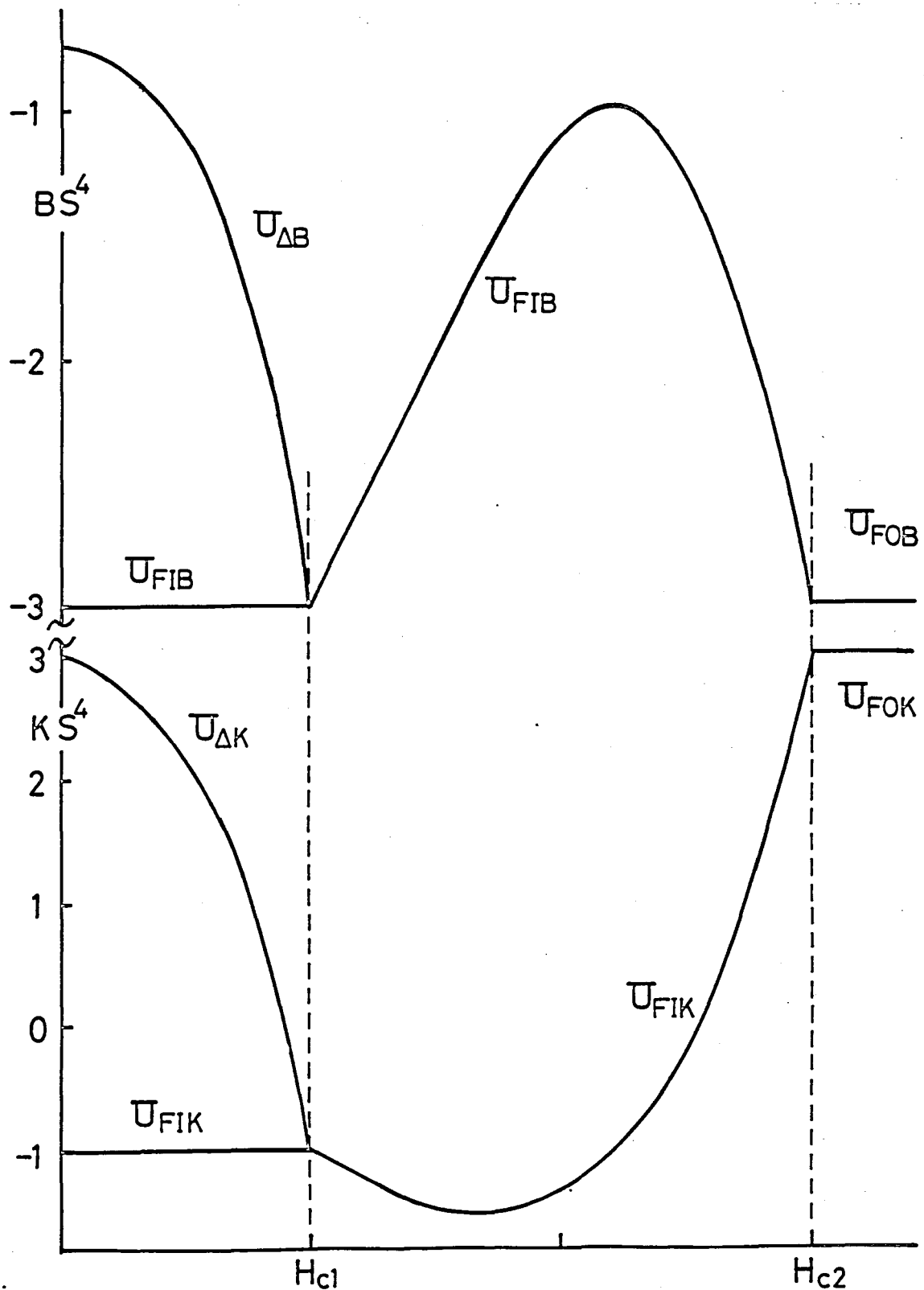


Fig.12 Four-spin free energies as a function of magnetic field. The suffixes Δ , FI and FO corresponds to the triangular, ferri-magnetic and ferromagnetic states, respectively, and B and K mean the biquadratic and four-spin-cyclic exchange, respectively.

where three effective fields are defined as $H_E = \lambda M$, $H_B = 3BS^3/g\mu_B$ and $H_K = 3KS^3/g\mu_B$. Neglecting the change in the initial susceptibility of Δ -state caused by the higher order terms, the critical field H_{c0} , where the spin-triangular to ferrimagnetic transition occurs, is previously calculated as⁹⁾

$$H_{c0} = H_E - 2[H_E(H_B' + H_K')]^{1/2}, \quad (18)$$

with

$$H_B' = (1 - \cos^2 \alpha_0 \cos 2\alpha_0) H_B, \quad (19)$$

$$H_K' = (1 + \cos^2 3\alpha_0) H_K, \quad (20)$$

where α_0 is the angle α at H_{c0} and expressed as

$$\cos \alpha_0 = -(1/2)(1 + H_{c0}/H_E). \quad (21)$$

When the change in the susceptibility of Δ -state is taken into account, the critical field H_{c0} given by eq.(18) will be modified. We shall treat the initial stage of the magnetization of Δ -state more exactly. The magnetization process can be obtained by minimizing the energy (16) with respect to angles and is given by

$$H_0 = m[H_E - H_B(m+1)(m+2) - 3H_K(m+2)], \quad (0 \leq m \leq 1), \quad (22)$$

where $m = -(1 + 2\cos \alpha)$ is the magnetization value in reduced unit.

It is noted that the ferrimagnetic state corresponds to the case $m=1$. When $12H_K + 11H_B < H_E$, eq.(22) gives only one solution for m . In this case, m continuously increases with H_0 and shows second order phase transition to the ferrimagnetic state($m=1$) at the critical field

$$H_{c0} = H_E - 6H_B - 9H_K, \quad (23)$$

which is a little different from the previous expression of the critical field (18). On the other hand, when $12H_K + 11H_B > H_E$, m in eq.(22) has two solutions so that one should compare the free energies with that of the ferrimagnetic state and take the stable one. Two cases are found. If $8H_K + \frac{9}{2}H_B < H_E$, the system shows first order phase transition to the ferrimagnetic state at a field which can not be written in a simple form but is somewhat larger than the value given by eq.(23). The other case, when $8H_K + \frac{9}{2}H_B > H_E$, the ferrimagnetic state becomes stable even at $H_0 = 0$. In our case of C_6Eu , H_K and H_B are considered to be small compared with H_E so that the critical field (23) may be applied approximately.

Numerical results of the magnetization of Δ -state are shown in Fig.13 for three typical cases. In the figure, the reduced magnetization m is given as a function of the external field scaled by H_E . Curve (1) is an example that shows second order transition to the ferrimagnetic($m=1$) state. Curve (3) is an

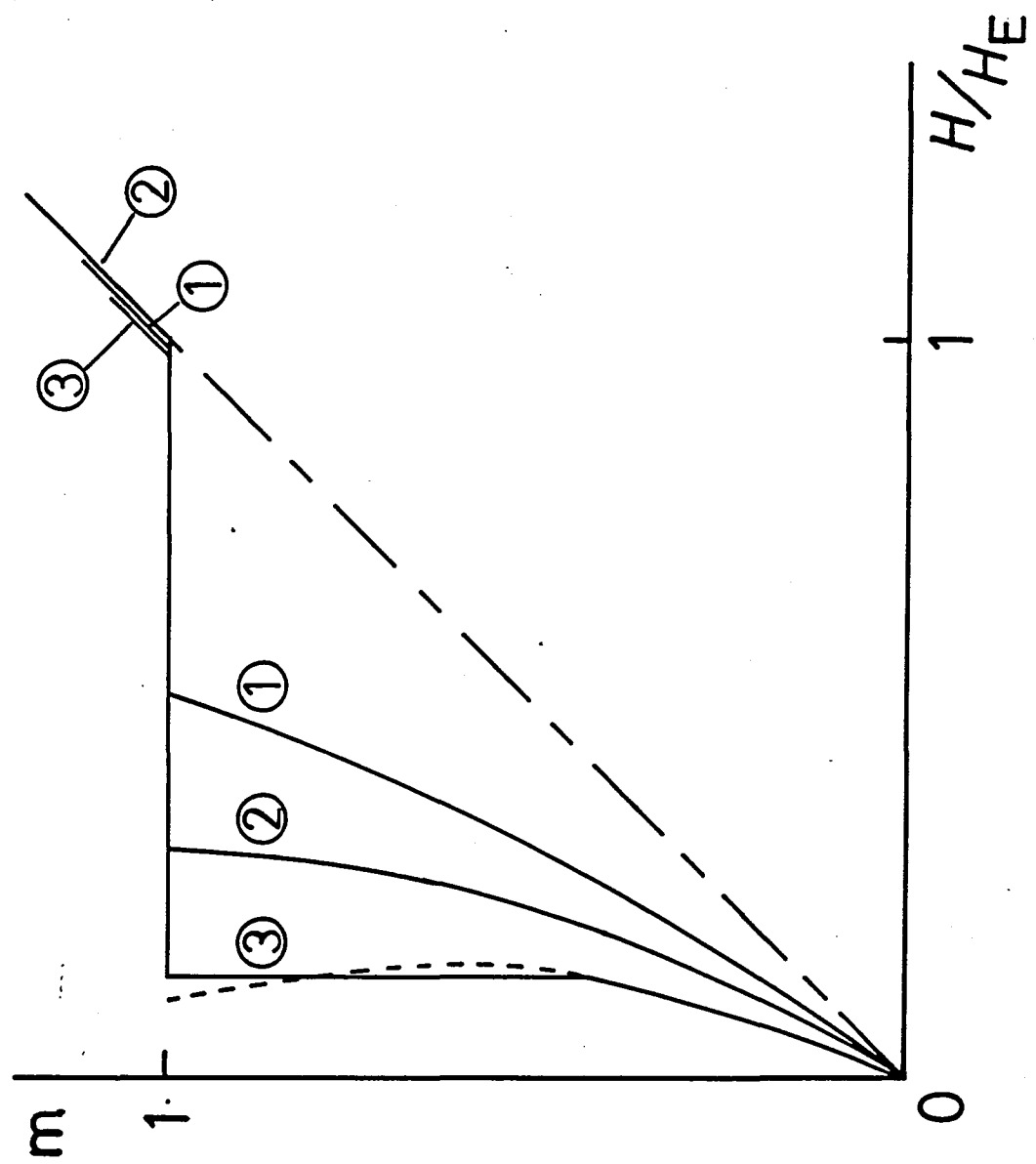


Fig.13 Initial stage of the magnetization process(H_0 in c-plane) calculated for three cases: (1) $H_B/H_E=0.02$, $H_K/H_E=0.04$; (2) $H_B/H_E=0.025$, $H_K/H_E=0.06$; (3) $H_B/H_E=0.03$, $H_K/H_E=0.08$. Dot-dashed line is the case $H_B=H_K=0$. Dotted line denotes thermodynamically unstable state.

example which shows first order transition, where dotted line shows the thermodynamically unstable solution derived from eq.(22). Curve (2) is at a critical condition and $C_6\text{Eu}$ is found to be near this case. Dot-dashed line in the figure shows the magnetization process when there is no four-spin exchange interaction. It is noted that the four-spin terms can reduce H_{c0} significantly without changing H_{cl} widely. Critical fields H_{cl} and H_{c2} are similarly given in terms of H_K and H_B as

$$H_{cl} = H_E + 2H_B - H_K, \quad (24)$$

$$H_{c2} = 3(H_E - 2H_B + 3H_K). \quad (25)$$

We can compare the three critical fields (23)~(25) with the experimentally obtained values $H_{c0}=16$ kOe, $H_{cl}=64$ kOe and $H_{c2}=215$ kOe, and determin H_E , H_B and H_K . The results are

$$\left. \begin{array}{l} H_E = 64 \text{ kOe}, \\ H_B = 2.0 \text{ kOe}, \\ H_K = 4.0 \text{ kOe.} \end{array} \right\} \quad (26)$$

These values are slightly different from the previously determined values $H_E=65$ kOe, $H_B=1.6$ kOe and $H_K=3.9$ kOe, which are derived from the expression of the critical field H_{c0} of eq.(18).

Three exchange parameters J_0 , J_1 and J' are determined from the exchange field H_E and the Curie-Weiss constant θ .

These are expressed as

$$H_E = -2(3J_0 + 2J')S/g\mu_B = 64 \text{ kOe}, \quad (27)$$

$$\theta = 63(J_0 + J_1 + J')/k_B = 1.3 \text{ K}, \quad (28)$$

where k_B is the Boltzmann constant. Using eqs.(27) and (28) with reasonable assumptions $J_1 < |J_0|$ and $|J'| \ll |J_0|$, the exchange parameters are determined as

$$\left. \begin{array}{l} J_0/k_B = -0.5 \pm 0.1 \text{ K}, \\ J_1/k_B = 0.4 \pm 0.1 \text{ K}, \\ J'/k_B = 0.1 \pm 0.1 \text{ K.} \end{array} \right\} \quad (29)$$

These values correspond to the point indicated in the phase diagram of Fig.8 (a). This results confirms the initial assumption that the ground state of C_6Eu is the spin triangular state. It is also noted that J_1 is nearly comparable to J_0 , with the opposite sign. This is consistent with the model that the dominant exchange in the c-plane is the RKKY interaction.

The four-spin exchange parameters are given in the next page.

$$BS^2/k_B = 0.02 \pm 0.005 \text{ K}, \quad (30)$$

$$KS^2/k_B = 0.05 \pm 0.01 \text{ K}. \quad (31)$$

The results show that the four-spin ring exchange is larger than the biquadratic exchange in accord with the case of $\text{NiS}_2^{14})$.

It is emphasized that $C_6\text{Eu}$ is the first example in which the four-spin exchanges are determined quantitatively. In ^3He (bcc) and NiS_2 (fcc), the exchange paths are complex and it is difficult to determin the value. In the triangular plane, on the other hand, the basic four-spin cyclic path is only one rhombic route and this simplifies the problem great deal. From the obtained parameters, the magnetization curve for $H_0 \parallel c$ -plane is drawn by solid line in Fig.14. The experimental result is also shown in the figure by dashed line, which shows a satisfactory agreement with the theory.

Next, we consider the magnetization process for $H_0 \parallel c$ -axis. Experimentally speaking, no metamagnetic plateau is observed in this case and the magnetization shows nearly linear increase. This will be explained by introducing, for example, weak uniaxial anisotropy of the form DS_z^2 , $D > 0$, along c -axis. The assumption of such term is consistent with the observed anisotropic behaviour of the magnetic susceptibility. When the anisotropy exists, the Δ -state will take the configuration given in Fig.15 (a) under the field H_0 applied along c -axis. In this case, spins are not in the same plane so that the

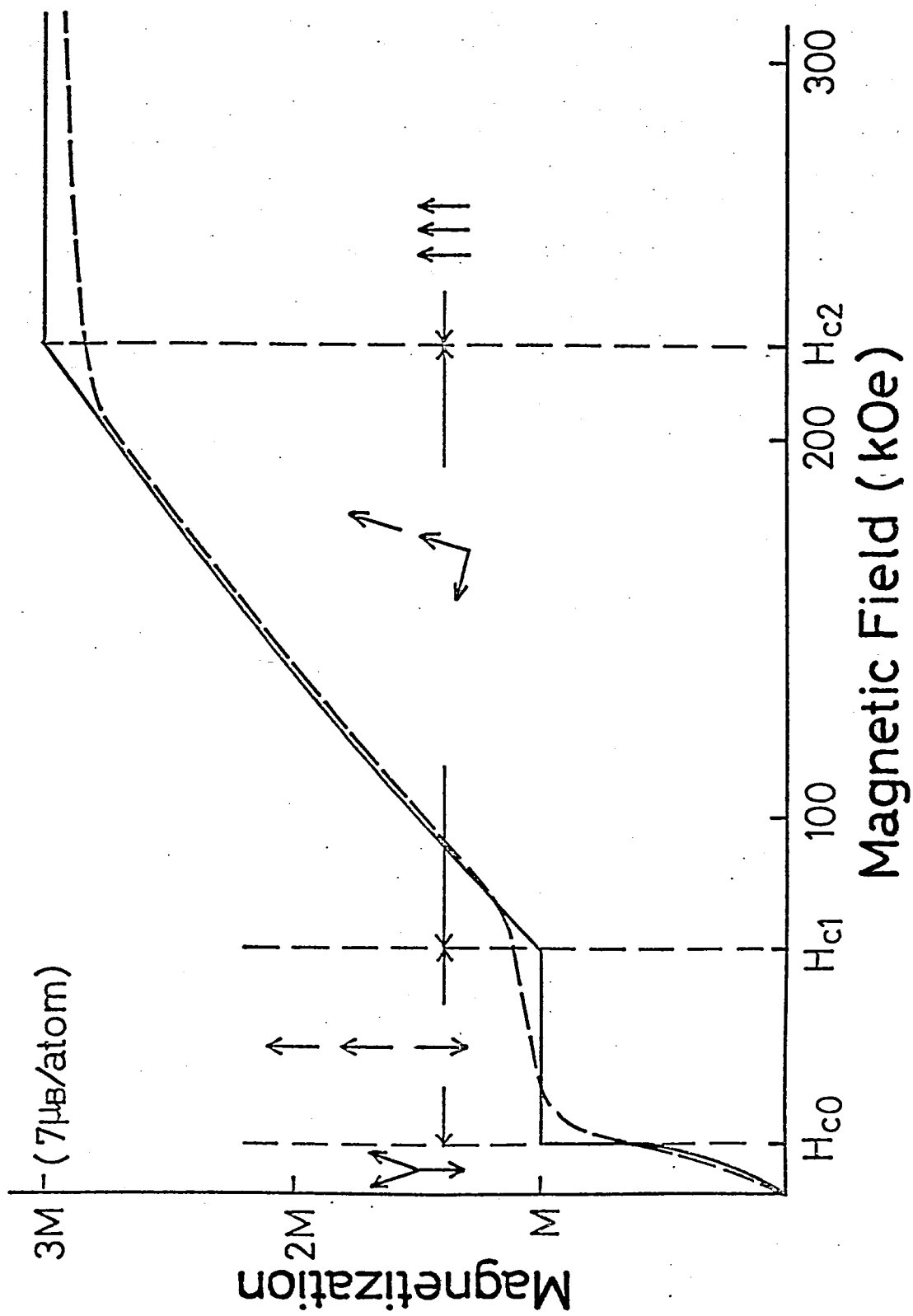


Fig. 14 Theoretical magnetization curve of C_6Eu , $H_0//c$ -plane. Dashed line is the experimental result. Models of spin structures are shown.

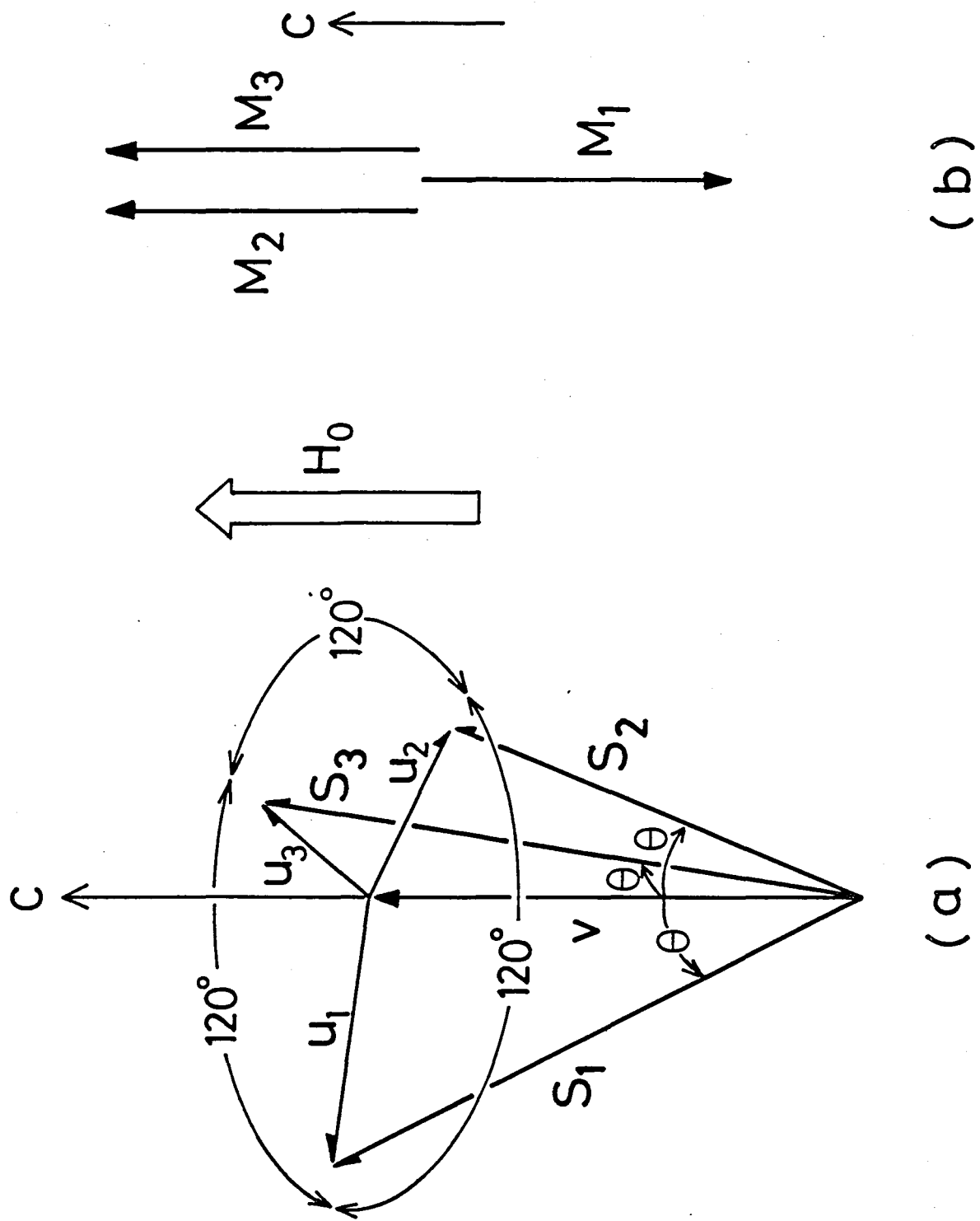


Fig.15 Model of magnetization process for $H_0//c$ -axis. (a):triangular state; (b):ferrimagnetic state.

four-spin energy formula (11) can not be applied. We divide \vec{S}_i into two components, \vec{u}_i and \vec{v} :

$$\vec{S}_i = \vec{u}_i + \vec{v}, \quad |\vec{u}_i| = S \sin \theta, \quad |\vec{v}| = S \cos \theta, \quad (32)$$

where angle θ is defined in Fig.15 (a). Vector \vec{u}_i is perpendicular to c-axis and forms the triangular configuration, while \vec{v} is parallel to c-axis. Substituting (32) into (10), the four-spin-ring energy is written as

$$\begin{aligned} U_K' = & K [(\vec{u}_i \vec{u}_j) (\vec{u}_k \vec{u}_l) + (\vec{u}_i \vec{u}_l) (\vec{u}_j \vec{u}_k) - (\vec{u}_i \vec{u}_k) (\vec{u}_j \vec{u}_l) \\ & + v^2 (\vec{u}_i \vec{u}_j + \vec{u}_j \vec{u}_k + \vec{u}_k \vec{u}_l + \vec{u}_l \vec{u}_i - \vec{u}_i \vec{u}_k - \vec{u}_j \vec{u}_l) \\ & + v^4] . \end{aligned} \quad (33)$$

As $\vec{u}_i \sim \vec{u}_l$ lie on the same plane, the first three terms in the bracket can be written in the form of eq.(11) and given as $S^4 \sin^4 \theta \cos(\phi_i - \phi_j + \phi_k - \phi_l)$, where ϕ_i is the angle between \vec{u}_i and arbitrary chosen axis in c-plane. The value of $\cos(\phi_i - \phi_j + \phi_k - \phi_l)$ is again obtained from Fig.11 and is now unity for all rings because \vec{u}_i 's remain in 120° -triangular state throughout the magnetization process. The fourth term $(\vec{u}_i \vec{u}_j + \vec{u}_j \vec{u}_k + \vec{u}_k \vec{u}_l + \vec{u}_l \vec{u}_i - \vec{u}_i \vec{u}_k - \vec{u}_j \vec{u}_l)$ also gives the same value $-(5/2)S^2 \sin^2 \theta$ for all rings. Thus the four-spin free energy of Δ -state for $H_0 \parallel c$ -axis is written as in the next page.

$$U_{\Delta K}' = \frac{3}{2} N K S^4 (2 - 9 \cos^2 \theta + 9 \cos^4 \theta). \quad (34)$$

Adding Zeeman, two-spin, biquadratic and anisotropy terms to eq.(34), the total free energy $U_{4\Delta}'$ up to fourth order in S is written as

$$U_{4\Delta}' = -3M H_0 \cos \theta - \frac{3}{2} M H_E (1 - 3 \cos^2 \theta) - \frac{3}{4} M H_B (1 - 3 \cos^2 \theta)^2 + \frac{3}{2} M H_K (2 - 9 \cos^2 \theta + 9 \cos^4 \theta) + 3M H_D \cos^2 \theta, \quad (35)$$

where $H_D = DS/gu_B$. The above energy should be compared with that of the ferrimagnetic state perpendicular to c-plane (Fig. 15 (b)). The energy can be obtained by adding the anisotropy energy $3M H_D$ to eq.(17), putting the angles as $\beta_1 = 0$, $\beta_2 = \beta = 180^\circ$, and the result is

$$U_{4FI}' = -M H_0 - M H_E - 3M H_B - M H_K + 3M H_D. \quad (36)$$

The 1/3 ferrimagnetic plateau will not appear if the relation $U_{4\Delta}' < U_{4FI}'$ holds at $H_0 = H_{c1}$, or $\cos \theta = 1/3$. From (35) and (36), we obtain the following condition for H_D :

$$H_D > H_B + H_K. \quad (37)$$

From previously obtained values of H_B and H_K , it is concluded that H_D of 6 kOe or D of 0.23 K is enough to suppress the ferrimagnetic state in c-axis magnetization process.

Finding the minimum condition of eq.(35) with respect to θ , the magnetization curve for $H_0 \parallel c$ -axis can be obtained and is given in Fig.16 by solid line. The magnetization increases sublinearly with the field and saturates at around 240 kOe, which is a little higher than the case $H_0 \parallel c$ -plane due to the anisotropy. Dashed line in the figure denotes the experimental result. A qualitative agreement is obtained. The difference between the theory and the experiment may be due to the diamagnetic eddy current induced in the conductive c -plane by the pulsed magnetic field.

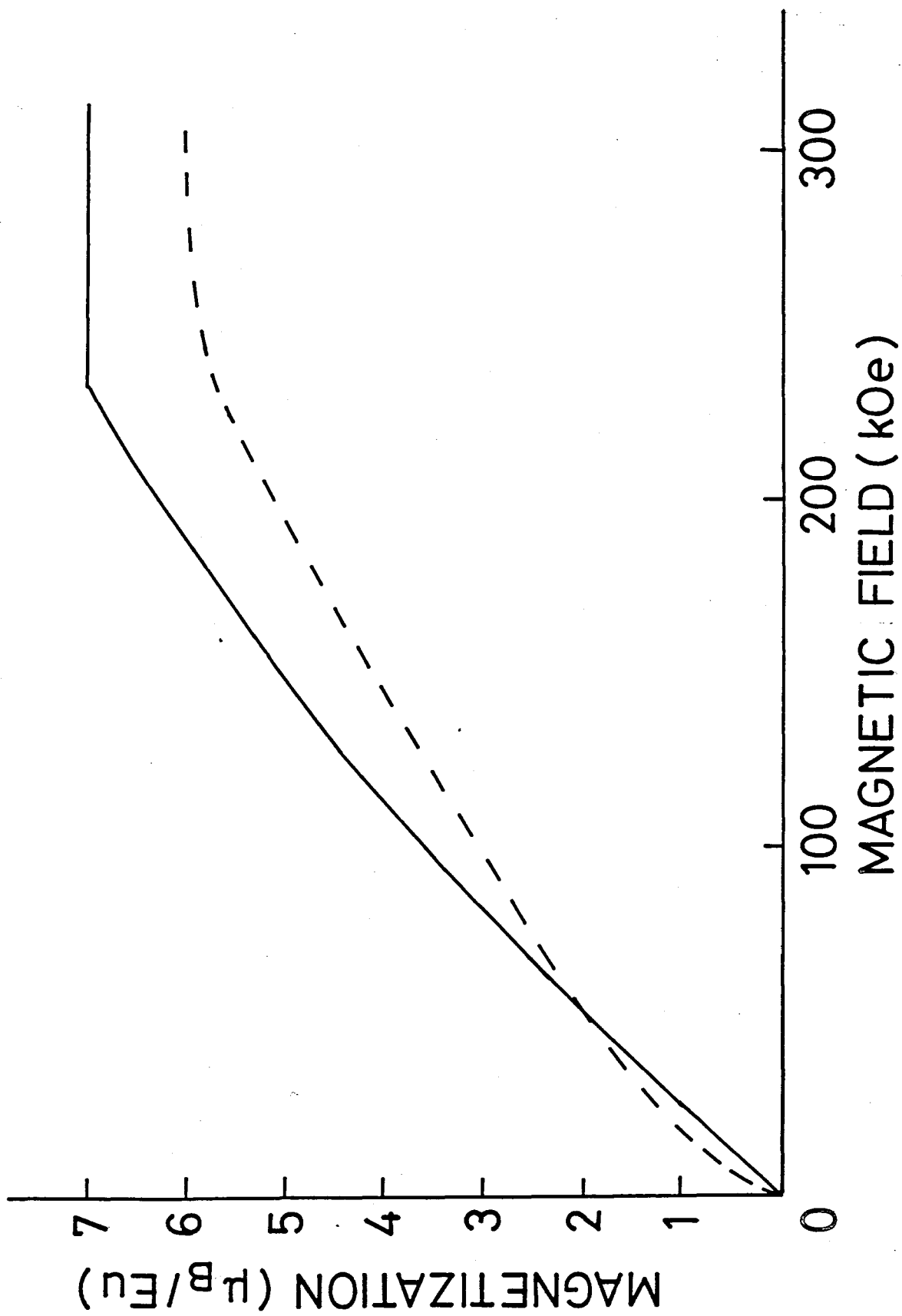


Fig.16 Theoretical magnetization curve of C_6Eu for $H_0//c$ -axis (solid line)
 Dashed line is the experimental result.

§ 6. PHENOMENOLOGICAL CONSIDERATION

So far, we have taken into account only biquadratic and nearest neighbour cyclic four-spin exchange interactions in the four-spin free energy. There may be another paths for four-spin exchange, or another higher order term such as three-spin exchange of the form $(\vec{S}_i \vec{S}_j)(\vec{S}_k \vec{S}_j)$. To consider the effect of these terms, a phenomenological treatment is also done.

As discussed in §4, three sublattices \vec{M}_1 , \vec{M}_2 and \vec{M}_3 are interacting equivalently to each other in triangular lattice. Therefore, the general form of the free energy of the three sublattice model up to fourth order in M should be written as

$$\begin{aligned}
 U_4 = & -\vec{H}_0(\vec{M}_1 + \vec{M}_2 + \vec{M}_3) + \lambda'(\vec{M}_1 \vec{M}_2 + \vec{M}_2 \vec{M}_3 + \vec{M}_3 \vec{M}_1) \\
 & - B'[(\vec{M}_1 \vec{M}_2)^2 + (\vec{M}_2 \vec{M}_3)^2 + (\vec{M}_3 \vec{M}_1)^2] \\
 & + K'[(\vec{M}_1 \vec{M}_2)(\vec{M}_2 \vec{M}_3) + (\vec{M}_2 \vec{M}_3)(\vec{M}_3 \vec{M}_1) + (\vec{M}_3 \vec{M}_1)(\vec{M}_1 \vec{M}_2)]. \quad (38)
 \end{aligned}$$

Other terms such as M_i^4 or $M_i^2 M_j^2$ are constant and terms such as $M_i^2 (\vec{M}_j \vec{M}_k)$ can be reduced to the quadratic term, at least at $T=0$. In the above expression, biquadratic exchange B contributes to B' term and four-spin cyclic exchange K considered in the last section has contribution to both λ' and K' . Any other interactions can be reduced to λ' , B' and K' . In last section, we had taken into account only B and K terms in addition

to λ and discussed the free energy. In that case, the free energy can be written in the general form with the relations

$$\lambda' M = H_E - H_K, \quad (39)$$

$$B' M^3 = H_B, \quad (40)$$

$$K' M^3 = 2H_K. \quad (41)$$

It is noted that B' and K' terms contain only B and K terms respectively. We have chosen H_E , H_B and H_K so as to explain the experimental results. This means that the general molecular field coefficients λ' , B' and K' are adjusted through H_E , H_B and H_K . Therefore, H_E , H_B and H_K obtained in the preceding section should be considered as effective exchange fields that contain all the higher order interactions.

§ 7. CONCLUDING DISCUSSION

In this paper we have measured the high field magnetization of easy plane triangular lattice antiferromagnet C_6Eu and found a ferrimagnetic plateau in the c-plane magnetization process. We have discussed the magnetization process within the molecular field theory and found that the plateau can not be explained by usual two-spin exchange or anisotropy, but can be well explained by introducing a weak four-spin exchange interactions in the system. The four-spin exchange energy is about 10 % of the nearest neighbour two-spin exchange J_0 . However, the ratio B/J_0 and K/J_0 are 0.4 % and 0.9 %, respectively, and are very small. These results are acceptable because the system is considered to be governed by RKKY-interaction between well localized Eu spins. As the spin value is very large ($S=7/2$), these weak higher order interactions could affect the magnetization process. It is noted that the observed plateau rapidly disappears around 30 K, well below T_N . This fact also supports the existence of higher order terms because $\langle S^4 \rangle$ term decreases faster than $\langle S^2 \rangle$ term with the temperature.

APPENDIX -GROUND STATE SPIN CONFIGURATIONS OF HCP SPIN LATTICE-

Ground state spin configurations of hcp lattice are investigated classically and the phase diagrams are shown in Fig.4 of §4. The details of the derivation and the related discussions are given in the followings.

Figure A-1 shows the hcp spin lattice, where the unit cell is indicated by thick solid lines. There are two spins per unit cell, which we shall call spin-A (open circles in Fig. A-1) and spin-B (solid circles in Fig.A-1), respectively. Both A- and B-spins form equivalent triangular planes which are denoted as A- and B- planes. We define three exchange parameters J_0 , J_1 and J' as are shown in the figure, with the same notations used in §4. We have the following spin Hamiltonian:

$$H = -2J_0 \sum_{\ell m} (\vec{S}_{\ell A} \vec{S}_{m A} + \vec{S}_{\ell B} \vec{S}_{m B}) - 2J_1 \sum_{\ell m} (\vec{S}_{\ell A} \vec{S}_{m A} + \vec{S}_{\ell B} \vec{S}_{m B}) - 2J' \sum_{\ell m} (\vec{S}_{\ell A} \vec{S}_{m B}). \quad (A1)$$

We treat the spin operators as classical vectors and follow the standard method²²⁾ to obtain the exchange energy. Making Fourier transformation of spins

$$\vec{S}_{m\mu} = S \sum_{\vec{q}} \vec{\sigma}_{\vec{q}\mu} e^{i\vec{q}\vec{R}_m}, \quad (\mu=A, B) \quad (A2)$$

where \vec{R}_m denotes the position of m -th unit cell, the exchange

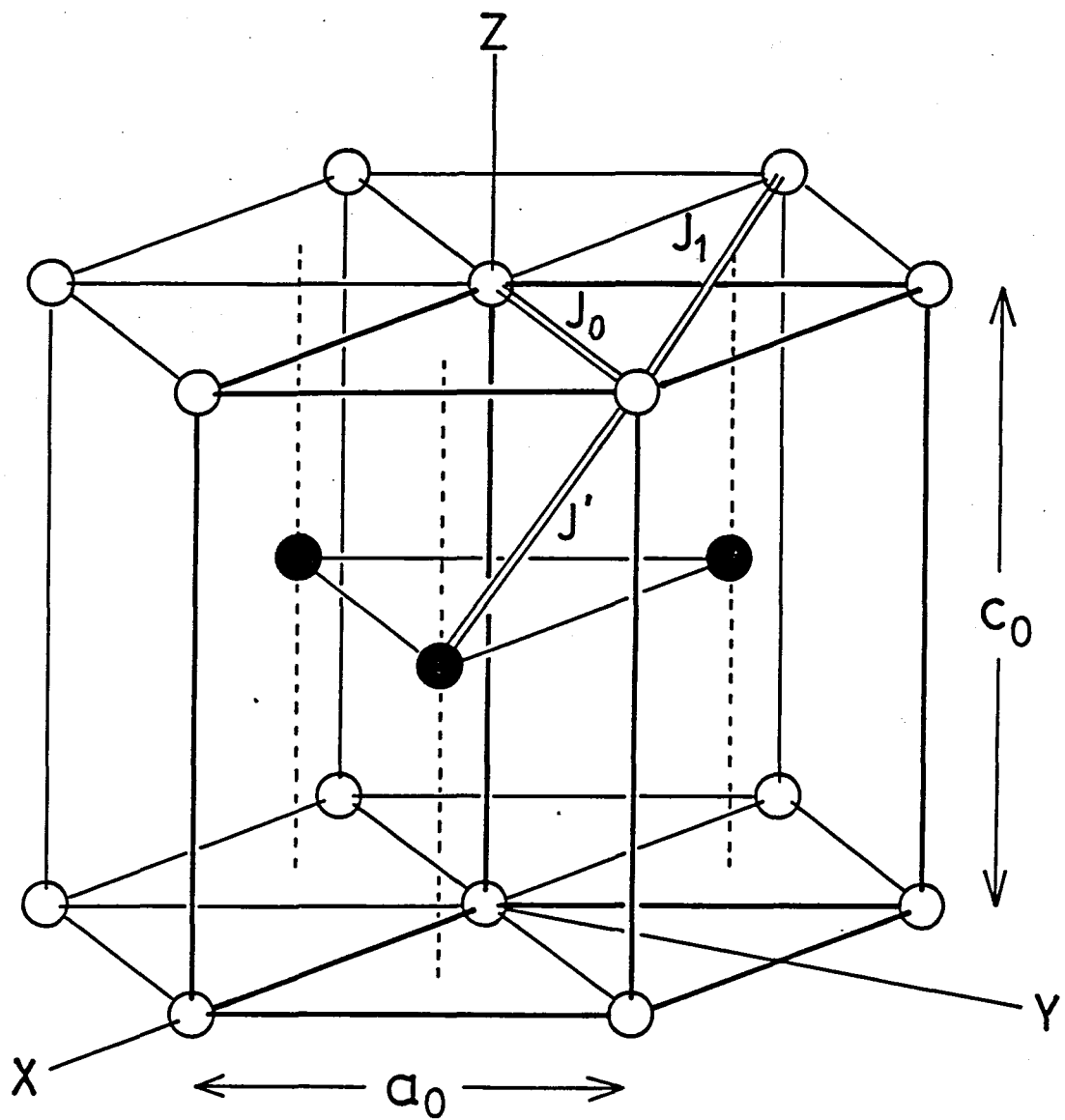


Fig.A-1 hcp spin lattice. Unit cell is indicated by thick line. Open circles denote spin sites on A-plane, and solid circles denote those on B-plane. Three exchange parameters are defined.

energy of given configuration can be written as

$$E(\vec{q}) = -\frac{NS^2}{2} \sum_{\vec{q}} [(J_0(\vec{q}) + J_1(\vec{q}))(|\vec{\sigma}_{\vec{q}A}|^2 + |\vec{\sigma}_{\vec{q}B}|^2) + J'(\vec{q})\vec{\sigma}_{\vec{q}A}\vec{\sigma}_{\vec{q}B}^* + J'(\vec{q})^*\vec{\sigma}_{\vec{q}A}^*\vec{\sigma}_{\vec{q}B}]. \quad (A3)$$

Here N is the number of total spins and $*$ denotes the complex conjugate, and $J_0(\vec{q})$, $J_1(\vec{q})$ and $J'(\vec{q})$ are given by

$$J_0(\vec{q}) = 2J_0(\cos q_x + 2\cos \frac{q_x}{2} \cos \frac{\sqrt{3}q_y}{2}), \quad (A4)$$

$$J_1(\vec{q}) = 2J_1(\cos \sqrt{3}q_y + 2\cos \frac{3q_x}{2} \cos \frac{\sqrt{3}q_y}{2}), \quad (A5)$$

$$J'(\vec{q}) = 2J' \cos \frac{q_z c}{2} (1 + 2\cos \frac{q_x}{2}) e^{-\sqrt{3}q_y i/2} e^{-(3q_y + q_z c)i/2}, \quad (A6)$$

with the coordinate axis shown in Fig.A-1. Here $c = c_0/a_0$ and a_0 is taken as unit length. Hereafter, we shall discuss the spin configurations that have single \vec{q} -component.

The complex vector $\vec{\sigma}_{\vec{q}\mu}$ can be written as a combination of two real vectors $\vec{u}_{\vec{q}\mu}$ and $\vec{v}_{\vec{q}\mu}$:

$$\vec{\sigma}_{\vec{q}\mu} = (\vec{u}_{\vec{q}\mu} - i\vec{v}_{\vec{q}\mu})/2. \quad (A7)$$

Using (A7), we can write eq.(A2) as

$$\vec{S}_{m\mu} = S(\vec{u}_{\vec{q}\mu} \cos \vec{q}\vec{R}_m + \vec{v}_{\vec{q}\mu} \sin \vec{q}\vec{R}_m). \quad (A8)$$

From the condition $\vec{S}_{m\mu}^2 = S^2$ (constant), $\vec{u}_{q\mu}$ and $\vec{v}_{q\mu}$ should be orthogonal unit vectors. The energy (A3) can be written as

$$E(\vec{q}) = -\frac{NS^2}{2} [2(J_0(\vec{q}) + J_1(\vec{q})) + (Re J'(\vec{q}))(\vec{u}_{qA}\vec{u}_{qB} + \vec{v}_{qA}\vec{v}_{qB}) + (Im J'(\vec{q}))(\vec{v}_{qA}\vec{u}_{qB} - \vec{u}_{qA}\vec{v}_{qB})]. \quad (A9)$$

It can be shown that the energy minimum of eq.(A9) is realized when $\vec{u}_{qA} \times \vec{v}_{qA} = \vec{u}_{qB} \times \vec{v}_{qB}$ and $\omega = \arg(J'(\vec{q}))$, where ω is the phase difference between A- and B-sites²²⁾. Then the energy (A9) is given by

$$E(\vec{q}) = -NS^2[J_0(\vec{q}) + J_1(\vec{q}) + |J'(\vec{q})|], \quad (A10)$$

or using eqs.(A4)~(A6),

$$E(\vec{q}) = -2NS^2[J_0(\cos q_x + 2\cos \frac{q_x}{2} \cos \frac{\sqrt{3}q_y}{2}) + J_1(\cos \sqrt{3}q_y + 2\cos \frac{3q_x}{2} \cos \frac{\sqrt{3}q_y}{2}) + |J'| \cos \frac{q_z c}{2} \sqrt{1 + 4\cos \frac{q_x}{2} \cos \frac{\sqrt{3}q_y}{2} + 4\cos^2 \frac{q_x}{2}}]. \quad (A11)$$

The \vec{q} -vector is determined by minimizing the energy. It is clear from eq.(A11) that $q_z = 0$ is necessary to make $E(\vec{q})$ minimum, so that there is no modulation of the magnetic structure along c-axis. We have only to consider the problem on $q_z = 0$ plane in the first Brillouin zone shown in Fig.A-2.

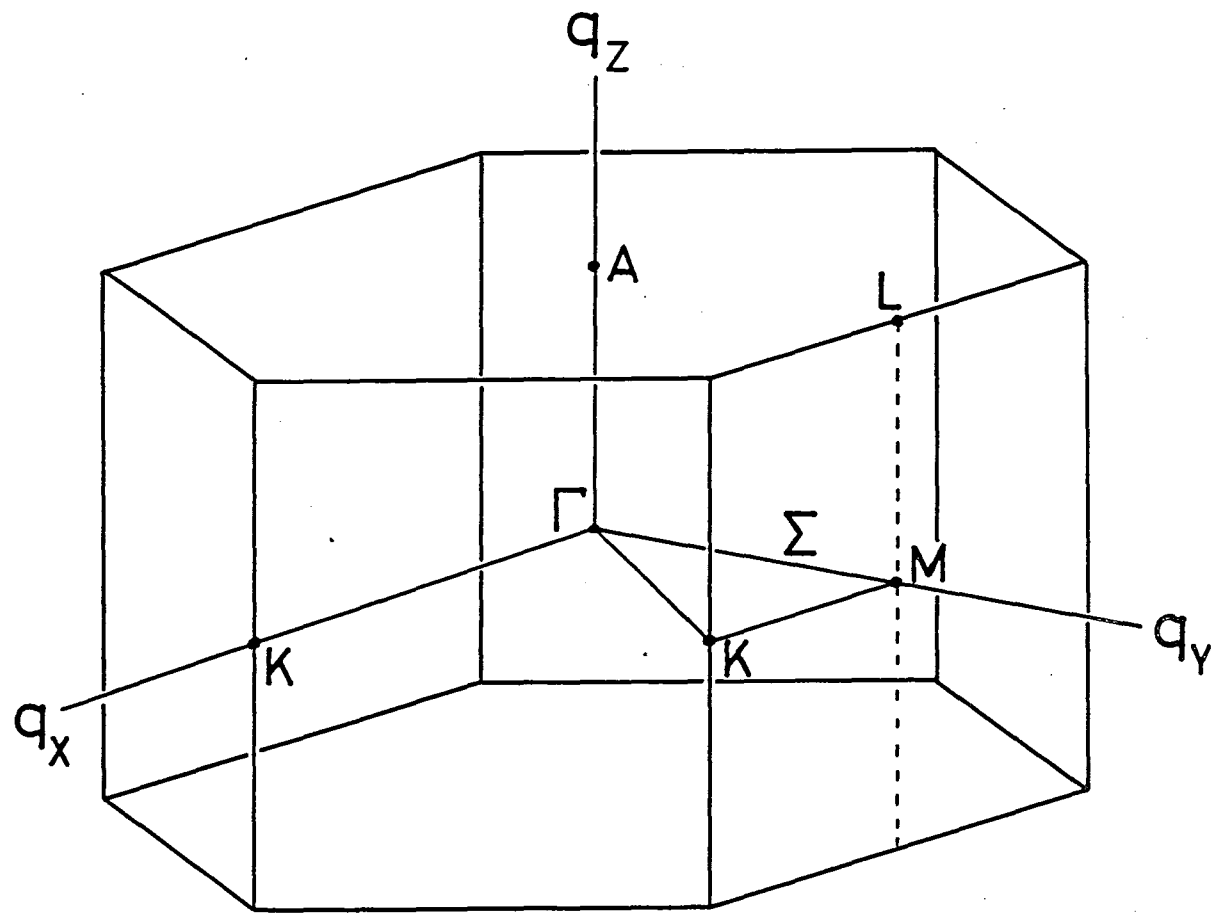


Fig.A-2 First Brillouin zone of hcp lattice.

As is well known, the ground state of the triangular anti-ferromagnetic spin lattice is the spin-triangular state (magnetic order on the K-point of the Brillouin zone). This is found to be the case for hcp lattice if there is no interplane exchange coupling J' . It can be shown that the spin-triangular state is in principle unstable against weak J' . Assuming $|J'/J_0|$ to be small, the exchange energy (A11) can be expanded around the K-point ($\vec{q}_K = (4\pi/3, 0, 0)$) as

$$E(\vec{q}_K + \vec{\delta}) = -2NS^2 \left[-\frac{3}{2}J_0 + 3J_1 + \frac{3}{8}J_0\delta^2 - \frac{9}{4}J_1\delta^2 + \frac{\sqrt{3}}{2}|J'| \delta \right. \\ \left. - \frac{J_0}{8}\delta^3 \alpha \cos 3\theta + \dots \right], \quad (J_0 < 0), \quad (A12)$$

where $\vec{\delta} = \delta(\cos\theta, \sin\theta, 0)$ and $\alpha = \frac{\sqrt{3}}{2} - |J'/J_0|\delta^{-1}$. It is noted that J' introduces a linear term in δ . As the result, $E(\vec{q})$ takes minimum at finite value of δ . Up to the second order terms in the expansion, minimum of $E(\vec{q})$ is realized on a ring of radius δ_0 around the K-point (Fig.A-3):

$$\delta_0 = 2\sqrt{3}|J'|/(18J_1 - 3J_0). \quad (A13)$$

Here, J_1 is assumed to be larger than $(1/8)J_0$, or otherwise a simple antiferromagnetic state becomes stable as is shown in the phase diagram (see Fig.4a). When the third order term in δ is taken into account, the degeneracy on the ring is removed. There are two cases according to the sign of J_1 . If $J_1 > 0$ (ferromagnetic),

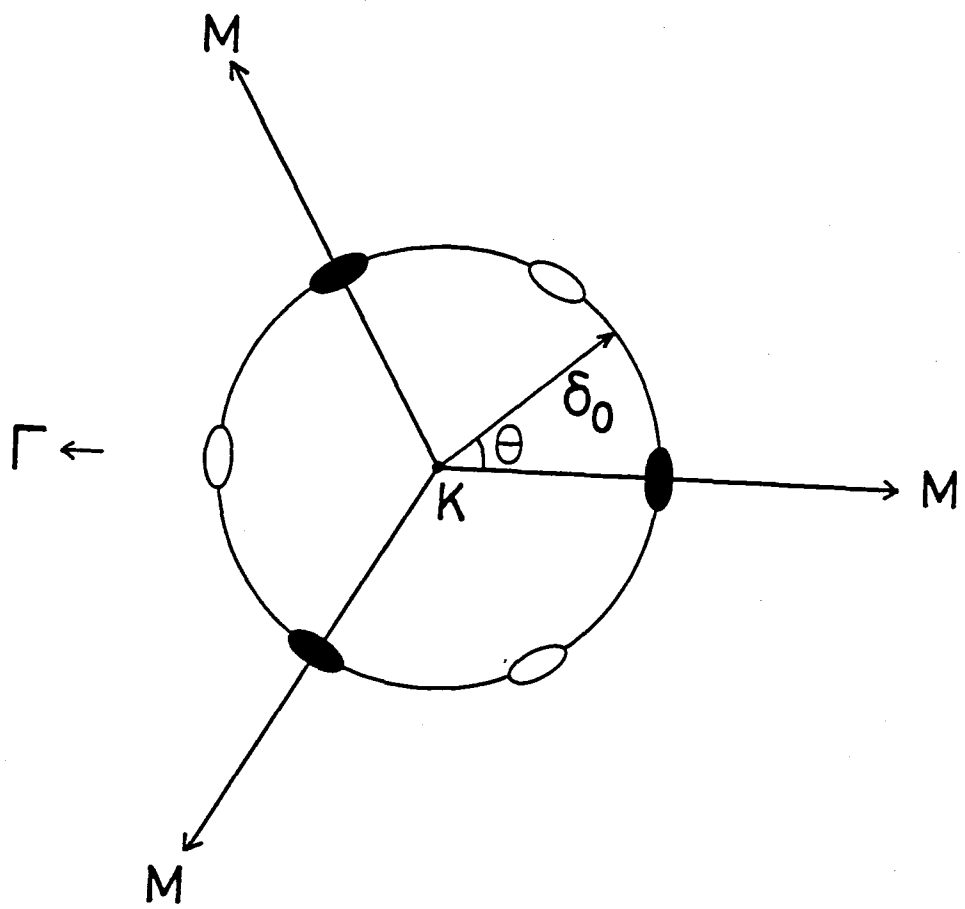


Fig.A-3 Energy minimum around K-point when $J_0 < 0$. Solid point: $J_1 < 0$; white point: $J_1 > 0$. δ_0 is given in the text.

$\alpha = \frac{\sqrt{3}}{2} - |J'|/J_0 |\delta_0|^{-1}$ is negative and $E(\vec{q})$ takes minimum when $\cos 3\theta = -1$ (indicated by white points in Fig.A-3), while if $J_1 < 0$ (antiferromagnetic), α becomes positive and $\cos 3\theta = 1$ is the stable state (black points in Fig.A-3). The corresponding spin structures are obtained, by making use of eq.(A8), as incommensurate triangular states where the spin rotation angle ϕ is given as $2\pi/3 + \delta_0/2$ and $2\pi/3 - \delta_0/2$ for the cases $J_1 < 0$ and $J_1 > 0$, respectively. It is noted that if $J_1 = 0$, $E(\vec{q})$ is degenerated on the ring in Fig.A-3 up to the third order in δ .

A similar instability around K-point is discussed by Shiba⁴⁾, who considered the effect of dipole-dipole interaction in the antiferromagnetic triangular spin lattice. In that case, the ordered state is realized as a sinusoidal incommensurate structure, which can exist only in the temperature region near T_N .

The incommensurate structures obtained here are the consequence of a kind of the frustration effect in hcp lattice. This can be explained by a simple model given in Fig.A-4, where three spins $\vec{S}_{1A} \sim \vec{S}_{3A}$ on A-plane and the site 2B on the adjacent B-plane are shown. The spin \vec{S}_{2B} at site 2B interacts with $\vec{S}_{1A} \sim \vec{S}_{3A}$ through J' . Consider the interplane exchange field \vec{H}_{E2B} acting on site 2B:

$$\vec{H}_{E2B} = 2J'(\vec{S}_{1A} + \vec{S}_{2A} + \vec{S}_{3A})/g\mu_B. \quad (A14)$$

Obviously, if $\vec{S}_{1A} \sim \vec{S}_{3A}$ are in the commensurate triangular state ($\phi = 120^\circ$), \vec{H}_{E2B} vanishes and there is no energy reduction with respect to J' .

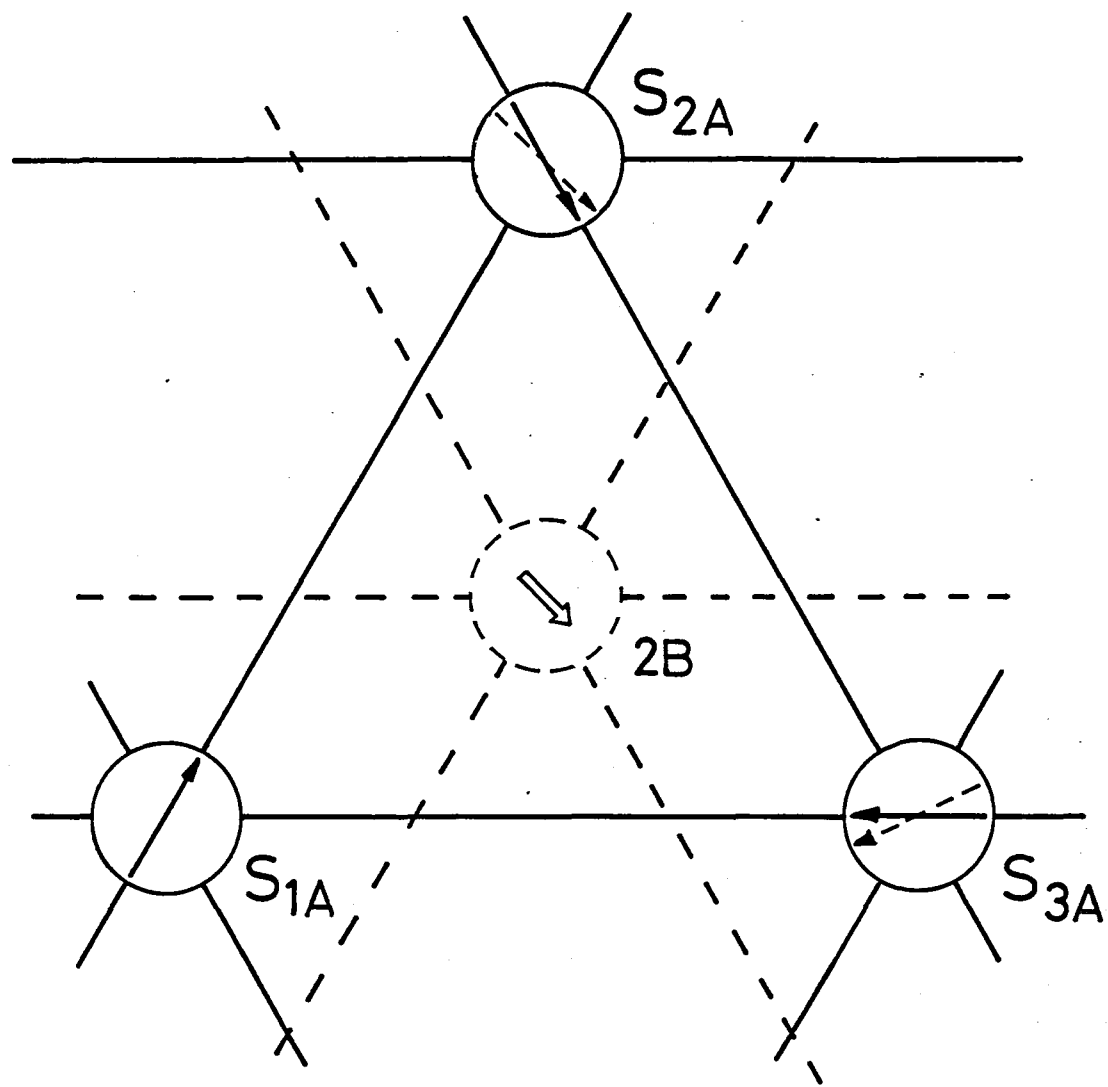


Fig.A-4 Frustration of hcp lattice. Three spins $\vec{S}_{1A} \sim \vec{S}_{3A}$ on the A-plane are shown. In the commensurate triangular state (solid arrows), no interplane exchange field acts on the site 2B on the adjacent B-plane from $\vec{S}_{1A} \sim \vec{S}_{3A}$, while the incommensurate structure (dotted arrows) produces the exchange field on the site 2B indicated by white arrow.

On the other hand, the incommensurate structure shown by dotted arrows in Fig.A-4 produces the exchange field \vec{H}_{E2B} indicated by a white arrow in the figure and can decrease the interplane exchange energy by placing the spin \vec{S}_{2B} parallel to \vec{H}_{E2B} . The structure of course increases the intraplane exchange energy, so that the stable state is realized when these two energies balance.

As can be seen from eq.(A13), δ_0 is small when J_1 is positive and large. In our case of C_6Eu , the obtained parameters J_0 , J_1 and J' give $\delta_0/q_K=0.01$ so that one can substantially regard it as a "commensurate" triangular state. On the other hand, when J_1 is negative, the modification of the triangular structure becomes significant.

Other phases shown in Fig.8 are similarly obtained by finding the minimum points of eq.(A11). The phase boundaries given by thick solid lines indicate the first order boundaries, where the \vec{q} -vector changes discontinuously. Other boundaries are the second order ones where the \vec{q} -vector changes continuously. Phase I is the order on the Γ -point, which is ferromagnetic when $J' > 0$, and antiferromagnetic with ferromagnetic plane coupled antiferromagnetically along c-axis when $J' < 0$. Phase II is an antiferromagnetic order on the M-point, and phases V and V' are the helical structure with the \vec{q} -vector between Γ and M-points (indicated by Σ in Fig.A-2).

REFERENCES

- (1) M. Suzuki and H. Ikeda: J. Phys. Cl4 (1981) L923.
- (2) M. Elahy, C. Nicolini, G. Dresselhaus and G.O. Zimmermann; Solid State Commun. 41 (1982) 289.
- (3) T. Haseda, N. Wada, M. Hata and K. Amaya: Physica 108B (1981) 841.
- (4) H. Shiba: Solid State Commun. 41 (1982) 511.
- (5) M. Mekata and K. Adachi: Solid State Physics(Japan) 17 (1982) 491.
- (6) M.E. Makrini, D. Guerard, P. Lagrange and A. Herord: Physica 99B (1980) 481.
- (7) H. Suematsu, K. Ohmatsu and R. Yoshizaki: Solid State Commun. 38 (1981) 1103.
- (8) H. Suematsu, K. Ohmatsu, K. Sugiyama, T. Sakakibara, M. Motokawa and M. Date: Solid State Commun. 40 (1981) 241.
- (9) M. Date, T. Sakakibara, K. Sugiyama and H. Suematsu: to be published in proceedings of International Symposium on High Field Magnetism 1982, Osaka.
- (10) R.A. Guyer: J. Low Temp. Phys. 30 (1978) 1.
- (11) M. Roger, J.M. Delrieu and J.H. Hetherington: Phys. Rev. Lett. 45 (1980) 137.
- (12) A. Yoshimori and S. Inagaki: J. Phys. Soc. Jpn. 44 (1978) 101; J. Phys. Soc. Jpn. 50 (1981) 769.
- (13) I. Hase, H. Fukuda and A. Yoshimori: J. Phys. Soc. Jpn. (1981) 774.

- (14) K. Yosida and S. Inagaki: J. Phys. Soc. Jpn. 50 (1981) 3268.
- (15) M. Takahashi: J. Phys. C 10 (1977) 1289.
- (16) J. Hara and H. Fukuyama: Technical Report of ISSP, Ser A, No.1129 (1981).
- (17) C. Herring: Magnetism IIB, ed. by Rado and Suhl, Academic Press, New York, 1966.
- (18) E.A. Harris and J. Owen: Phys. Rev. Lett. 11 (1963) 9; D.S. Rodbell, I.S. Jacobs and J. Owen: Phys. Rev. Lett. 11 (1963) 10.
- (19) M. Matsuura, Y. Okuda, M. Morotomi, M. Mollymoto and M. Date: J. Phys. Soc. Jpn. 46 (1979) 1031.
- (20) G. Kaindl, J. Feldhaus, U. Ladewig and K.H. Frank: Phys. Rev. Lett. 50 (1983) 123.
- (21) A. Narath: J. Phys. Soc. Jpn. 19 (1964) 2245.
H. Kobayashi and T. Haseda: J. Phys. Soc. Jpn. 19 (1964) 765.
- (22) T. Nagamiya: Solid State Physics, ed. by Seitz, Turnbull and Ehrenreich, Academic Press 1967.
- (23) K. Yosida: Supplement of Prog. Theor. Phys. 69 (1980) 475.

PART III

HIGH FIELD MAGNETIZATION OF

RANDOMLY DILUTED ANTIKERROMAGNET $Fe_{1-x}Zn_xF_2$

ABSTRACT

High field magnetization measurements of the randomly diluted, anisotropic antiferromagnet $Fe_{1-x}Zn_xF_2$ ($0 \leq x \leq 0.9$) are done up to 550 kOe in the temperature range 1.3 K to T_N . Spin-flop field H_{SF} of pure FeF_2 is obtained as 414 ± 5 kOe, and the bi-critical point is found at $H_B = 478 \pm 5$ kOe, T_B (adiabatic) = 59 ± 1 K. Novel series of single-spin "exchange-flips" are observed in the diluted specimens, in addition to the concentration-dependent H_{SF} . The exchange flips occur when the applied field H_0 exceeds the effective exchange field $H_E' = nH_E/z$ at sites on the down-sublattice with n magnetic neighbors. Hysteresis boundary, marked by anomalous peak in dM/dH versus H_0 , is found, which smoothly connects with T_N at $H_0 = 0$. This effect is explained by order-disorder transition in the diluted system.

§ 1. INTRODUCTION

In recent years, magnetic and electronic properties of randomly diluted antiferromagnets have been attracting considerable attention^{1,2)}. Above all, rutile compounds of Mn²⁺ and Fe²⁺ have been playing an important role in the study of random magnetic materials since their crystallographic and magnetic structures are very simple. Among these, diluted FeF₂ is particularly interesting because Fe²⁺ has strong uniaxial crystal field anisotropy in the compound, which is nearly comparable with the exchange energy in the diluted system. Therefore, much work has been done on the system concerning static and dynamic properties^{3~8)}. As for the magnetization process of a random system, however, no clear or interesting phenomenon is reported. One reason may be a technical difficulty that the magnetization study of these systems needs very strong magnetic field, especially for high anisotropy systems. For example, the spin-flop transition field (H_{SF}) of pure FeF₂ is estimated as over than 400 kOe⁹⁾ so that it is far beyond the limit of static field. Considering these points, we have done high field magnetization measurements of high anisotropy diluted antiferromagnet Fe_{1-x}Zn_xF₂ under pulsed magnetic field^{10,11)}. The research was done in cooperation with A.R. King and V. Jaccarino of University of California, Santa Barbara (UCSB).

Our Initial motivation for studying this system was to investigate the concentration dependence of the spin-flop field.

As is well known, an antiferromagnet with weak anisotropy shows spin-flop (SF) at low temperature, while a metamagnetic transition appears when the uniaxial anisotropy field H_A exceeds the exchange field H_E . Therefore, one would expect a cross over effect from SF to metamagnetic behaviour at some concentration x in $\text{Fe}_{1-x}\text{Zn}_x\text{F}_2$, where only the exchange coupling, not the anisotropy, is diluted. It was also our interest to examine a H_0 -T phase diagram of pure FeF_2 , which has not been obtained for the critical field is very high⁹⁾.

During the experiment, we observed, rather unexpectedly, a novel series of field induced "exchange flips" in addition to the concentration dependent spin-flop field $H_{SF}(x)$. The spins with $n=1, \dots, 8$ exchange coupled neighbours would have effective exchange fields $H_E' = (n/z)H_E$, where $z=8$ is the coordination number. When the external field H_0 just exceeds H_E' , the total field acting on these spins residing on the down spin sublattice (spins anti-parallel to H_0) reverses direction. An abrupt magnetization reversal (exchange flip) will occur for these spins at $H_0 = (n/8)H_E$, so long as $H_E' < H_{SF}(x)$. In addition to these transitions, we observed a new boundary in the field marked by an anomalous peak in dM/dH_0 . When H_0 exceeds the boundary, considerable hysteresis is observed in the magnetization process. The boundary is found to be well explained by an idea of order-disorder transition.

The magnetic phase diagram of randomly diluted antiferromagnet is also of current interest from a viewpoint that

the system can be considered as an experimental realization of "random field effect"¹²⁾. One of the interesting consequences of the effect is the lowering of the spatial dimensionality of the system. Drastic decrease of T_N under the field, or a new type of critical behaviours characteristic of a lower dimensional systems were predicted^{12~15)}, and many experiments^{8,16~20)} were performed. Absence of the long range order in the two dimensional Ising system under a random field was predicted¹⁴⁾, which was confirmed by the neutron diffraction experiment on $Rb_2Co_{1-x}Mg_xF_4$ ¹⁸⁾. There seems to be, however, a confliction between theory and experiment on the point whether a lower critical dimensionality d_L of the Ising system, below which no long range order can occur in the presence of a weak random field, is 2 or 3. If d_L is 3, three dimensional diluted antiferromagnet does not show long range magnetic order under a weak field applied along the easy axis.¹⁵⁾ However, neutron diffraction experiment of $Mn_{1-x}Zn_xF_2$ showed no destruction of the long range order up to 40 kOe²⁰⁾. Specific heat measurements on $Fe_{1-x}Zn_xF_2$ and $Mn_{1-x}Zn_xF_2$ ⁸⁾ revealed sharp magnetic transitions in the systems up to 20 kOe and showed the existence of the long range order at least at low field region.

The order-disorder boundary observed in the present experiment is found to smoothly connect with the antiferromagnetic to paramagnetic phase boundary determined in Ref.8. Therefore, we take an empirical approach and refer to it as a phase transition.

§ 2. CRYSTAL AND MAGNETIC STRUCTURES

The crystal structure of pure FeF_2 is shown in Fig.1. The cation sites are surrounded by a distorted octahedron of fluorine ions, the point symmetry being D_{2h} . The environment of the corner ions differs from that at the body center by a rotation of 90° about the c-axis.

The Fe^{2+} ion has a $3d^6$ configuration and a 5D ground term. In an octahedral crystal field the orbital degeneracy of the ground term is reduced into a lower triplet and an excited doublet orbital state separated by some 10000 cm^{-1} . The orthorhombic D_{2h} symmetry further removes all the orbital degeneracy. The energy of the first excited state above the ground singlet state is determined as 1115 cm^{-1} 21). The fivefold spin degeneracy of the ground singlet is removed by spin-orbit coupling λ , resulting in a uniaxial anisotropy of the form $-DS_z^2$. The magnitude of D is of order λ^2/Δ , where $\lambda=-63 \text{ cm}^{-1}$ 22) and Δ is the energy of the first excited state at 1115 cm^{-1} . Consequently, Fe^{2+} has large single ion anisotropy D 22). Below Néel temperature $T_N=78.4 \text{ K}$, spins order along c-axis as shown in Fig.1 by arrows. The magnetic unit cell is the same size as the chemical cell. Exchange interactions J_v ($v=1,2,3$) and the uniaxial anisotropy D of FeF_2 are precisely determined by neutron inelastic scattering study 3), where J_v are defined as in Fig.1. Using the standard notations of the spin Hamiltonian in the next page,

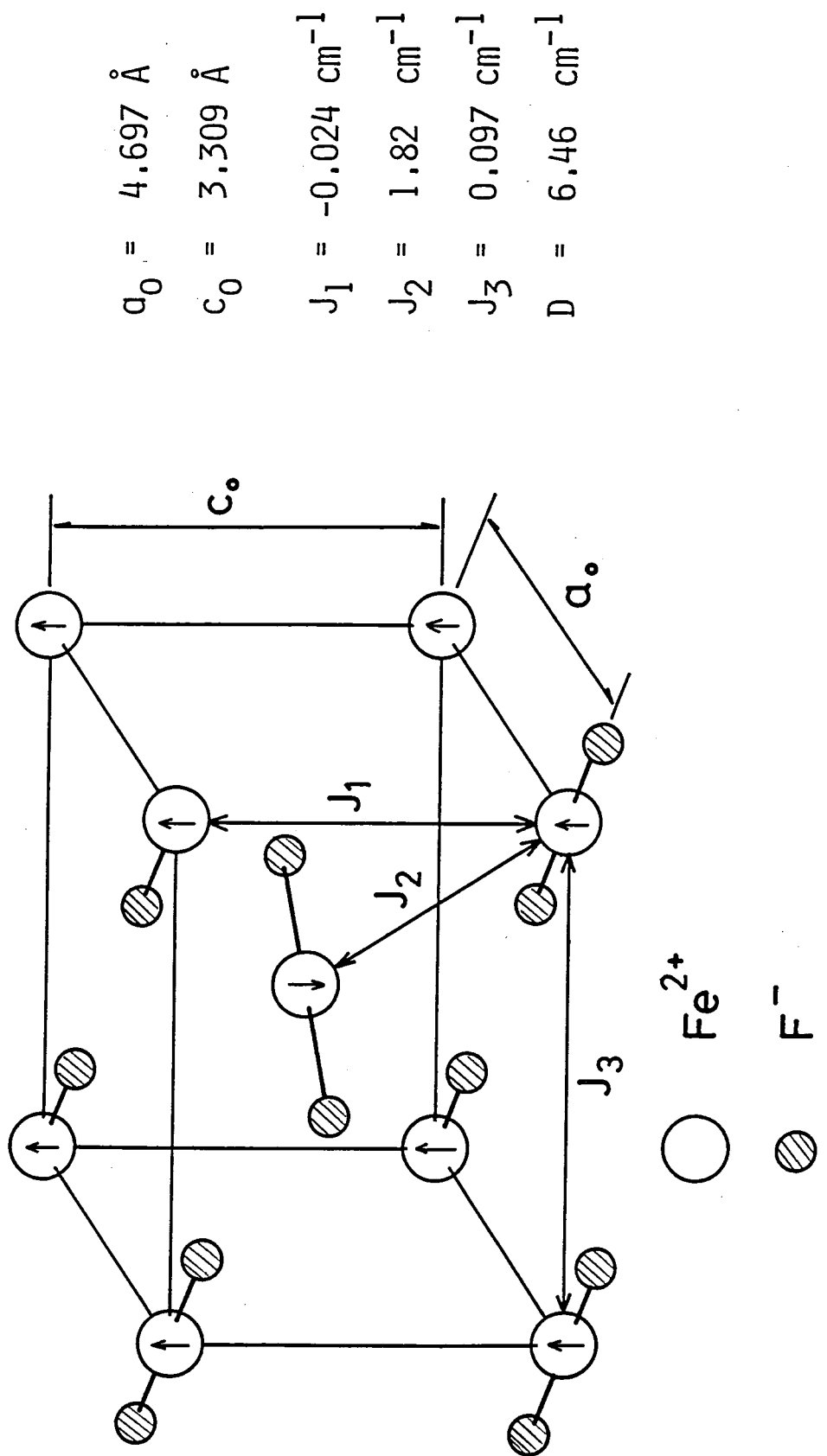


Fig.1 Crystal structure of FeF_2 . Small arrows indicate the spin alignment at the ordered state below $T_N = 78 \text{ K}$.

$$H = 2 \sum_{\langle i,j \rangle} J \vec{S}_i \vec{S}_j - D \sum_i S_{iz}^2, \quad (1)$$

the parameters are determined (in cm^{-1}) as follows³⁾:

$$J_1 = -0.024 \pm 0.030; \quad J_2 = 1.82 \pm 0.05; \quad J_3 = 0.097 \pm 0.030; \quad D = 6.46 \pm 0.29. \quad -0.10.$$

Effective anisotropy field H_A and intersublattice exchange field H_E are respectively given by $H_A = [(2S-1)D + E_d]/g\mu_B = 191 \text{ kOe}$ and $H_E = 2zJ_2S/g\mu_B = 554 \text{ kOe}$, where $E_d = 0.68 \text{ cm}^{-1}$ is the dipolar energy³⁾, g is the g -value ($= 2.25^{22)$) and μ_B is the Bohr magneton.

From these values, H_{SF} is estimated by molecular field theory as

$$H_{SF} = \sqrt{2H_E H_A - H_A^2} = 419 \text{ kOe.} \quad (2)$$

ZnF_2 is an isostructural compound with FeF_2 and has almost the same lattice parameters with FeF_2 ($a_0 = 4.703 \text{ \AA}$ and $c_0 = 3.134 \text{ \AA}$ for ZnF_2). Therefore, the mixed crystal $\text{Fe}_{1-x}\text{Zn}_x\text{F}_2$ will provide a simple and interesting model system of a diluted antiferromagnet because H_A is nearly x -independent while averaged exchange field $H_E(x)$ decreases linearly with x ⁶⁾. The x -dependence of the Néel temperature $T_N(x)$ is measured and the percolation limit x_p is found as around $0.76^{4,6)$. Interestingly, $T_N(x)$ in the range $0 < x < 0.7$ decreases linearly with x toward $x=1$, not toward x_p . This behaviour is theoretically explained as due to the Ising-like anisotropy of the system.⁵⁾

§ 3. EXPERIMENTAL PROCEDURE AND RESULTS

3.1 Experimental Procedure

High field magnetization measurements at liquid helium temperature were performed up to 550 kOe by D-2 2L Magnet and cryostat. Temperature-dependent measurements up to 360 kOe were done by D-2 1L Magnet and the temperature controlled cryostat. The H_0 -T phase diagrams above 360 kOe were obtained also by D-2 2L Magnet. In this case, the field was applied during specimens were gradually warming up after the level of the liquid helium dropped below the position of the specimens.

The specimens were twelve single crystals of $Fe_{1-x}Zn_xF_2$ with x varying from 0 (pure FeF_2) to 0.9, beyond the percolation limit $x_p = 0.76$. These were grown at UCSB by the Bridgeman method, and cut into rods of 2X2X10 mm. The longest dimension was the c-axis, which was aligned parallel to H_0 within 1° . The demagnetizing factor of the arrangement was estimated as about 0.04, so that the demagnetizing field was negligible and no correction was done.

3.2 Low Temperature Results

A series of dM/dH_0 vs. H_0 data for all the concentration range are shown in Figs. 2 and 3, illustrating the outline of the main effects seen in the low temperature region. The data were taken at 4.2 K ($x \leq 0.19$) and 1.3 K ($x > 0.19$). First of all, pure FeF_2 showed a spin-flop at the field $H_{SF} = 414 \pm 5$ kOe,

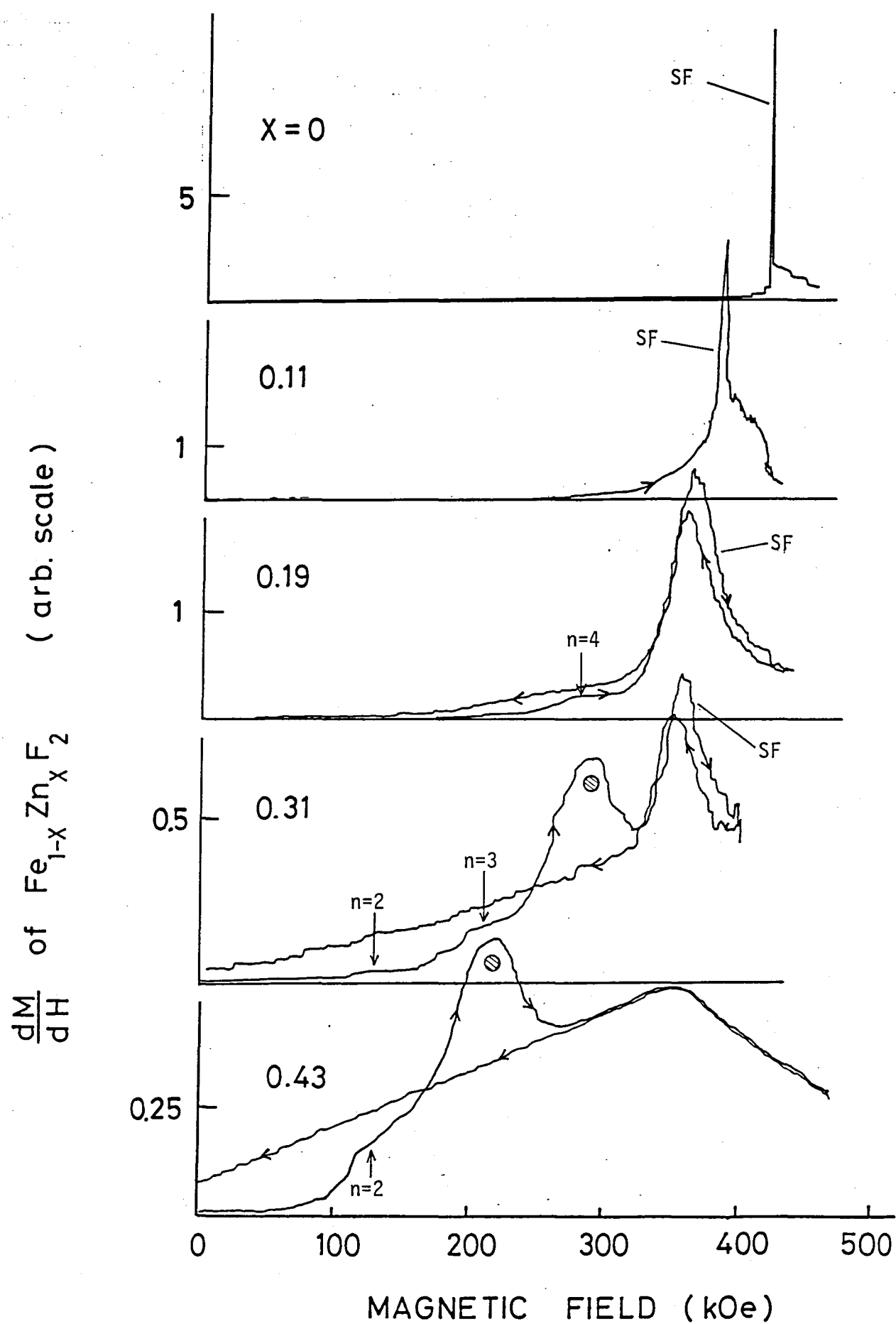


Fig.2 dM/dH_0 of $\text{Fe}_{1-x}\text{Zn}_x\text{F}_2$, $0 \leq x \leq 0.43$, as a function of field. Spin-flop(SF) and exchange flips($n=2 \sim 4$) are indicated. Shaded circles mark the peaks at the hysteresis boundary. Direction of field scan is indicated by arrows along the curves.

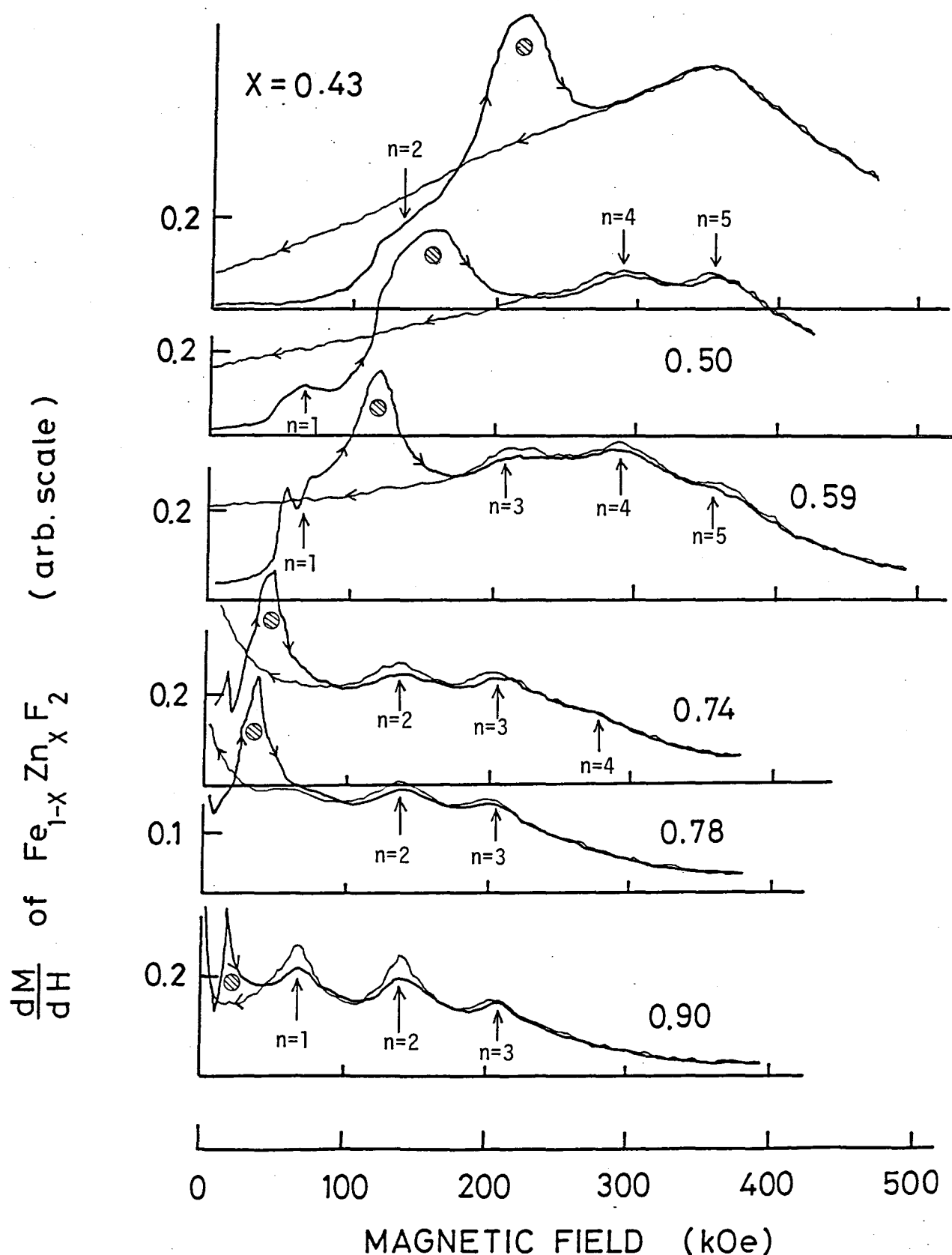


Fig.3 dM/dH_0 of $\text{Fe}_{1-x}\text{Zn}_x\text{F}_2$, $0.43 \leq x \leq 0.9$, as a function of field. Exchange flips ($n=1 \sim 5$) are indicated. Shaded circles mark the peaks at the hysteresis boundary. Direction of field scan is indicated by arrows along the curves.

in good agreement with the predicted value (2). No significant hysteresis is found. It is noticed that this is the first observation of the spin-flop in FeF_2 ¹¹. With the dilution, the spin-flop first decreases in the field H_{SF} , becoming broad and disappears at around $x=0.43$ despite the virtual crystal approximation (VCA) prediction that the spin-flop would persist until $x \sim 0.6$. Here the averaged exchange field $H_E(x)$ becomes equal to the anisotropy field $H_A(x)$ and metamagnetism would occur in this approximation. We believe that a large peak appearing in $x=0.31$ around 350 kOe is a spin-flop.

In addition to the spin-flop, there found peaks in dM/dH_0 data with almost regular interval in the field. These peaks occur at around fields $H_0 \approx 70n$ kOe, $n=1, 2, \dots, 5$, nearly independent of the concentration. These peaks will be interpreted later in terms of independent spin reversal so that we shall hereafter call them as "spin-flips" or "exchange flips" and distinguish them from the cooperative spin-flop. The case of $x=0.19$ is shown in more detail in Fig.4, where the dM/dH_0 data are shown by successively changing the maximum applied field $H_{0\max}$. Peaks in dM/dH_0 corresponding to exchange flips $n=2$ to 4 and the spin-flop(SF) are indicated. As can be seen, the exchange flips are observed in both field-increasing and decreasing scans so long as $H_{0\max}$ does not exceeds H_{SF} . If $H_{0\max}$ exceeds H_{SF} , no flip is seen in the field-decreasing scan. The corresponding magnetization curve is given in Fig.5. The hysteretic behaviour can be seen below H_{SF} .

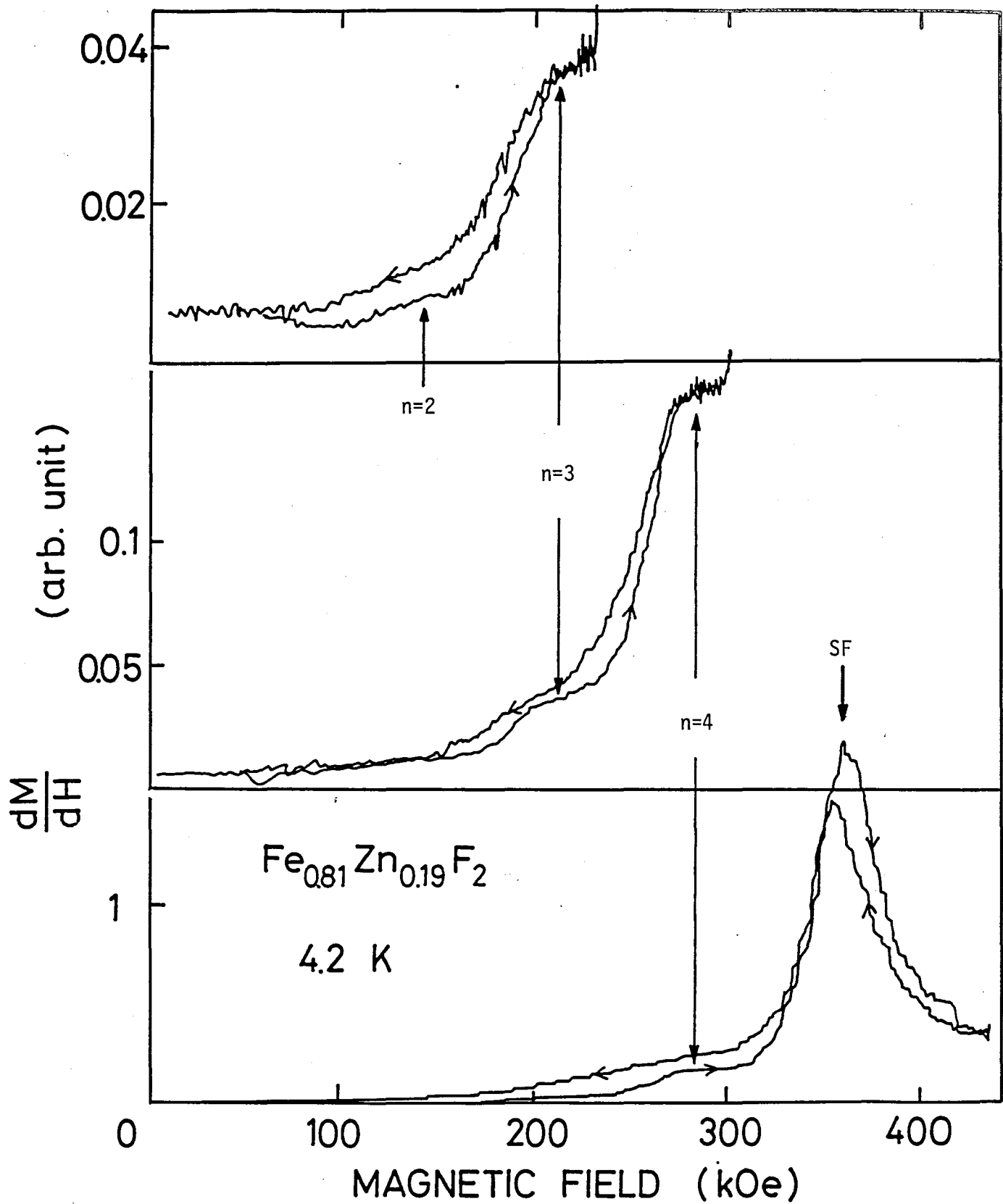


Fig. 4 dM/dH of $\text{Fe}_{0.81}\text{Zn}_{0.19}\text{F}_2$. Spin-flop(SF) and exchange flips($n=2\sim 4$) are indicated. Arrows on the curves indicate the direction of field scan.

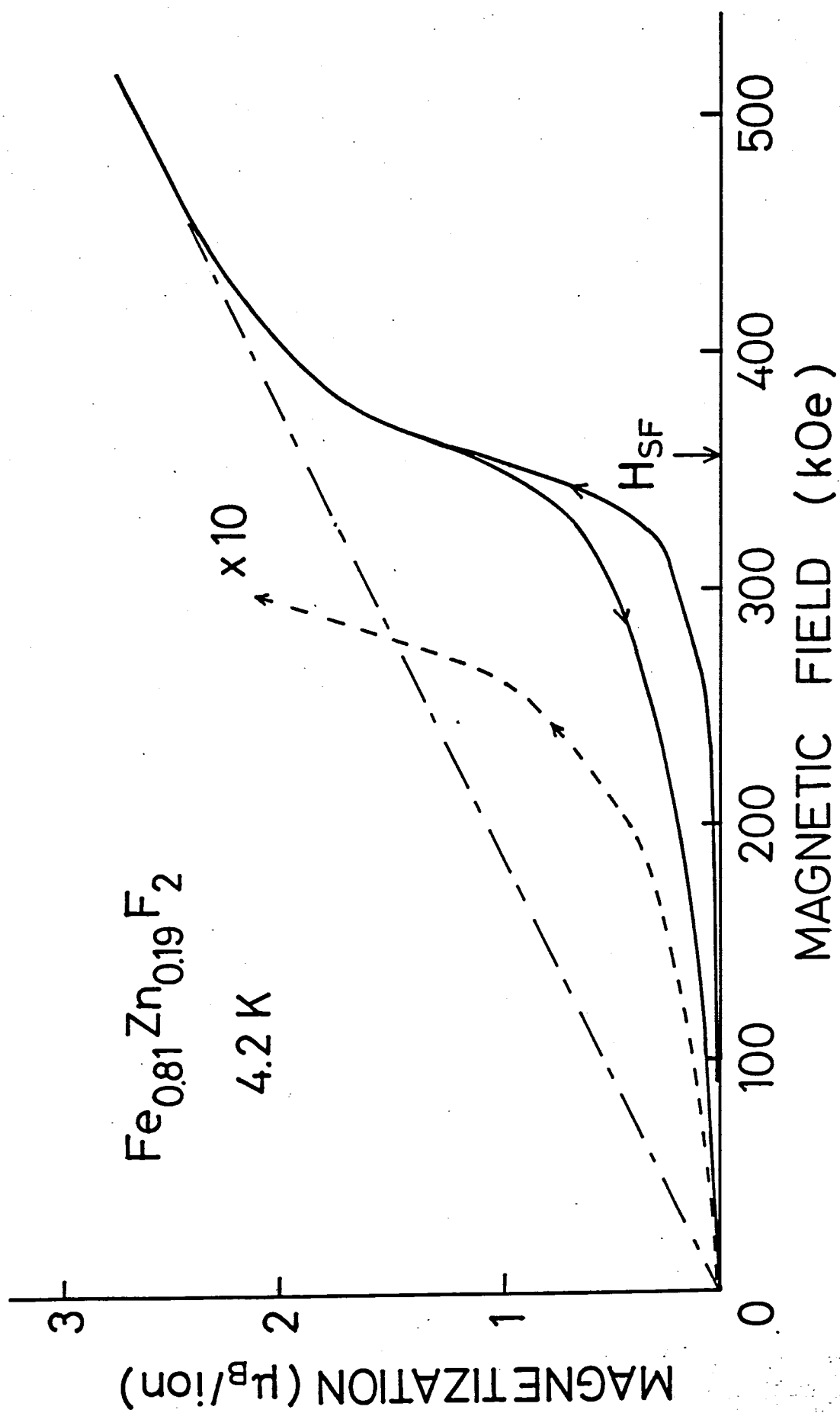


Fig. 5 Magnetization curve of $\text{Fe}_{0.81}\text{Zn}_{0.19}\text{F}_2$. Arrows indicate the direction of field scan. Spin-flop field H_{SF} is shown.

In more diluted specimen, another kind of hysteresis boundary in the field is observed. The case of $x=0.27$ is shown in Fig.6, where dM/dH_0 is displayed as a function of H_0 by successively changing $H_{0\max}$ as in Fig.4. Exchange flips $n=1$ to 3 are clearly seen in Figs.6c-e with little hysteresis. On the other hand, when $H_{0\max}$ exceeds a peak marked by a shaded point in Fig.6b, the dM/dH_0 returns back in completely different way from the field-increasing scan, showing no exchange flip. The new hysteresis boundary accompanied by the anomalous peak in dM/dH_0 is hereafter called as H_h . The magnetization curve of $x=0.27$ is shown in Fig.7, where the spin-flop field H_{SF} and the hysteresis boundary H_h are indicated by arrows. The curve shows large hysteresis below H_h , while no hysteresis is found above H_{SF} . The magnetization above 400 kOe shows nearly linear increase with the field and no higher flip is observed up to 550 kOe.

Further dilution decreases H_h and moves the anomalous peaks marked by shaded points in Figs.2 and 3 toward lower field, bringing it below the $n=1$ flip near the percolation limit x_p . Specimens with $x>0.5$ show exchange flips above H_h with little hysteresis. No significant change is observed in a magnetization process around x_p . The exchange flips become even sharper in $x=0.9$, which possesses no long range order at all. Moreover, this sample still shows hysteretic behaviour at the initial stage of the magnetization process accompanying an apparent anomalous peak only seen in the field-increasing scan.

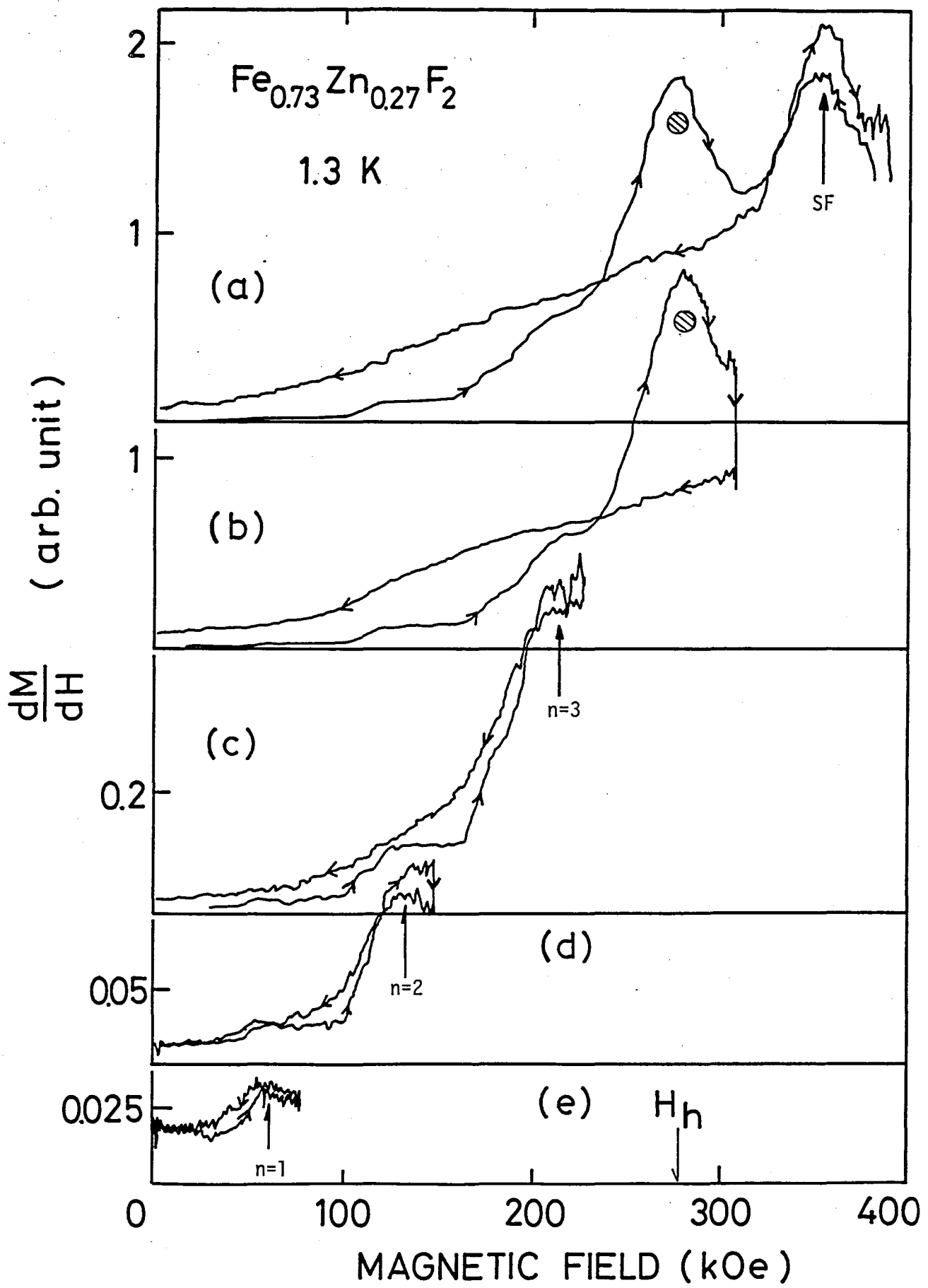


Fig.6 dM/dH_0 of $\text{Fe}_{0.73}\text{Zn}_{0.27}\text{F}_2$. Spin-flop(SF) and exchange flips($n=1\sim 3$) are indicated. Shaded circles mark the peak at the hysteresis boundary. Direction of field scan is indicated by arrows along the curves.

$\text{Fe}_{0.73} \text{Zn}_{0.27} \text{F}_2$

1.3 K

MAGNETIZATION (H_B/ion)

500
400
300
200
100
0

MAGNETIC FIELD (kOe)

H_h

H_{SF}

Fig. 7 Magnetization curve of $\text{Fe}_{0.73} \text{Zn}_{0.27} \text{F}_2$. Arrows on the curve indicate the direction of field scan. Spin-flop field H_{SF} and the hysteresis boundary H_h are also shown.

The low temperature exchange flips, hysteresis boundaries at H_h and spin-flop points for all specimens are collected in Fig. 8. The spin-flop transition is marked by black points in the figure, which extends from FeF_2 ($x=0$) to around $x=0.4$. The thick dashed line represents the VCA prediction of $H_{SF}(x)$: $H_{SF}(x)=\sqrt{2(1-x)H_E H_A - H_A^2}$. The observed spin-flop field first decreases almost linearly with x along the dashed line, and departs from it at around $x=0.3$, leveling off with further dilution. The exchange flips are marked by open circles. It is clearly seen that the exchange flips align with almost regular interval with little concentration dependence. They extend well beyond the percolation limit x_p . As the spin-flop line accidentally ends close to the $n=5$ flip, it is difficult to distinguish between the two. For instance, the character of the highest transition seen in $x=0.43$, indicated by a solid square point near $n=5$ line, is not clear. The hysteresis boundary accompanied by an anomalous peak in dM/dH_0 is indicated by shaded points. It starts at $x=0.27$ and decreases first linearly with x along a line that intersects $H_0=0$ at $x=x_p$, but shows leveling off at around x_p and persists even at $x=0.9$.

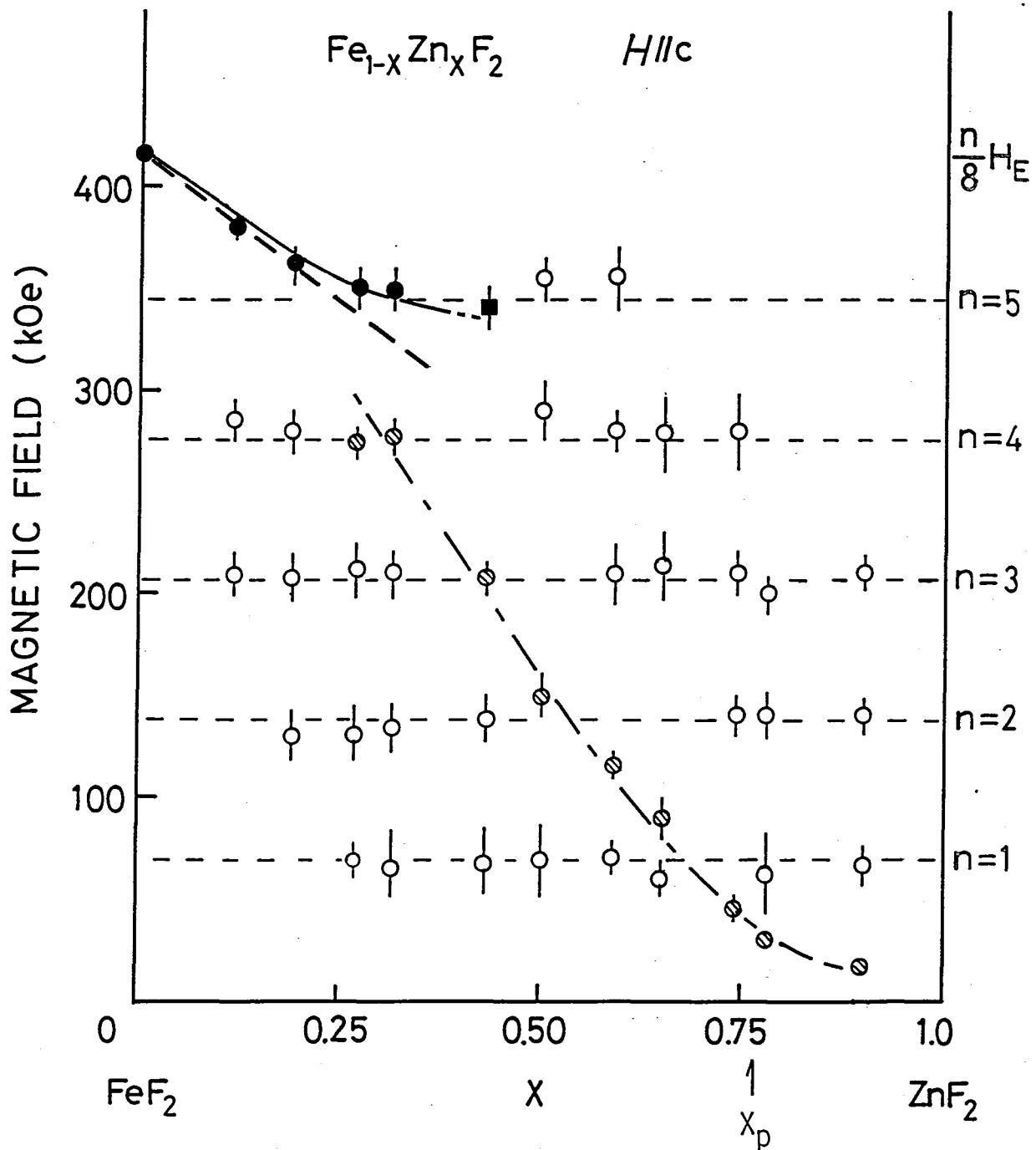


Fig. 8 Transition fields of $\text{Fe}_{1-x}\text{Zn}_x\text{F}_2$. Solid circles are spin-flop, open circles are exchange flips and shaded circles indicate the hysteresis boundary. Horizontal dashed lines represent the predicted exchange flip positions $n=1$ to 5. Thick dashed line is the VCA prediction of the spin-flop field and the solid line is the result of computer simulation.

3.3 Phase Diagrams

The H_0 -T phase boundaries of pure FeF_2 and diluted specimens $x=0.11$ and 0.19 are shown in Fig.9. These samples show spin-flop (SF) at low temperature. In FeF_2 , the SF line is found to increase with the temperature from $H_{SF}=414$ kOe at $T=4.2$ K, to $H_B=478\pm 5$ kOe at the bicritical point (BCP) which is found at $T_B=59\pm 1$ K. Thick solid line below T_B indicates a first order antiferromagnetic (AF) to SF boundary. Field scan across this boundary yields a sharp spike in dM/dH_0 . The thin solid line above T_B indicates a second order AF to P (paramagnetic) boundary. Passing through T_B , qualitative change in dM/dH_0 is observed as shown in Fig.10. The sharp spike seen at $T=58$ K, just below T_B , changes to a λ -shape at $T=60$ K, just above T_B . The λ -shape peak is observed in dM/dH_0 along the AF-P boundary, up to T_N . The SF-P boundary is expected to be nearly vertical so that it is unobservable by field scan. The dot-dashed line shown at the AF-P boundary is a static field results by Shapira²³⁾, who determined the boundary by ultrasonic attenuation measurement up to 200 kOe. The apparent discrepancy between his results and our pulsed field ones may be due to the adiabatic condition involved in the present pulsed field measurements.

In the diluted sample $x=0.11$, small rise in H_{SF} with temperature is observed, from 380 kOe at 4.2 K to 391 kOe at 45 K. A qualitative change in dM/dH_0 is also found between 45 K and 50 K, but is not so clear as in FeF_2 . The BCP, if any, is not determined precisely. More dilute sample $x=0.19$ shows no

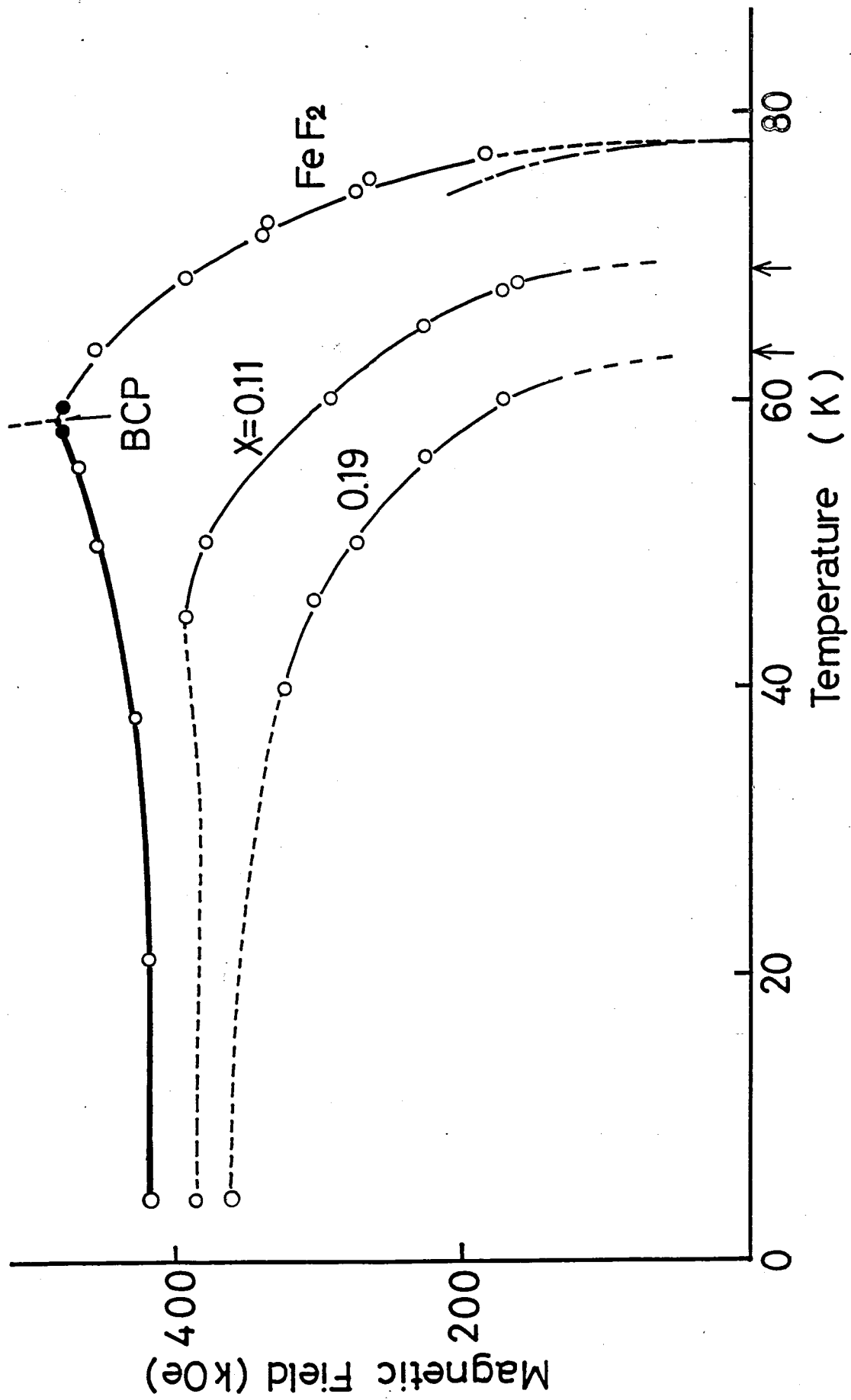


Fig.9 Phase diagrams of $\text{Fe}_{1-x}\text{Zn}_x\text{F}_2$, $0 \leq x \leq 0.19$. Bicritical point (BCP) is found in FeF_2 at $T_B = 59 \pm 1$ K and $H_B = 478 \pm 5$ kOe. Thick solid line indicates the first order antiferromagnetic to spin-flop boundary and thin solid lines are the second order antiferromagnetic to paramagnetic boundaries. Dot dashed line is the static field result²³.

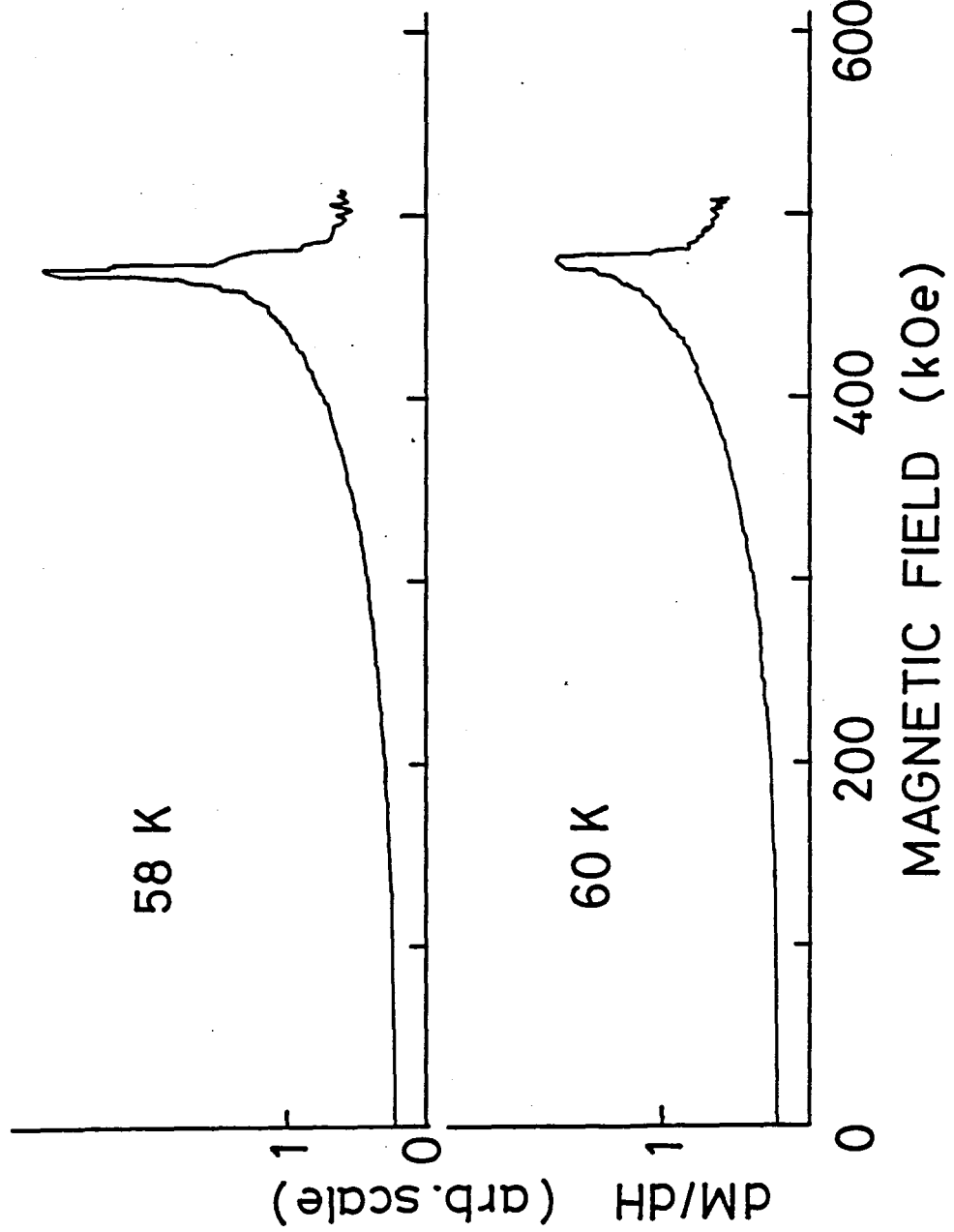


Fig.10 dM/dH_0 of FeF_2 around the bicritical point ($T_B=59$ K), corresponding to two data points indicated by solid circles in Fig.9.

increase in H_{SF} .

The phase diagram of $x=0.31$ is shown in Fig.11, where the temperature dependence of exchange flips are also shown. The exchange flips are found to broaden rapidly and disappear with increasing temperature. The spin-flop boundary increases in the field, broadens and seems to disappear at around 35 K. The complete phase boundary is not known. On the other hand, the hysteresis boundary marked by shaded points is found to go smoothly over into T_N at $H_0=0$ measured previously. It is also found that the high-end of the boundary exactly agrees with the antiferromagnetic to paramagnetic boundary determined from the heat capacity measurement under steady field²⁴⁾. Therefore, the boundary might be related with the long range order of the system.

More diluted specimens show the same features in the phase diagram with $x=0.31$ except the spin-flop, which is not observed for $x>0.5$. The hysteresis boundary of the specimen $x>x_p$ is found to disappear rapidly with increasing temperature. For example, the peak appearing in dM/dH_0 at the hysteresis boundary H_h of $x=0.9$ becomes about half in magnitude at 4.2 K compared with that at 1.3 K, and is unobservable at 10 K. So far, no evaluation has been made of the order of the observed transitions, or of the existence of multicritical points, except FeF_2 .

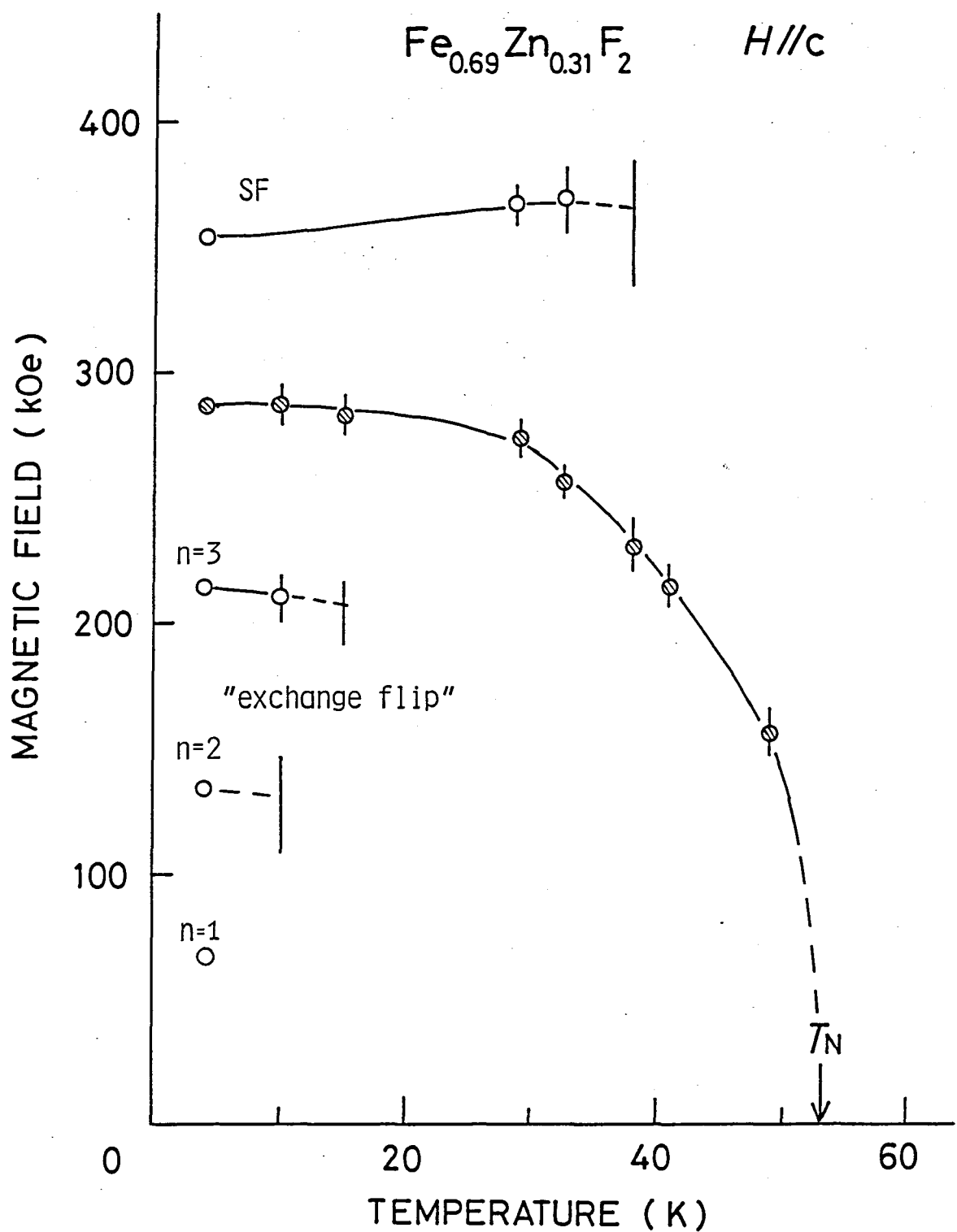


Fig.11 Temperature dependence of the transition fields in $\text{Fe}_{0.69}\text{Zn}_{0.31}\text{F}_2$. Shaded circles mark the hysteresis boundary.

§4. DISCUSSION

4.1 FeF₂

We have determined the AF-SF, AF-P boundaries and bicritical point of FeF₂. The observed spin-flop field H_{SF} at 4.2 K is in good agreement with the predicted value of thermodynamical boundary at T=0 (eq.(2)), calculated from the parameters determined previously³⁾. On the other hand, there was a discrepancy in the AF-P phase boundary between our result and the previous static one²³⁾. The boundary determined here is higher in the temperature than the static one at H₀>0. This may come from the adiabatic condition in our pulse field measurement. The specimen used is a bulk rod and the thermal relaxation time should be long, possibly of the order of second, while the field rise time is about 0.2 msec. Therefore, the specimen can not be in thermal equilibrium with the heat bath(helium gas). In this case, the temperature of the specimen changes with the field as

$$dT = - \frac{T}{C_H} (\partial M / \partial T)_H dH, \quad (3)$$

where C_H is the specific heat under field(see §4 of PART I). Now, dT should be negative when the field H₀ is applied parallel to the spin-easy axis of the antiferromagnet, because χ_{\parallel} of the antiferromagnet is an increasing function of temperature for T<T_N. In other words, fluctuation(entropy) of the spin system is increased by the field, and this effect absorbs heat from the

lattice under the adiabatic condition. Thus, the temperature of the specimen decreases with H_0 and the phase boundary is seen at higher starting temperature. The temperature decrease ΔT can roughly be estimated. Assuming χ_{\parallel} to be field-independent, $(\partial M / \partial T)_H$ can be replaced by $H_0 (\partial \chi_{\parallel} / \partial T)$. T/C_H is of course a function of field, but the field dependence can be neglected in the estimation of small temperature change near T_N . Then, eq.(3) can be integrated as

$$\Delta T = - \frac{T}{2C_H} (\partial \chi_{\parallel} / \partial T) H_0^2. \quad (4)$$

$(\partial \chi_{\parallel} / \partial T)$ is about 5×10^{-4} emu/mole·K, and C_H is about 40 J/mole·K at around T_N , so that ΔT is estimated as -2K at 200 kOe. The value will explain the difference between the static and pulsed field results. More accurate correction will need the field dependence of χ_{\parallel} and C_H , so that it is not done. The isothermal bicritical point will be lower in temperature by about 5 K.¹¹⁾

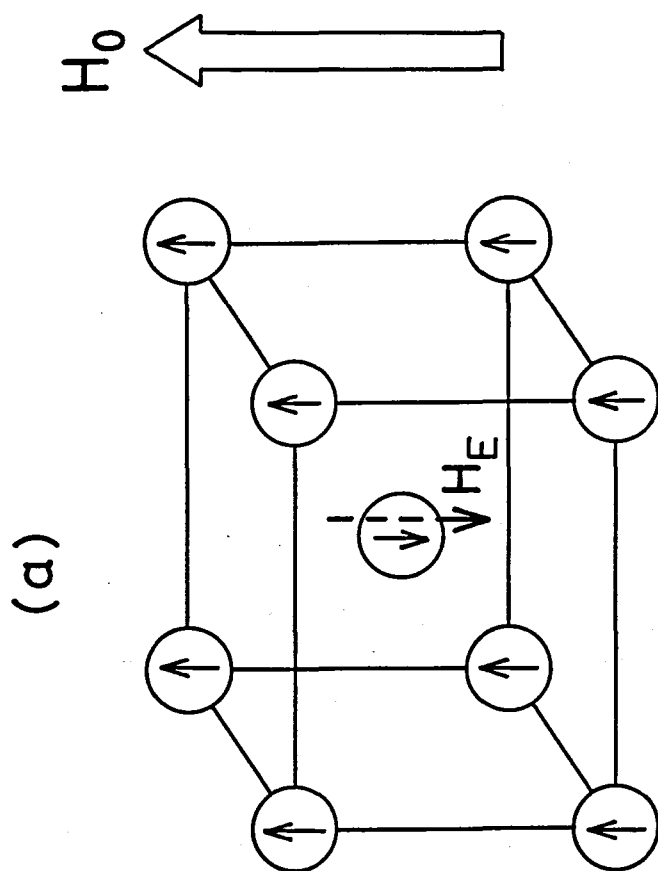
The AF-SF phase boundary was theoretically obtained by Rezende⁹⁾, who calculated the $\omega=0$ -field of down-going $k=0$ magnon mode by taking into account the four-magnon interaction arising from the single ion anisotropy. He showed that H_{SF} is a decreasing function of temperature. Our experimental results are, however, in complete disagreement with the theory. The reason of the discrepancy is not clear, but it may possibly be due to the use of the random-phase approximation in the treatment of the large single ion anisotropy.¹¹⁾

4.2 Diluted System

One of the remarkable results in the diluted specimens is the concentration independent "exchange flips" which are observed at fields $H_0 \approx 70n$ kOe, $n=1, 2, \dots$. This point is considered first. For a while, we assume Ising spins. One down-spin in the pure FeF_2 has the exchange field $H_E = 550$ kOe from the surrounding eight next nearest neighbour up-spins through J_2 , as is shown in Fig.12a. On the other hand, in a diluted system, the number n of exchange coupled up-spins around the down-spin distributes from 0 to 8. Fig.12 b is the case $n=3$, where the down-spin at the body center will have the effective exchange field $H_E' = (3/8)H_E$ from the neighbouring three up-spins. When the external field H_0 is applied parallel to c-axis, the total field acting on the down-spin reverses at $H_0 = H_E'$ and the down-spin will flip up. This effect will cause the magnetization discontinuities at $H_0 = (n/8)H_E = 69n$ kOe, $n=1, 2, \dots$, in accord with the experimental results. The magnetization and energy of this process can be obtained by simple probability calculation. The probability of any site having n neighbours is given by

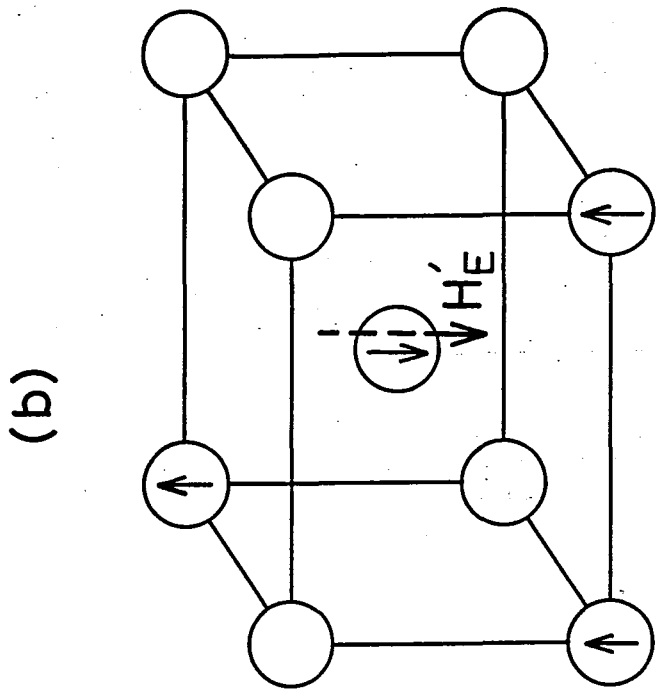
$$p(n) = z^C_n (1-x)^n x^{z-n}, \quad (3)$$

where z^C_n is the binomial coefficient and z is the coordination number. The concentration of occupied sites with n neighbours is given in the next page as



$$H_E = 550 \text{ kOe}$$

$$n = 8$$



$$n = 3$$

$$H'_E = \frac{3}{8} H_E$$

Fig.12 Exchange field acting on the down spin sites with $n=8$ (a) and $n=3$ (b) up spin neighbours. Small arrows indicate the direction of spins and broken arrows indicate the direction of the exchange fields. In the diluted specimen, the exchange field H'_E distributes as $H'_E = (n/8)H_E$, $n=1, \dots, 8$, where H_E denotes the exchange field of pure FeF_2 . External field H_0 is applied along the up spin direction.

$$\begin{aligned}
 C(n) &= (1-x)p(n) \\
 &= z C_n (1-x)^{n+1} x^{z-n}.
 \end{aligned} \tag{6}$$

When $H_0 = nH_E/z$, all down sublattice spins with n or fewer neighbours will flip up, giving the energy as

$$E = 2g\mu_B S H_E N \left[\sum_{m=1}^n (m/z) C(m) - (n/z) \sum_{m=1}^n C(m) \right], \tag{7}$$

relative to the AF state. Similarly, the change in the magnetization at this field is

$$\Delta M = 2g\mu_B S N C(n), \tag{8}$$

where N is the number of lattice points. The results for M are shown in Fig.13 for two concentrations $x=0.3$ and 0.5 by solid lines. It is noted that the simple model considered here does not include turning over of large clusters. In other words, all up sublattice spins are assumed to remain up throughout the magnetization process. This situation can be called as "ordered state flip", which will explain the initial stage of the experimentally observed magnetization. The magnetization process considered above will be actually reversible for small n , so long as the neighbours(up-spin) of the flipped spin have larger number of neighbours(down-spin) than the flipped one and can remain up at the decreasing field scan.

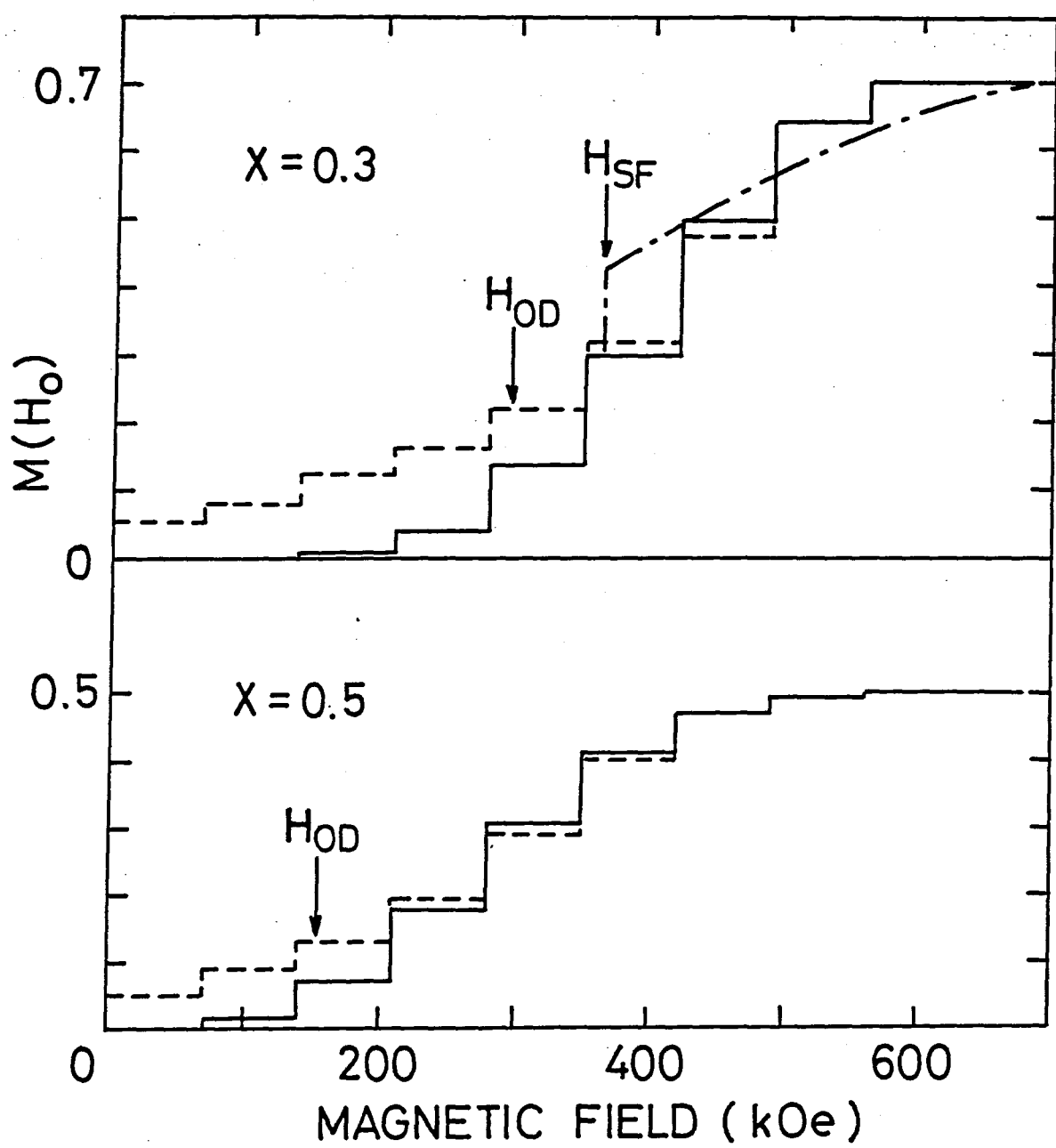


Fig.13 Simulated magnetization curves of $\text{Fe}_{1-x}\text{Zn}_x\text{F}_2$, $x=0.3$ and 0.5 for ordered flip(solid line), disordered flip(dotted line) and spin-flop phase(dot dashed line). Transition fields are also shown by arrows.

If $H_0 > H_E$, the spins become fully aligned in this model, and the original identities of the sublattices are lost. When H_0 is then decreased below $H_E'(n)$, a new decreasing field state will be entered, where spins with n neighbours on both sublattice may flip down, provided all n neighbours remain up. The state will possess no long range order. This can be easily understood by two dimensional($z=4$) model shown in Fig.14. Here, the initial AF state is shown in (a) where dotted lines indicate the down spin sublattice. When H_0 is decreased below H_E , two spins with $n=4$ will flip down first(Fig.14b). Decreasing H_0 further, $n=3$ flip-down occurs and the spins will have configuration given by Fig.14c. It is composed of short range AF domains nucleated from the $n=4$ flip-down shown in Fig.14b. We will refer to it as the "disordered flip state". Of course, such state becomes unstable below certain field, but it can not be treated by simple probability calculations as is used in the ordered state flips.

The magnetization M and energy E of the disordered flip state were obtained by computer simulation¹⁰⁾ and the results for M are shown by dotted lines in Fig.13. Comparing E with that of ordered state flip(7), it was shown that the disordered state is stable at high field but becomes higher in the energy than the ordered state below the field H_{OD} indicated in Fig.13. When H_0 is decreased below H_{OD} , the real system will try to relax to the ordered state by reversing domains or by the boundary motion, but the simulation allowed only single spin

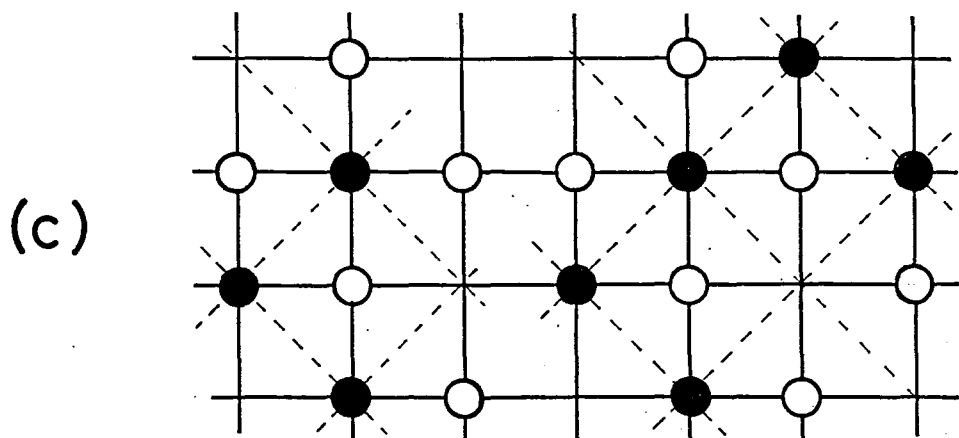
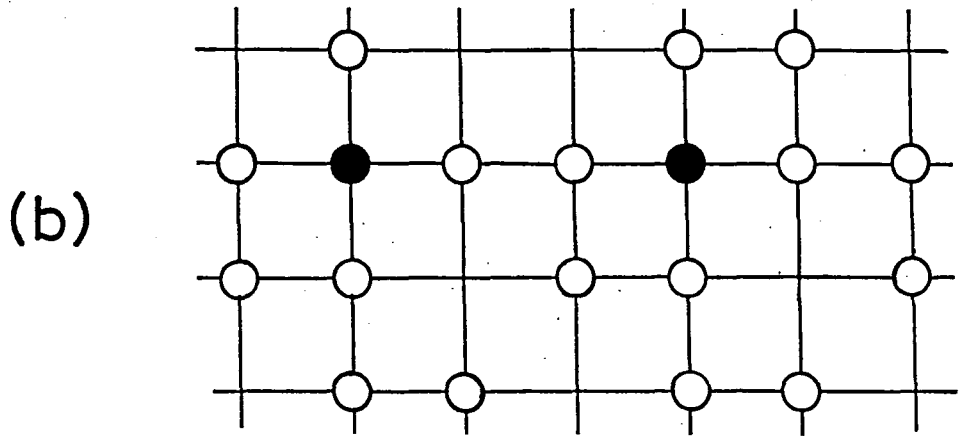
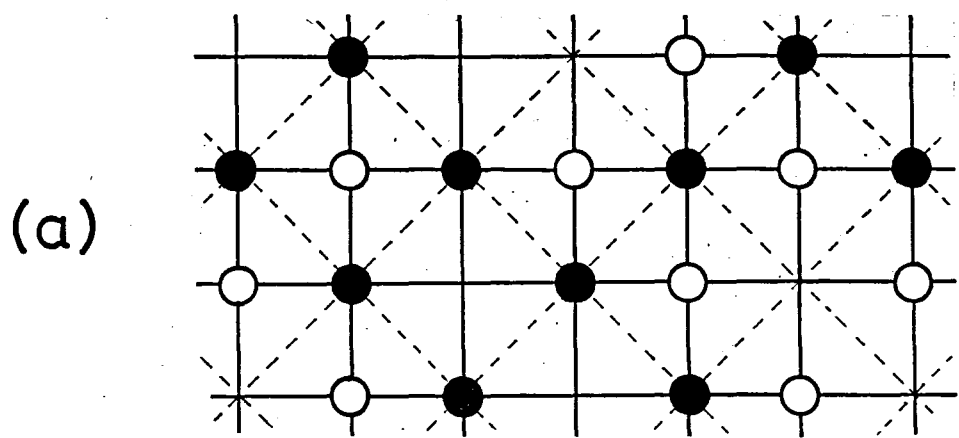


Fig.14 Two dimensional model ($z=4$) for the disordered flip in the decreasing field. Open circles denote up-spins and solid points are down-spins. The initial ordered state is shown in (a), where dotted lines indicate the down spin sublattice. The disordered state (c) arises from $n=4$ flip-down at $H_0=H_E$, shown in (b).

flips so that the model system remains trapped in the disordered state, showing finite magnetization even at $H_0=0$. It is noticed that the disordered state has larger M than the ordered state at H_{OD} . Considering these points, an idea arises that the hysteresis boundary H_h , accompanied by an anomalous peak in dM/dH_0 only seen in the field increasing scan, may be explained by a crossover from the low field ordered state to the high field disordered one at H_{OD} . In fact, H_{OD} is found to be very close to H_h . Moreover, as the magnetization of the disordered state is larger than the ordered one, the transition will result in a peak in dM/dH_0 . The disordered state is likely to be a large set of nearly degenerated states so that such a transition will occur in a large number of ways and consequently very rapidly. However, the reverse transition can occur in only a single way and would be much slower process. Thus, the order-disorder (O-D) transition might have an inherent hysteresis in the rate and would not occur in the field-decreasing scan in the pulsed field measurement. The observed temperature dependence of H_h also supports the order-disorder transition model.

The hysteresis boundary H_h shows linear decrease toward zero at around the percolation limit x_p . This may be explained in the present model by the fact that the domain wall energy decreases with x and the domain can easily be formed at lower field with increasing x . However, the reason that the H_h persists beyond x_p is not fully understood. One of the possible accounts may be the followings: the disordered state in the

present model consists of considerable short-range antiferromagnetic domains whose size L is mainly determined by the configuration of magnetic ions and likely to become smaller with increasing x . On the other hand, the short range ordered state at $H_0=0$ for $x>x_p$ is composed of antiferromagnetic clusters or chains whose average size L_0 is determined by x . As we expect $L_0>L$ at low temperature, a destruction of the short range order into much smaller domain will occur at certain field. In this case, the "O-D transition" is not the genuine one but means the abrupt change in the spin correlation length ξ . As ξ is a decreasing function of temperature, such transition will not occur above certain temperature T_0 where $\xi < L$. This is also consistent with the experimental results.

So far, we assumed Ising spins. The real system $Fe_{1-x}Zn_xF_2$, however, is not the case and spin-flop(SF) occurs for small x . Therefore, the above model is applicable only at H_0 below the spin-flop field H_{SF} . It is natural that H_{SF} first decreases linearly with small dilution. On the other hand, H_{SF} shows a leveling off at around $x=0.3$. This fact will be the consequence of the spin-flips and the O-D transition, both of which will considerably decreases the energy of spin-colinear state (moment parallel to c-axis), making the spin-canted state less favorable. The peak appearing in $x=0.31$ at around 350 kOe (Fig.6a) is believed to be the spin-flop for the following reasons: it appears both in increasing and decreasing field, and no higher flip is observed up to 550 kOe.

The magnetization curve of $x=0.31$ (Fig.7) also supports the idea. The extrapolation of the magnetization above H_{SF} intersects the origin (dashed line), showing that the spins are in a canted state above H_{SF} . On the other hand, specimens for $x>0.5$ have only exchange flips in the high field region, showing the spins are in colinear state. Therefore, the spin-flop seems to end between $x=0.31$ and 0.5. The spin-flop in a random spin system can not be treated quantitatively in a simple way so we must rely again on the simulation¹⁰⁾. The energy of SF state is compared with that of ordered and disordered states, and the predicted $H_{SF}(x)$ is shown in Fig.8 by solid line, in good agreement with the experimental results. The SF-state is found to become higher in the energy than the flip state and end at around $x=0.4$, in accord with our experiments. The simulated magnetization process of SF-state is shown in Fig.13 for $x=0.3$ by dot-dashed line. It is very interesting that the SF and O-D transitions seem to coexisting at around $x=0.3$. In SF-state, the antiferromagnetic component of spins is perpendicular to the external field so that there is no Zeeman energy reduction by making domain structure. Therefore, the long range order might be reentered above H_{SF} .

Figure 15 shows the simulation of dM/dH_0 ¹⁰⁾, obtained by superimposing Gaussian peaks of amplitudes corresponding to the calculated ΔM at the transitions seen in Fig.13. The Gaussian width are chosen to best fit the data and are about 30 kOe. The width is expected for a strain-induced exchange broadening.

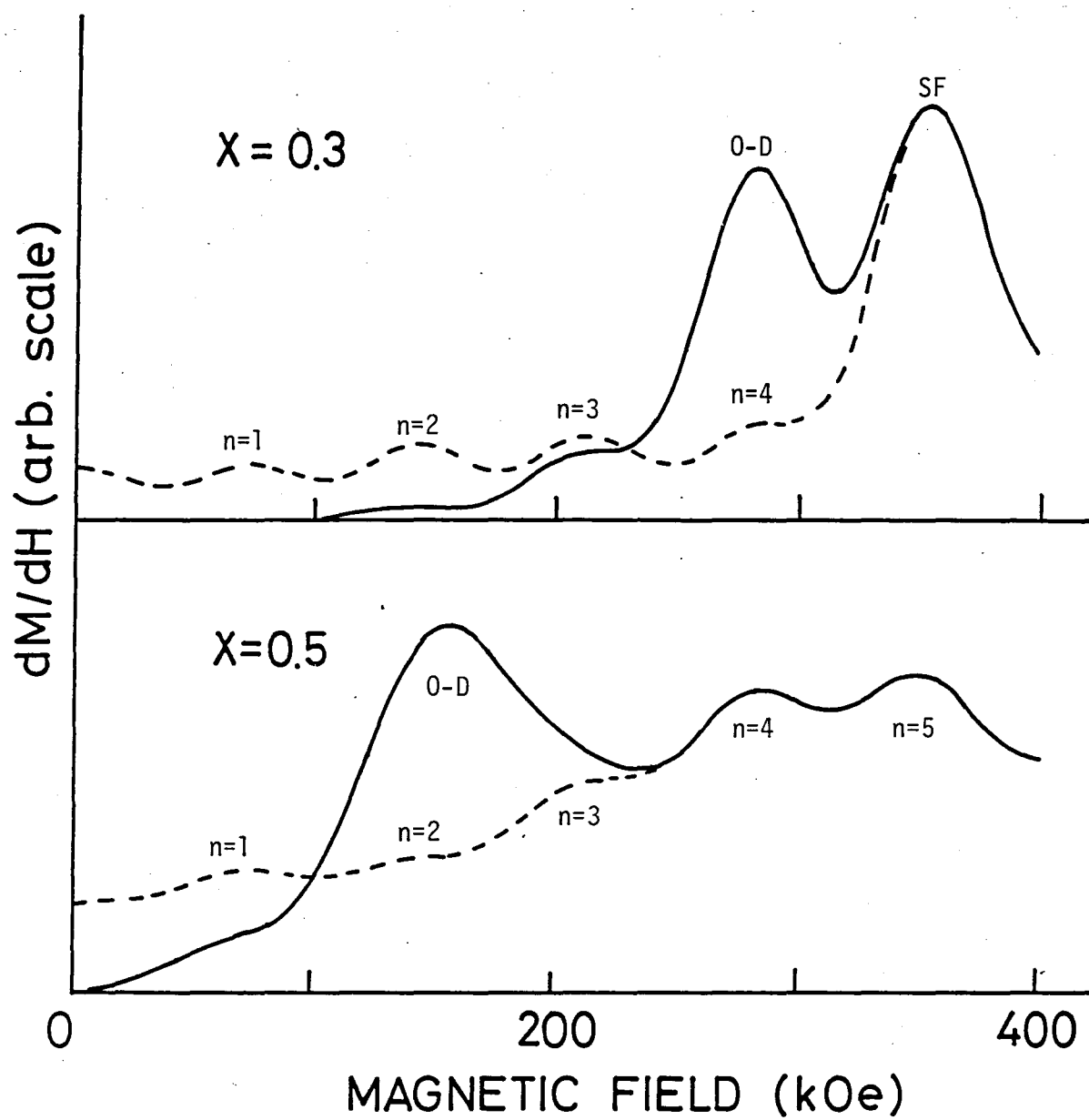


Fig.15 Simulated dM/dH curves of $Fe_{1-x}Zn_xF_2$, $x=0.3$ and 0.5 .
 Solid lines are field-increasing sweep and dotted lines are decreasing one.

The solid lines in the figure indicate the field-increasing scan and the dotted lines are the field-decreasing one. For $x=0.3$, solid line represents the ordered flips $n=1$ to 3, the O-D transition and the transition from the ordered state to SF. The dashed line is the reverse transition SF to disorder, and disordered flips $n=5$ to 0. For $x=0.5$, the solid line represents the ordered flips $n=1$ and 2, the O-D transition and the disordered flips $n=3$ to 6. The dashed line represents the disordered flips $n=6$ to 0. These simulated dM/dH_0 curves agree remarkably well with the experimental results of the corresponding concentrations shown in Figs.2 and 3. Thus, one may conclude that the important features of the experiments are explained by the effects considered here.

We have discussed the observed hysteresis boundary in terms of the "order-disorder transition" from the empirical point of view. The model is supported by the fact that the boundary smoothly connects to the antiferromagnetic to paramagnetic phase boundary determined from the heat capacity measurement.^{8,24)} However, one can not derive a definite conclusion from the magnetization measurement whether there is a long range order in the system or not. Even if the spin correlation length ξ is a gradual decreasing function of field as is predicted from the random field theory¹⁵⁾, the system may be looked as if in the ordered state so long as ξ is longer than the average distance of n -th spin-flip site in our model²⁵⁾. When ξ becomes shorter

than the distance, the system will show an apparent transition to the disordered state as is observed in the specimen with $x > x_p$.

On the other hand, if the order-disorder boundary is a genuine one, the whole phase diagram will be a quite novel one. The low temperature part of the boundary is not a simple antiferromagnetic to paramagnetic one, because the moment is not saturated there. There might be certain critical point on the boundary that is not seen yet, which separates the low temperature O-D boundary from the high temperature AF-P one. Further inquiries to these problems from the different approach will be needed.

REFERENCES

- 1) R.A. Cowley: AIP Conf. Proc. 29 (1976) 243.
- 2) R.A. Cowley, G. Shirane, R.J. Birgeneau, E.C. Svensson and H.J. Guggenheim: Phys. Rev. B22 (1980) 4412.
- 3) M.T. Hutchings, B.D. Rainford and H.J. Guggenheim: J. Phys. C3 (1970) 307.
- 4) G.K. Wertheim, D.N.E. Buchanan and H.J. Guggenheim: Phys. Rev. 152 (1966) 527.
- 5) R.A. Tahir-Kheli and A.R. McGurn: Phys. Rev. B18 (1978) 503.
- 6) Cid B. de Araujo: Phys. Rev. B22 (1980) 266.
- 7) A.R. King and V. Jaccarino: J. Appl. Phys. 52 (1981) 1785.
- 8) D.P. Belanger, A.R. King and V. Jaccarino: Phys. Rev. Lett. 48 (1982) 1050.
- 9) S.M. Rezende: J. Phys. C11 (1978) L701.
- 10) A.R. King, V. Jaccarino, T. Sakakibara, M. Motokawa and M. Date: Phys. Rev. Lett. 47 (1981) 117; J. Appl. Phys. 53 (1982) 1874; Proc. Int. Symposium on High Field Magnetism, 1982, Osaka.
- 11) V. Jaccarino, A.R. King, M. Motokawa, T. Sakakibara and M. Date: Proc. Int. Conf. on Magnetism, 1982, Kyoto.
- 12) S. Fishman and A. Aharony: J. Phys. C12 (1979) L729; J. Magn. Magn. Mat. 15-18 (1980) 239.
- 13) A. Aharony: Phys. Rev. B18 (1978) 3318, 3328.
- 14) Y. Imry and S. Ma: Phys. Rev. Lett. 35 (1975) 1399.

- 15) E. Pytte, Y. Imry and D. Mukamel: Phys. Rev. Lett. 46 (1981) 1173.
- 16) H. Rohrer: J. Appl. Phys. 52 (1981) 1708.
- 17) Y. Shapira: J. Appl. Phys. 53 (1982) 1931.
- 18) H. Yoshizawa, R.A. Cowley, G. Shirane, R.J. Birgenau, H.J. Guggenheim and H. Ikeda: Phys. Rev. Lett. 48 (1982) 438.
- 19) H. Yasuoka, C.J. Magon and V. Jaccarino: J. Phys. Soc. Jpn. 51 (1982) 1039.
- 20) R.A. Cowley and W.J.L. Buyers: J. Phys. C15 (1982) L1209.
- 21) J. Stout, M.I. Steinfield and M. Yuzuri: J. Appl. Phys. 39 (1968) 1142.
- 22) M. Tinkham: Proc. Roy. Soc. A 236 (1956) 535.
- 23) Y. Shapira: Phys. Rev. B2 (1970) 2725.
- 24) A.R. King: private communication.
- 25) M. Motokawa: private communication.

ACKNOWLEDGEMENTS

The author wishes to express his sincere gratitude to Professor Muneyuki Date for his valuable suggestions and enlightening discussions, and for his continuous encouragement throughout the present work. Thanks are also due to Professor Mitsuhiro Motokawa for many stimulating discussions.

The author would like to thank Professor Hiroyoshi Suematsu of Institute of Materials Science, University of Tsukuba, for supplying C_6Eu crystals and for many helpful discussions about the problem. He would also like to thank Professor Vincent Jaccarino and Dr. Allan R. King of University of California, Santa Barbara, for supplying $Fe_{1-x}Zn_xF_2$ crystals and for their valuable suggestions about the problem.

He is indebted to Mr. Kiyohiro Sugiyama for the cooperation in the magnetization measurements. Finally, the author wishes to thank all the members of Date laboratory.